Deciphering the role of USH1G/SANS in protein-protein interactions and nuclear shuttling.

Dissertation:

Submitted to the Faculty of Biology (FB10)

In partial fulfilment of requirements for the

„Doctor rerum naturalium“

Johannes Gutenberg-Universität Mainz

Jacques Sebastian Fritze

(DOB: 12.09.1992, Malsch)

Mainz, 15.01.2025

Dean: Univ.-Prof. Dr. Eckhard Thines,
Institute of Biotechnology
and Drug Research

1. PhD reviewer: [redacted]
Institute of Molecular Physiology

2. PhD reviewer: [redacted],
Institute of Molecular Physiology

Date of thesis defense: _____

Much to learn, you still have.

-Yoda; Star Wars

1 Explanatory notes

The present doctoral work is a cumulative thesis consisting of two essential articles:

Publication 1

Fritze J.S., Stiehler F.F., Wolfrum U. (2023).
Pathogenic Variants in USH1G/SANS Alter Protein Interaction with Pre-RNA Processing Factors PRPF6 and PRPF31 of the Spliceosome.
Int J Mol Sci. 2023 Dec 18;24(24):17608.
doi: 10.3390/ijms242417608.; PMID: 38139438; PMCID: PMC10744108

Publication 2

Fritze J.S., Stiehler F.F., Wolfrum U. (2024). Nuclear–Cytoplasmic Shuttling of the Usher Syndrome 1G Protein SANS Differs from Its Paralog ANKS4B.
Cells. 2024 Nov 8;13(22):1855
doi: 10.3390/cells13221855.; PMID: 39594604; PMCID: PMC11592671

Additionally, I provide two preliminary data sets:

Chapter 7.3:

SANS alters the mobility of PRPF31 in Cajal bodies of the nucleus

Chapter 7.4:

Assessment of PRPF31 nuclear mobility

In addition to the publications compiled for this dissertation, I have contributed at the JGU Mainz to the following scientific work:

Nagel-Wolfrum K., Fadl B.R., Becker M.M., Wunderlich K.A., Schäfer J., Sturm D., **Fritze J.**, Gür B., Kaplan L., Andreani T., Goldmann T., Brooks M., Starostik M.R., Lokhande A., Apel M., Fath K.R., Stingl K., Kohl S., DeAngelis M.M., Schlötzer-Schrehardt U., Kim I.K., Owen L.A., Vetter J.M., Pfeiffer N., Andrade-Navarro M.A., Grosche A., Swaroop A., Wolfrum U.
Expression and subcellular localization of USH1C/harmonin in human retina provides insights into pathomechanisms and therapy
Hum Mol Genet. 2023 Jan 13;32(3):431-449.
doi: 10.1093/hmg/ddac211.; PMID: 35997788; PMCID: PMC9851744

2 Index

3 List of Abbreviations

ANK ..... *ankyrin repeats*
ANKS4B ..... *ankyrin repeat and SAM domain-containing protein 4B*
CC ..... *coiled coiled*
CENT ..... *central domain*
cryo-EM ..... *cryo-electron microscopy*
FRAP ..... fluorescence recovery after photobleaching
FRET ..... *fluorescence resonance energy transfer*
HAT ..... *half TPR*
IDR ..... *intrinsically disordered region*
NES ..... *nuclear export sequence*
NLS ..... *nuclear localization sequence*
NMR ..... *nuclear magnetic resonance*
NPC ..... *nuclear pore complexes*
PBM ..... *PDZ binding motif*
PRPF ..... *pre-mRNA processing factors*
RP ..... *Retinitis Pigmentosa*
SAM ..... *sterile alpha motif*
SANS ..... *scaffold protein containing ankyrin repeats and SAM domain*
snRNPs ..... *small nuclear ribonucleoproteins*
USH ..... *Human Usher syndrome*

4 Introduction

Human Usher syndrome (USH) is a complex, rare, heterogeneous disease resulting in hearing and vision loss as well as vestibular dysfunction (Fuster-Garcia et al., 2021). To date, mutations in 15 distinct genes have been identified as the cause of this disease, but the underlying molecular pathophysiology remains largely elusive. With this thesis I aim to decipher the underlying cellular mechanisms of the Human Usher syndrome-associated protein SANS. SANS was recently functionally connected with pre-mRNA splicing in the nucleus (Yildirim et al., 2021). I aimed to provide a more detailed understanding of SANS' nuclear role, focusing on its interaction with other splicing-related proteins and the mechanisms behind its nuclear-cytoplasmic shuttling that enable it to fulfill its functional role.

4.1 The human Usher syndrome

Human Usher syndrome is a monogenetic autosomal recessive genetic disorder with a prevalence of 3:100,000 representing the most common form of deaf–blindness (Fuster-Garcia et al., 2021). USH is originally distinguished in three clinical subtypes (USH1-3) (Millan et al., 2011). However, recent findings suggest a fourth subtype (USH4) (Fuster-Garcia et al., 2021; Peter et al., 2021; Velde et al., 2022; Ullah et al., 2024). USH1 is the most severe subtype manifesting in hearing loss, vestibular dysfunction, and pre-pubertal onset of retinal dysfunctions in the form of *retinitis pigmentosa* (RP) (Mathur & Yang, 2015).

Twelve genes and three gene loci have been identified so far with mutations in these genes leading to USH (Figure 1) (Fuster-Garcia et al., 2021). The mutation in one of those USH proteins encoding genes is enough to cause USH. Ten of the respective encoded USH proteins interact with each other and form through this a protein network the USH-interactome (Figure 1) (Wolfrum, 2011; Fuster-Garcia et al., 2021). The USH interactome has been shown to play a crucial role at the stereocilia tip link in the inner ear and the connecting cilia of the photoreceptor cells in the retina (Fuster-Garcia et al., 2021). Moreover, USH-proteins belong to different protein classes such as motor proteins, adhesion proteins and scaffold proteins (Mathur & Yang, 2015). One of these scaffold proteins is the scaffold protein containing ankyrin repeats and SAM domain (SANS) (Weil et al., 2003; Fuster-Garcia et al., 2021), which is encoded by *USH1G* and is the main focus of this thesis.

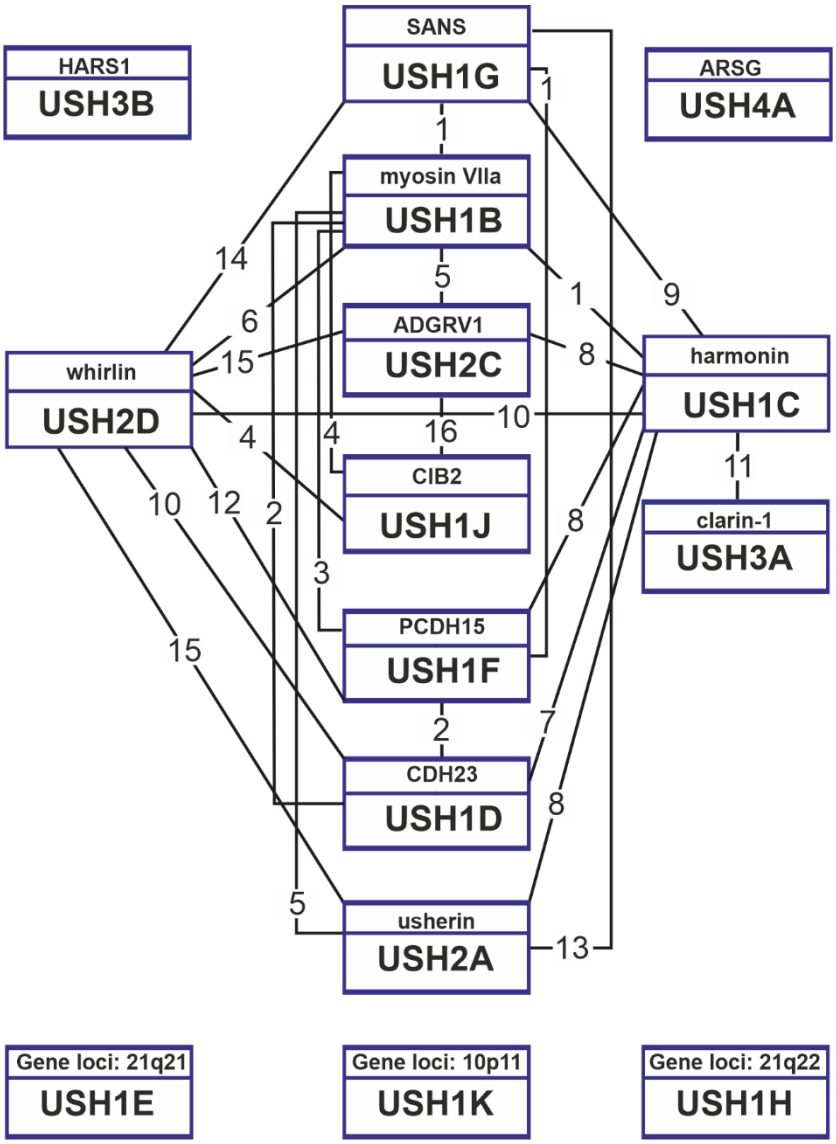

Figure 1. Overview of the 15 USH causing genes. USH causing genes are written in blue boxes, protein names are written above. For USH1E, USH1K and USH1H the gene locus is indicated as no encoded protein is known. Known protein-protein interactions are shown with grey lines. Publications that show protein-protein interactions are indicated with numbers. 1: (Adato et al., 2005b); 2: (Kazmierczak et al., 2007); 3: (Senften et al., 2006); 4: (Riazuddin et al., 2012); 5: (Michalski et al., 2007); 6: (Delprat et al., 2005); 7: (Grillet et al., 2009); 8: (Reiners et al., 2005); 9: (Yang et al., 2010); 10: (Zhu et al., 2020); 11: (Dulon et al., 2018); 12: (Michel et al., 2020); 13: (Sorusch et al., 2017); 14: (Maerker et al., 2008); 15: (van Wijk et al., 2006); 16: (Linnert et al., 2023). Adapted from (Wolfrum, 2011; Fuster-Garcia et al., 2021).

4.2 Scaffold protein containing ankyrin repeats and SAM domain (SANS)

The human *USH1G* gene (chromosome loci 17.11) encodes SANS, a scaffold protein of ~52 kDa molecular weight consisting of 461 amino acids (Weil et al., 2003). More than 70 pathogenic variants in *USH1G*/SANS have been identified thus far in USH1 patients, which lead to USH1 symptoms (Fokkema et al., 2011).

SANS is composed of three ankyrin repeats (ANK1-3), a central domain (CENT), a sterile alpha motif (SAM), as well as a PDZ binding motif (PBM) at the C-terminal end (Figure 2) (Sorusch et al., 2017). The CENT domain is functionally further divided into a N-terminal CENTn and a C-terminal CENTc domain (Sorusch et al., 2017). Based on experimental and prediction data the CENT domain can be further divided into three subdomains, CENTn1, CENTn2, and CENTc (Fritze et al., 2023). As a scaffold protein, SANS binds multiple proteins through its various domains (Adato et al., 2005b; Maerker et al., 2008; Sorusch et al., 2019; Yildirim et al., 2021) (Representative binding partners shown in Figure 2). However, SANS' CENT domain appears to be the primary binding platform with 50 putative binding partners identified so far (Maerker et al., 2008; Overlack et al., 2011; Sorusch et al., 2017; Yildirim et al., 2021).

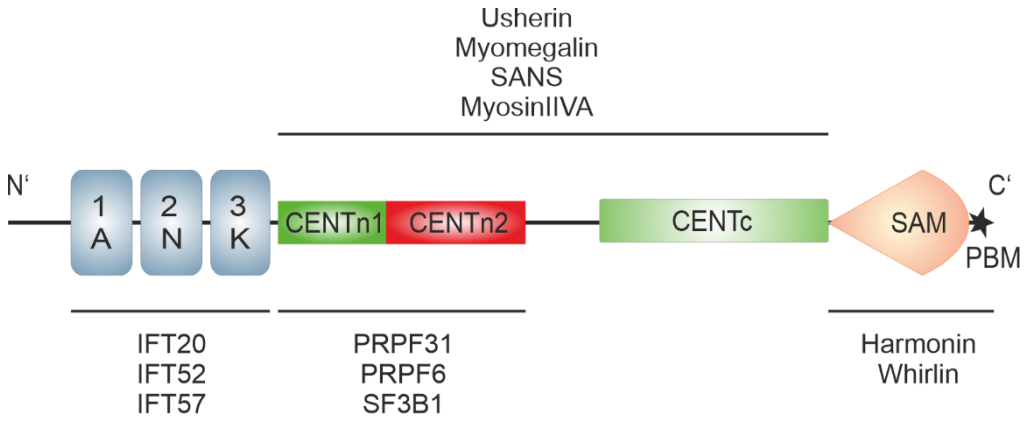

Figure 2. Cartoon of scaffold protein containing ankyrin repeats and SAM domain (SANS). SANS consists of three ankyrin repeats, three central domains CENTn1, CENTn2 and CENTc, as well as a SAM domain with a C-terminal PDZ binding motif (PBM). Representative binding partners of SANS from up to 50 putative binding partners of SANS are indicated. (Adato et al., 2005b; Maerker et al., 2008; Yan et al., 2010; Overlack et al., 2011; Sorusch et al., 2017, 2019; Yildirim et al., 2021)

In auditory hair cells, SANS is essential for the proper arrangement of the stereocilia in the hair bundles during development and for the composition and function of the mechanosensitive tip-link complex at the tip of the stereocilia (Caberlotto et al., 2011; He et al., 2019; Géléoc & El-Amraoui, 2020). In the retina, SANS is expressed in photoreceptor cells, where it is associated with intracellular transport, endocytosis, nuclear splicing and primary ciliogenesis (Maerker et al., 2008; Overlack et al., 2011; Papal et al., 2013; Bauss et al., 2014; Sorusch et al., 2019; Yildirim et al., 2021). In addition, recent single cell RNAseq data suggest that SANS is expressed in Müller glia cells (Lukowski et al., 2019; Cowan et al., 2020). These cells regulate extracellular

space volume, ion and water homeostasis, and take part in repair mechanisms of the human retina (Reichenbach & Bringmann, 2020).

SANS has been observed in both the cytoplasm and nucleus of cells (Sorusch et al., 2017). In the nucleus, SANS was linked to the regulation of pre-mRNA splicing and activation of the spliceosome through interactions with several spliceosomal components (Yildirim et al., 2021). Furthermore, siRNA-based knockdown of SANS showed alterations in alternative splicing of specific target genes, which could be rescued by wild type SANS but not by pathogenic variants of SANS. The interactions between SANS and these splicing proteins remain incompletely understood, thus we aimed to elucidate these interactions in detail.

Interestingly, SANS has a paralogue protein, namely ankyrin repeat and SAM domain-containing protein 4B (ANKS4B) (Crawley et al., 2016). ANKS4B is a small ~46 kDa protein, consists of 417 amino acids and shares up to 80% amino acid similarities to SANS in its N- and C-terminal region (Crawley et al., 2016; Graves et al., 2020) (Figure 3). Like SANS, ANKS4B consists of three ANK, a SAM domain and a PDZ binding motif, but its CENT domain is less understood (Figure 3) (Crawley et al., 2016).

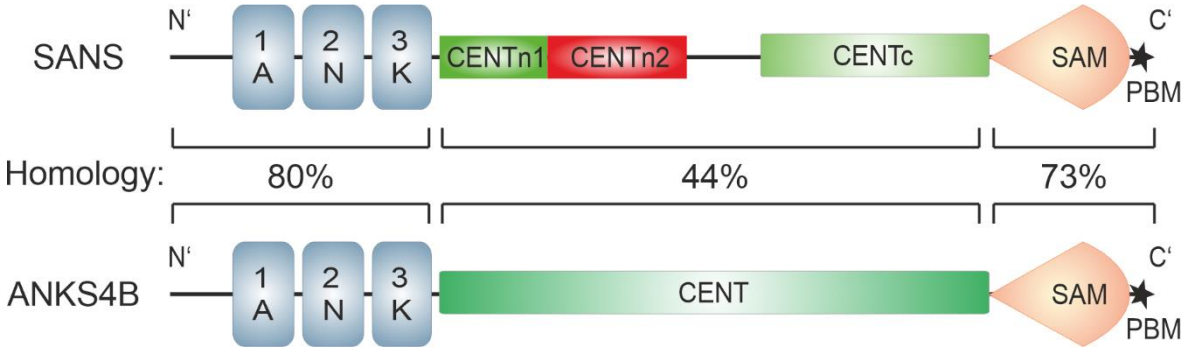

Figure 3. Cartoon of SANS and ANKS4B. Like SANS ANKS4B consists of three Ankyrin repeats (ANK), a central domain (CENT), a SAM domain and a C-terminal PBM. SANS and ANKS4B share up to 80% homology in their amino acid sequence.

SANS and ANKS4B share common binding partners such as harmonin but differ in their interaction to others such as Myosin-IIVA and Myosin-IIVB (Adato et al., 2005b; Crawley et al., 2016; He et al., 2019). The expression patterns of SANS and ANKS4B differ across various human organs. While SANS is predominantly localized in sensory cells, ANKS4B shows high expression levels in kidney and the gastrointestinal tract (Weil et al., 2003; Johnston et al., 2004; Uhlén et al., 2015). Here, ANKS4B functions as a scaffold protein in the inter-microvillar adhesion complex of the brush border of

intestinal enterocytes (Crawley et al., 2016; He et al., 2019). In contrast to SANS, ANKS4B has not been reported in the nucleus and is not associated with nuclear functions. Moreover, no disease relation of ANKS4B has been defined, but recent data indicate a role in diabetes and colon cancer (Sato et al., 2012; Xu et al., 2021).

4.3 Pre-mRNA splicing and the tri-snRNP-complex

As mentioned above, SANS functions in alternative splicing (Yildirim et al., 2021). Pre-mRNA splicing is a fundamental process in eukaryotic cells that occurs in the nucleus (Matera & Wang, 2014). It allows the inclusion or exclusion of exons and introns in mRNA, leading to the synthesis of multiple alternative protein isoforms from a single genomic locus (Figure 4A) (Matera & Wang, 2014; Papasaikas et al., 2015).

Splicing is catalyzed by the spliceosome, a highly dynamic macromolecular complex composed of five small nuclear ribonucleoprotein complexes (U1, U2, U5, U4/U6 snRNPs) and numerous other (>150) polypeptides (Papasaikas et al., 2015). The maturation of most snRNPs involves multiple steps occurring in both, the nucleus and cytoplasm (Matera & Wang, 2014). The maturation of the tri-snRNP complex (U4/U6.U5 snRNPs) is particularly elaborate, as two of the involved snRNPs, U4 and U5, are transported from the nucleus to the cytoplasm after their biogenesis, where they undergo further maturation (Mroczek & Dziembowski, 2013; Matera & Wang, 2014).

After transport back into the nucleus, the U4, U5 and U6 snRNPs are assembled into the final tri-snRNP complex within the so-called Cajal bodies (Figure 4B) (Matera & Wang, 2014; Staněk, 2017). From here, the matured tri-snRNP complex is transferred to nuclear speckles, which store spliceosomal components and are involved in splicing (Hasenson & Shav-Tal, 2020; Liao & Regev, 2021).

As a major building block of the spliceosome the tri-snRNP complex is of great importance and its final maturation in the Cajal bodies is highly dependent on two pre-mRNA processing factors (PRPF) PRPF31 and PRPF6 (Makarova et al., 2002; Schaffert et al., 2004). The small U4/U6 snRNP protein PRPF31 (499 residues) interacts via its coiled-coiled domain with the C-terminal HAT domains of the U5 snRNP protein PRPF6 (941 residues), leading to the formation of the tri-snRNP complex (Figure 4C) (Makarova et al., 2002; Liu et al., 2006, 2007; Staněk, 2017). Interestingly, pathogenic variants of both, PRPF31 and PRPF6, lead to non-syndromic RP in patients (Liu et al., 2007; Tanackovic et al., 2011). Previously, our group identified

SANS as a binding partner of both PRPF31 and PRPF6 (Yildirim et al., 2021). This leads to the question, how SANS interacts with both proteins and how it enters the nucleus to fulfill its role in splicing.

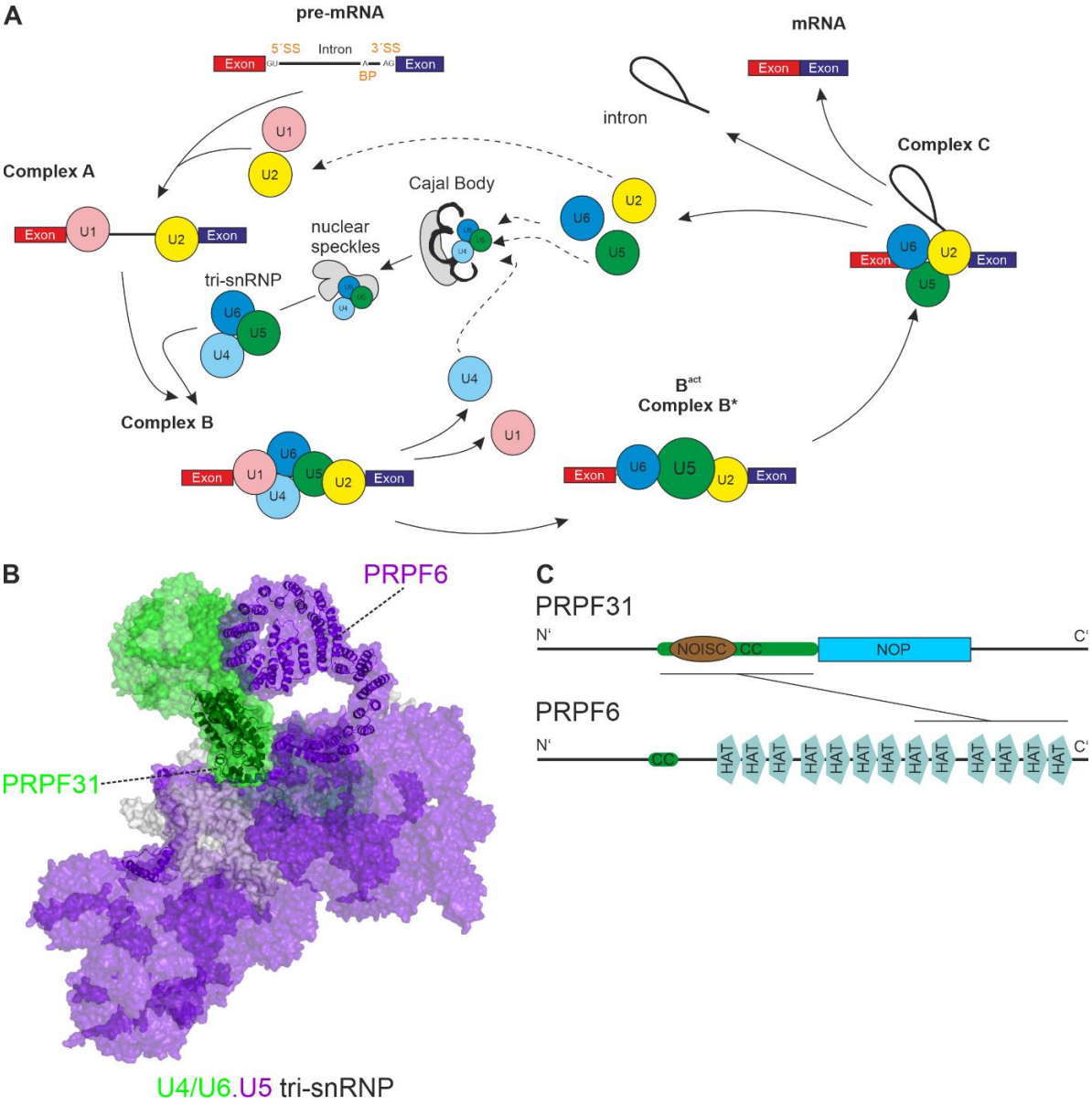

Figure 4. Schematic of the splicing process and tri-snRNP complex. (A) Five snRNAs (U1, U2, U4/U6 and U5) and more than 150 snRNPs are involved in the spliceosome. Complex A is formed by the recognition of U1 and U2 snRNPs 5`splice site (SS) and 3` branch point motif, respectively. It is followed by the recruitment of tri-snRNP complex, which is maturated in Cajal bodies and stored in nuclear speckles, to complex A for the formation of pre-catalytic complex B. Activation of complex B (Bact, catalytically inactive) is regulated by compositional and conformational rearrangement of itself. Catalytically active complex B (B*) leads to intron 3´- exon splicing. Following, complex C executes the ligation of remaining exons. Modified from (Yildirim, 2019). **(B)** Protein structure of the U4/U6.U5 tri-snRNP complex shown by cryo-EM modified from (Charenton et al., 2019). **(C)** Cartoon of PRPF31 and PRPF6. PRPF31 consists of a NOISC domain, a coiled coiled (CC) domain and a NOP domain. PRPF6 consists of a CC and thirteen half TPR (HAT) domains (Liu et al., 2006, 2007).

4.4 Nuclear transport

Since SANS functions in the nucleus an the cytoplasm (Sorusch et al., 2017; Yildirim et al., 2021), it has to be transported in- and outside of the nucleus. Efficient nuclear-cytoplasmic shuttling of macromolecules to their correct subcellular compartment is critical for proper functioning of the eukaryotic cell (Wing et al., 2022).

In humans, approximately 60 proteins participate in nuclear transport (Yang et al., 2023). The Ran-GDP/GTP system functions as a major key-player in this process and ensures directed and rapid transport (Figure 5). This transport is channeled over the nuclear membrane through nuclear pore complexes (NPC) (Wing et al., 2022; Yang et al., 2023) (Figure 5). In most cases proteins called karyopherins bind macromolecule cargoes and transport them in-/outside of the nucleus (Wing et al., 2022). Among them are members of the karyopherin-β family, commonly known as importins and exportins, which mediate the main trafficking across NPCs (Wing et al., 2022) (Figure 5).

Karyopherins recognize specific nuclear localization sequences (NLSs) and nuclear export sequences (NESs) on cargo molecules to facilitate trafficking (Figure 5). NLSs can be divided into two groups: non-classical NLSs, which have diverse protein sequences and structures, and classical NLSs, which are 4-16 residue long protein sequences containing positively charged residues (Lu et al., 2021; Wing et al., 2022). Only classical NESs were identified, which are recognized by CRM1/Exportin-1 (Fung et al., 2021; Wing et al., 2022). NESs are protein sequences that consists of hydrophobic residues (Φ) linked with other residues (X) and follow a certain scheme ($\Phi 1X_{2-3}\Phi 2X_{2-3}\Phi 3X\Phi 4$ or $\Phi 1X\Phi 2X_{2-3}\Phi 3X_{2-3}\Phi 4$) (Fung et al., 2021).

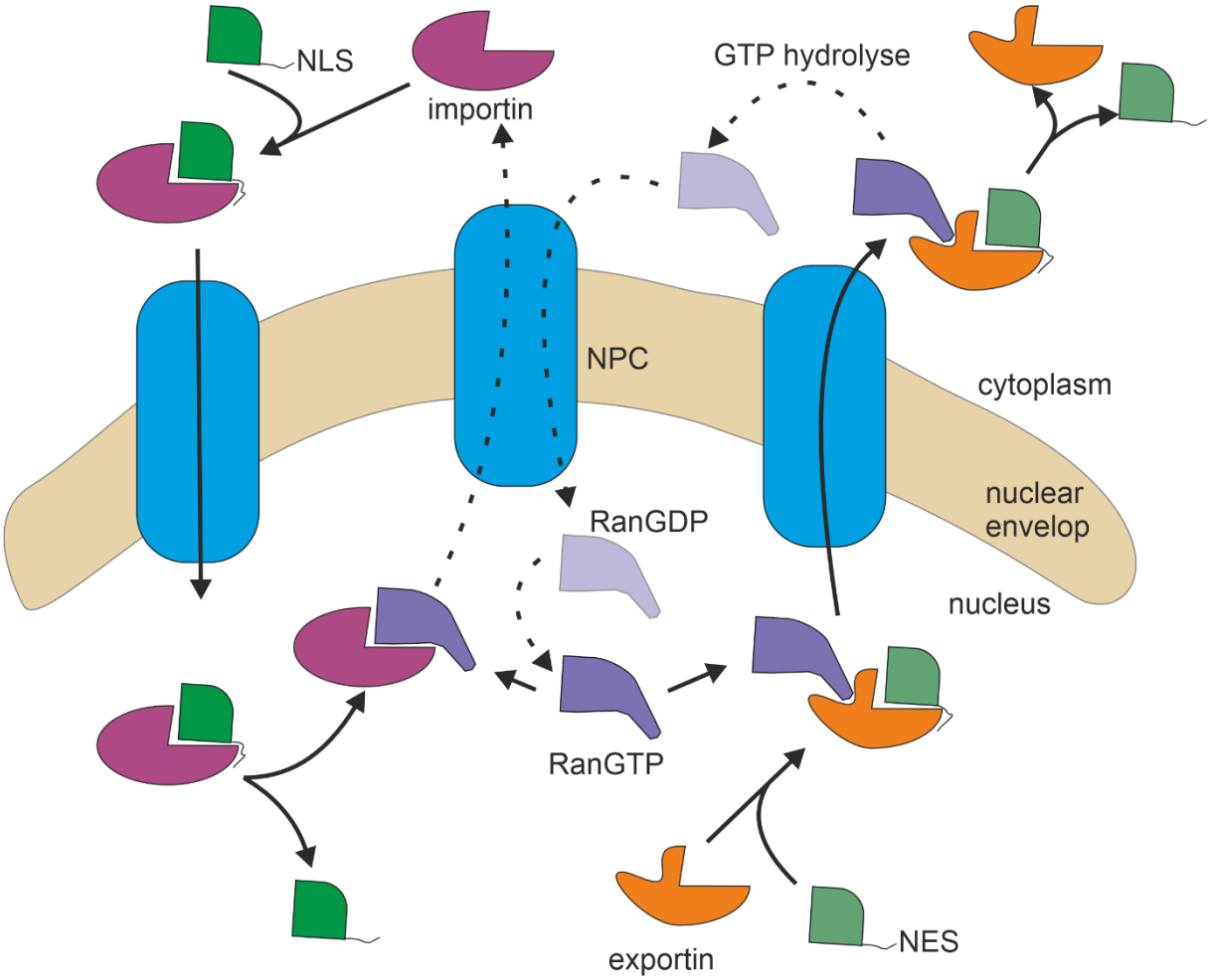

Figure 5. Model of protein nuclear import and export. Imported cargoes containing nuclear localization signals (NLS) form complexes with importins in the cytoplasm, enter the nucleus through the nuclear pore complexes (NPC), and are dissociated from the importins with the aid of RanGTP. Nuclear export of cargoes starts with the formation of trimeric complexes consisting of exportin, nuclear export signal (NES)-containing cargo, and RanGTP. The trimeric complex transits through the NPC and is disassembled in the cytoplasm upon the hydrolysis of RanGTP. Export of importins is facilitated by binding with RanGTP. Figure adapted from (Yang et al., 2023).

Since SANS localizes to the cytoplasm and the nucleus, it must be transported to both compartments (Sorusch et al., 2017; Yildirim et al., 2021). Passive transport of SANS through the NPCs is unlikely due to its size, which exceeds the threshold of NPCs of 40-50 kDa (Yang et al., 2023). Moreover, previous data of our group indicate altered localization of pathogenic variants of SANS, which could be disease relevant (Sorusch et al., 2017). One NLS was previously predicted for SANS (Yildirim et al., 2021). However, the underlying mechanism of SANS' nuclear-cytoplasmic shuttling remains elusive, and the identification of SANS' NLS/NES is one of the aims addressed here.

5 Aim of the thesis

The primary goal of our lab is to decipher the molecular function of USH proteins within the cell, thereby gaining deeper insights into the pathomechanisms underlying USH. Here, I investigated the molecular interactions and nuclear transport mechanisms of the USH protein SANS. To achieve this, I concentrated on three aims:

1. Deciphering the interaction of SANS with the tri-snRNP proteins PRPF31 and PRPF6.
2. Elucidating the mechanisms underlying SANS and ANKS4Bs nuclear-cytoplasmic shuttling.
3. Deciphering the role of SANS in the transfer of splicing components.

To Aim 1: Deciphering the interaction of SANS with the tri-snRNP proteins PRPF31 and PRPF6.

Previous findings from our lab suggest a role for SANS in nuclear alternative splicing (Yildirim et al., 2021). This function is mediated by SANS interactions with other splicing proteins, primarily within the tri-snRNP complex. Two binding partners of SANS and members of the tri-snRNP complex are the pre-mRNA processing factors PRPF31 and PRPF6. We aimed to elucidate the interactions between SANS and the tri-snRNP proteins PRPF31 and PRPF6 (Fritze et al., 2023). We addressed this aim through utilizing *in vitro* based FRET interaction assays. These interactions were further validated and characterized using in silico methods, primarily through AlphaFold2. Further, pathogenic variants of SANS were used to detect potential alterations in SANS interaction to PRPF31 and PRPF6 in a disease background.

To Aim 2: Elucidating the mechanisms underlying SANS and ANKS4Bs nuclear-cytoplasmic shuttling.

As SANS is localized in both the nucleus and cytoplasm (Sorusch et al., 2017), it must undergo active nuclear-cytoplasmic transport. However, the underlying mechanism of SANS' nuclear-cytoplasmic shuttling remained unclear. Further, the cellular localization of SANS' paralog ANKS4B and the underlying regulation remained an open question. Therefore, we aimed to investigate the subcellular localization of SANS and ANKS4B, as well as the mechanisms that control this process (Fritze et al., 2024). By employing *in silico* techniques, we sought to identify the NLSs and NESs of SANS that mediate its nuclear-cytoplasmic shuttling. We validated those NLSs and NESs through *in vitro*

expression of SANS mutants. Further, pathogenic variants of SANS were utilized to elucidate possible alterations in SANS' subcellular localization. In addition, we deciphered the subcellular localization of SANS paralogue ANKS4B and its molecular differences in comparison to SANS, by using eYFP-tagged constructs.

To Aim 3: Deciphering the role of SANS in the transfer of splicing components.
In previous studies of our group a role of SANS in the nuclear mobility of the tri-snRNP complex was suggested (Yildirim et al., 2021). In particular, the transfer of the tri-snRNP complex from Cajal bodies to nuclear speckles appears to depend on SANS. Here, I aimed to explore the nuclear mobility of the tri-snRNP complex by the fluorescence observation of the nuclear protein PRPF31. I provides preliminary data on the role of SANS in PRPF31s mobility within Cajal bodies, as well as the alterations in this mobility caused by pathogenic variants of SANS (Chapter 7.3). In addition, I utilize a novel photoactivatable protein approach, by tagging PRPF31 with paGFP and observation in live cell. This approach allowes me to present preliminary data on the nuclear transfer of PRPF31 from Cajal bodies to nuclear speckles (Chapter 7.4). Showcasing the nuclear transfer of the tri-snRNP complex.

6 Publications

6.1 Publication 1: Pathogenic variants in USH1G/SANS alter protein interaction with Pre-RNA processing factors PRPF6 and PRPF31 of the spliceosome. (Fritze et al., 2023)

International Journal of
Molecular Sciences

MDPI

Article

Pathogenic Variants in *USH1G*/SANS Alter Protein Interaction with Pre-RNA Processing Factors PRPF6 and PRPF31 of the Spliceosome

Jacques S. Fritze, Felizitas F. Stiehler and Uwe Wolfrum *

Institute of Molecular Physiology, Johannes Gutenberg University Mainz, 55128 Mainz, Germany
* Correspondence: wolfrum@uni-mainz.de

Abstract: Pre-mRNA splicing is an essential process orchestrated by the spliceosome, a dynamic complex assembled stepwise on pre-mRNA. We have previously identified that *USH1G* protein SANS regulates pre-mRNA splicing by mediating the intranuclear transfer of the spliceosomal U4/U6.U5 tri-snRNP complex. During this process, SANS interacts with the U4/U6 and U5 snRNP-specific proteins PRPF31 and PRPF6 and regulates splicing, which is disturbed by variants of *USH1G*/SANS causative for human Usher syndrome (USH), the most common form of hereditary deaf–blindness. Here, we aim to gain further insights into the molecular interaction of the splicing molecules PRPF31 and PRPF6 to the CENTn domain of SANS using fluorescence resonance energy transfer assays in cells and in silico deep learning-based protein structure predictions. This demonstrates that SANS directly binds via two distinct conserved regions of its CENTn to the two PRPFs. In addition, we provide evidence that these interactions occur sequentially and a conformational change of an intrinsically disordered region to a short α-helix of SANS CENTn2 is triggered by the binding of PRPF6. Furthermore, we find that pathogenic variants of *USH1G*/SANS perturb the binding of SANS to both PRPFs, implying a significance for the *USH1G* pathophysiology.

Keywords: splicing; U4/U6.U5 tri-snRNP; Usher syndrome; protein–protein interaction; FRET; AlphaFold2; in silico structure predictions

Citation: Fritze, J.S.; Stiehler, F.F.; Wolfrum, U. Pathogenic Variants in *USH1G*/SANS Alter Protein Interaction with Pre-RNA Processing Factors PRPF6 and PRPF31 of the Spliceosome. *Int. J. Mol. Sci.* **2023**, *24*, 17608. https://doi.org/10.3390/ijms242417608

Academic Editor: Istvan Simon

Received: 1 November 2023
Revised: 8 December 2023
Accepted: 12 December 2023
Published: 18 December 2023

1. Introduction

Pre-mRNA splicing is a fundamental process in eukaryotic cells that almost exclusively occurs in the nucleus. It allows the inclusion/exclusion of exons/introns in the mRNA that can give rise to the synthesis of multiple alternative protein isoforms from a single genomic locus [1]. This process is catalyzed by the spliceosome, a highly dynamic macromolecular complex composed of five small nuclear ribonucleoproteins (U1, U2, U5, U4/U6 snRNPs) and numerous other polypeptides [2]. We have recently shown that the Usher syndrome type 1G (*USH1G*) protein SANS (scaffold protein containing ankyrin repeats and SAM domain) regulates pre-mRNA splicing [3]. Here, SANS mediates the intranuclear transfer of the spliceosomal U4/U6.U5 tri-snRNP complexes from the Cajal body and nuclear speckles, which is essential for the spliceosome activation [3,4]. We found that, during these processes, SANS interacts, among others, with the spliceosomal U4/U6 and U5 snRNP-specific proteins PRPF31 and PRPF6, respectively. *USH1G*/SANS deficiency altered the kinetics of spliceosome activation leading to perturbations in constitutive and alternative splicing of target genes, especially genes related to the human Usher syndrome.

Human Usher syndrome (USH) is a complex autosomal recessive rare genetic disorder (prevalence 1:5000–1:10,000) but represents the most common form of deaf–blindness [5]. To date, at least 11 genes have been classified into four clinical subtypes (*USH1-4*); among them, *USH1* is the most severe subtype with profound hearing loss, vestibular dysfunction, and pre-pubertal onset of retinal dysfunctions in the form of retinitis pigmentosa [5–7].

The human *USH1G* gene encodes SANS, a scaffold protein of ~52 kDa molecular weight consisting of 461 amino acids. SANS is composed of three N-terminal ankyrin repeats (ANK1–3), two central domains (CENTn and CENTc), a sterile alpha motif (SAM), and PDZ binding motif at the very C-terminal end (Figure 1) [8,9]. In the auditory hair cells, SANS is essential for the correct arrangement of the stereocilia in the hair bundles during development and for the composition and function of the mechanosensitive tip-link complex at the tip of the stereocilia [10–12]. Less is known about the function of SANS in the retina. Previous work indicated that SANS associates with cellular modules such as intracellular transport, endocytosis, and primary ciliogenesis [9,13–17]. Additionally, the role of SANS and other USH proteins in stabilizing the outer segment of photoreceptors has been hypothesized due to their presence in the calyceal processes, which are microvilli-like processes of the inner segment of photoreceptor cells [18]. However, *USH1G*/SANS is not primarily expressed in photoreceptor cells but in Müller glial cells of the retina, as recently highlighted by single-cell RNAseq data [19].

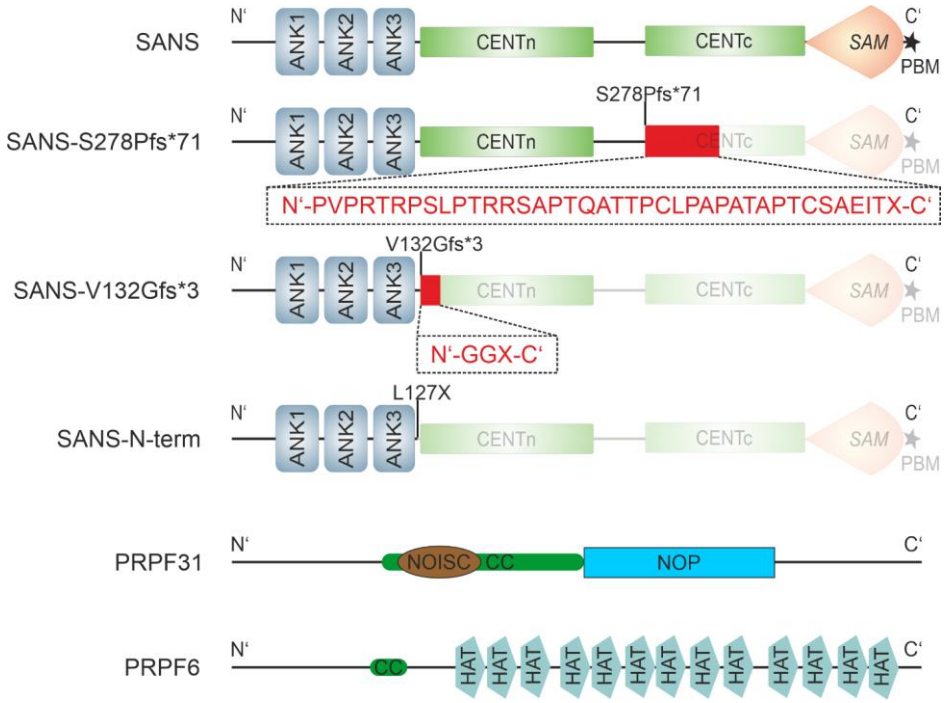

Figure 1. Domain structures of SANS variants and the pre-mRNA processing factors (PRPF) PRPF31 and PRPF6. Domain structure of SANS and USH-causing pathogenic variants SANS^{S278Pfs*71}, SANS^{V132Gfs*3}, SANS-Nterm, PRPF31, and PRPF6. SANS consists of three ankyrin repeats (ANK1–3), a central domain (CENT), divided into the N-terminal CENTn and the C-terminal CENTc, a sterile alpha motif (SAM), and PDZ binding motif (PBM, asterisk). Both USH-causing mutants, S278Pfs*71 and V132Gfs*3, are frameshift mutations, which lead to "missense extension" (red boxes and amino acid sequences below) and a premature stop in CENTc (S278Pfs*71) or CENTn (V132Gfs*), respectively. SANS-Nterm is an artificial construct missing CENTn and onward. PRPF31 consists of coiled-coil (CC, green) regions, a NOISC domain (brown), named after the central domain in Nop56/SIK1-like proteins, and a NOP domain (blue), a ribonucleoprotein (RNP) binding module, with both found in various pre-RNA processing ribonucleoproteins (InterPro: http://www.ebi.ac.uk/interpro/entry/InterPro/IPR012976 and IPR036070, accessed on 1 July 2023). PRPF6 exhibits thirteen half TPR (HAT) domains, as well as one CC domain.

In any case, the integrative scaffold functions of SANS are essential for the proper operation of diverse cellular modules, relying on context-dependent interactions with multiple protein partners. Other teams and ours have identified numerous proteins that bind to all domains and motifs of the SANS molecule [9,13,15,17,20–22]. These studies also

showed that the CENTn and CENTc domains are the preferential binding sites in SANS, with at least 50 different proteins binding to it [3,9,14,17,20]. Nevertheless, the mechanisms by which the CENTn and CENTc domains of SANS facilitate their interaction with multiple binding partners remain unexplained.

Here, we aimed to gain further insights into the molecular interaction of binding partners with the CENTn domain and to understand the effects of SANS-mediated splicing regulation. We investigated in detail the binary interaction of SANS with both PRPF31 and PRPF6 in cells using FRET assays and in silico deep learning-based protein structure predictions such as AlphaFold2-multimer and Metapredict [23,24]. Our data suggest that the SANS CENTn domain binds directly via two distinct conserved regions (CENTn1, CENTn2) to PRPF31 and PRPF6. We also provide evidence that these interactions occur sequentially and that PRPF6 binding introduces a conformational change of an intrinsically disordered region to an α-helix in SANS CENTn2. Finally, we found that perturbations in the binary interactions between the two PRPFs and pathogenic variants of *USH1G*/SANS were disturbed, implying a significance in the pathogenesis of *USH1G*.

2. Results

2.1. Binding of SANS to PRPF31 and PRPF6 in the Nucleus Revealed by FRET

We have previously demonstrated the interaction of the *USH1G* protein SANS with the splicing molecules PRPF31 and PRPF6 of the tri-snRNP complex by in vitro pull-down assays [3]. Here, we aimed to explore their binary binding in more detail by fluorescence resonance energy transfer (FRET) acceptor photobleaching assays in the cell [25]. For this, we co-expressed eYFP-SANS together with eCFP-tagged eCFP-PRPF31 or PRPF6-eCFP, in HEK293T cells. Confocal fluorescence microscopy showed that eYFP-SANS co-localized with both PRPF6-eCFP and eCFP-PRPF31, respectively, in the nucleus, as indicated by fluorescence intensity plots and confirmed by positive Pearson coefficient R values (Figure 2A,B). In addition, eCFP-tagged harmonin, a USH-related scaffold protein known to co-localize in situ and to interact with SANS [8,20,26], co-localized with co-expressed eYFP-SANS as expected (Figure 2C). Intriguingly, the co-localization of eYFP-SANS with harmonin-eCFP was predominantly in the cytoplasm. The triple transfection of PRPF6-eCFP, eYFP-SANS, and mRFP-PRPF31 showed co-localization of all three proteins inside the nucleus (Figure 2D), which was consistent with the localization of endogenous proteins as previously reported [3].

To study the binary interaction of SANS with both PRPFs in the cell, we performed FRET acceptor photobleaching assays in the nucleus (Figure 3A). FRET analyses revealed the interaction of the eCFP-eYFP FRET pairs SANS-PRPF31 and SANS-PRPF6 in nuclei (Figure 3B). The obtained FRET signals were at the same height as for the interaction between eYFP-SANS and the known SANS binding partner protein harmonin-eCFP in the cytoplasm (Figure 3B). In addition, we analyzed PRPF3, another PRPF of the spliceosomal tri-snRNP complex, previously shown not to interact with SANS as a negative control [3]. We did not observe notable FRET signals in assays with the SANS-PRPF3 eCFP-eYFP FRET pair (Figure 3C) and in all additional negative controls applied (Figure S1A–C). Taken together, the FRET-based interacting assays revealed specific binding of SANS to PRPF31 and PRPF6, respectively, in the nucleus.

During sequential spliceosome activation, the interaction of PRPF31 and PRPF6 as bridging factors between the small nuclear ribonucleoproteins snRNPs, U4/U6, and U5 of the tri-snRNP complex is essential [27]. This prompted us to test whether SANS interferes with the interaction between PRPF31 and PRPF6 within the tri-snRNP complex. As expected, we found significant FRET signals in HEK293T cells co-transfected with eCFP-PRPF31 and PRPF6-eYFP (Figure 3D). Additionally, expressed mRFP-SANS or mRFP alone did not alter the FRET signals for eCFP-PRPF31 and PRPF6-eYFP. Next, we conducted FRET analysis for eCFP-eYFP FRET pairs of SANS-PRPF31 in the presence of PRPF6-mCherry (Figure 3E). The FRET signals between eYFP-SANS and eCFP-PRPF31 were unaffected by PRPF6-mCherry (Figure 3E). However, co-expression of mRFP-PRPF31

significantly reduced FRET signals between SANS-PRPF6 FRET pairs, which was not observed in the presence of mRFP (Figure 3F). However, FRET efficiency decreased only by approximately 16%, which still indicates the interaction of SANS and PRPF6, but with lower affinity than in the absence of PRPF31. This decrease may indicate the competition of binding partners and/or a change in conformation of the tertiary complex of PRPF31-PRPF6 and SANS.

Taken together, these data suggest that the binary binding of SANS to PRPF31 is independent of PRPF6, but that PRPF31 interferes with the interaction of SANS with PRPF6 (Figure 3G).

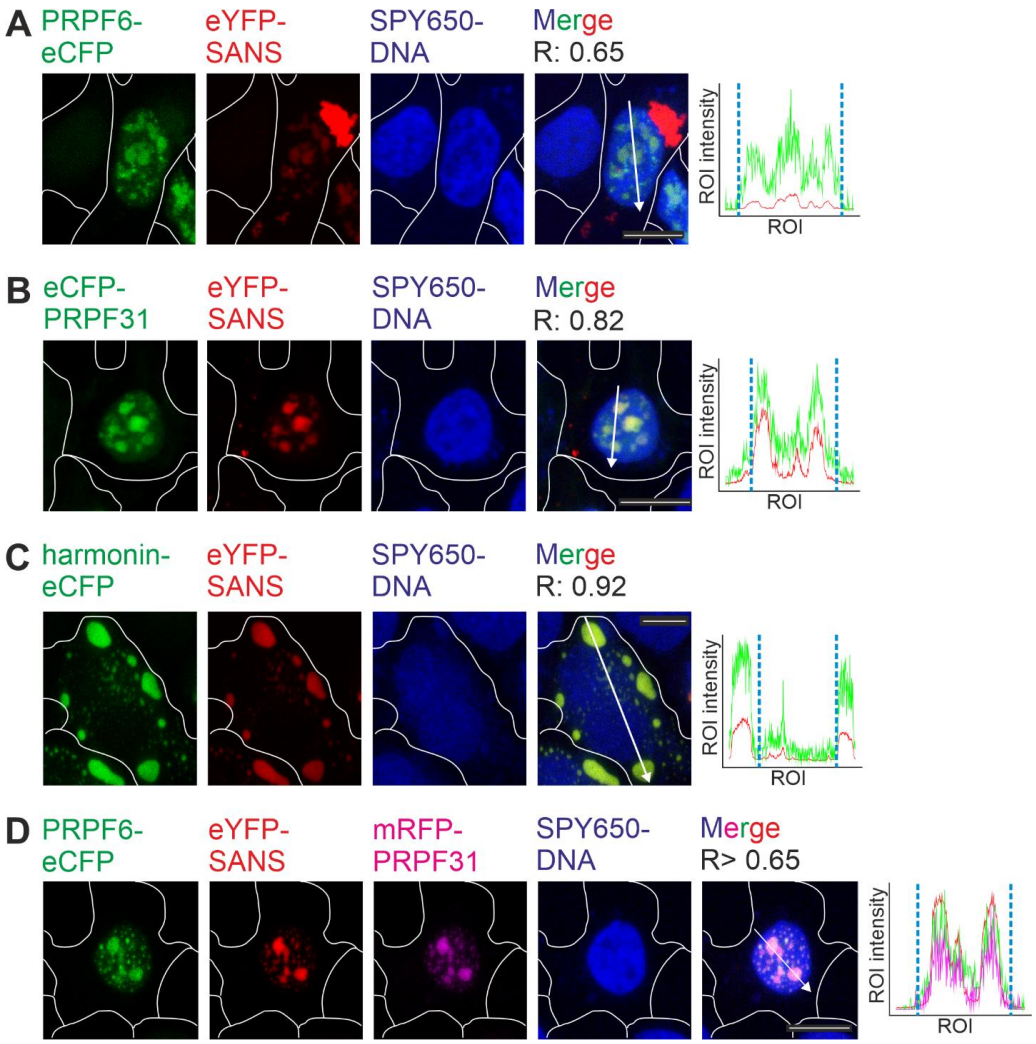

Figure 2. Co-localization of SANS and splicing proteins PRPF6 and PRPF31. (**A**–**D**) Confocal microscopy analyses of HEK293T cells co-transfected with eYFP-SANS and eCFP/mRFP tagged proteins, counterstained with SPY650-DNA as a nuclear marker. Fluorescence intensity plots of eYFP SANS (red) and transfected eCFP- (green) and mRFP-tagged (magenta) proteins for regions of interest (ROI) indicated by white arrows in merge images; blue dashed lines indicate nuclear extension. Positive Pearson coefficient R values indicate co-localization. (**A**) PRPF6-eCFP co-localized with eYFP-SANS in the nucleus. (**B**) eCFP-PRPF31 co-localized with eYFP-SANS in the nucleus. (**C**) *USH1C* protein harmonin-eCFP co-localized with eYFP-SANS, predominantly in the cytoplasm outside of the nucleus. (**D**) eYFP-SANS co-localized with PRPF6-eCFP and mRFP-PRPF31 in the nucleus of HEK293T cell in a triple transfection. White lines indicate cell borders. Example images of $n = 3$ experiments; scale bar = 10 µm.

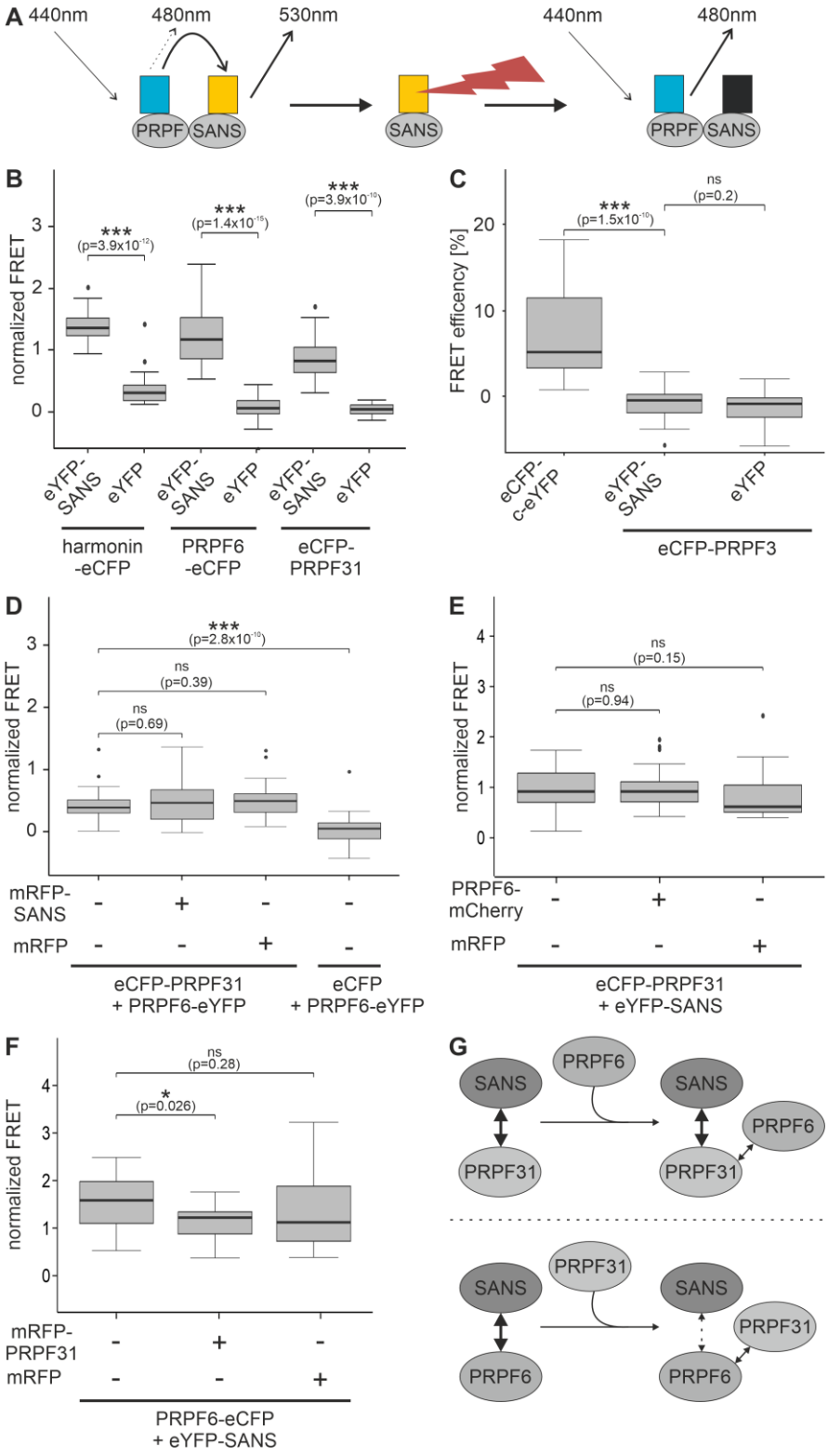

Figure 3. Interaction of SANS and binding partners analyzed by FRET acceptor bleach in HEK293T cells. (**A**) Illustration of the principle of the FRET acceptor bleach assay. Interaction of two proteins tagged with either eCFP (blue) or eYFP (yellow) leads to FRET (left). The acceptor (eYFP) is bleached (red flash symbol) (middle), which leads to increased emission of the donor (eCFP) (right) and no fluorescence of acceptor (black). (**B**–**F**) FRET assay in co-transfected HEK293T cells. In (**B**,**D**–**F**), FRET efficiencies were normalized to the fused eCFP-c-eYFP FRET pair (positive control), as shown in (**C**) and Figure S1. (**B**) FRET pairs eYFP-SANS-harmonin-eCFP, -PRPF6-eCFP, and -eCFP-PRPF31,

respectively, show a significant increase in the normalized FRET efficiencies compared to eYFP FRET pair negative controls. (**C**) FRET efficiency of eYFP-SANS-eCFP-PRPF3 shows a FRET efficiency similar to the eYFP negative control, which is significantly different from the positive control eCFP-c-eYFP. (**D**) FRET efficiencies of the eCFP-PRPF31-PRPF6-eYFP pair in the absence and presence of mRFP-SANS do not significantly differ. (**E**) Normalized FRET efficiencies of the eCFP-PRPF31-eYFP-SANS in the absence and presence of PRPF6-mCherry do not significantly differ. (**F**) Normalized FRET efficiency of the PRPF6-eCFP-eYFP-SANS is significantly decreased in the presence of mRFP-PRPF31. In (**E**,**F**), mRFP was used as a control for the third interaction partner. Outliers are shown as dots above/below the boxplots. Wilcoxon signed-rank test was performed for three independent experiments. (**G**) Schematic interaction of SANS, PRPF31, and PRPF6 from (**D**) to (**F**). SANS interaction with PRPF6 is decreased in the presence of PRPF31.

2.2. PRPF31 and PRPF6 Interact with Different Regions in SANS CENTn Domain

Our FRET experiments indicated that SANS interacts differently with PRPF31 and PRPF6. To explore the structural basis for this interaction, we used AlphaFold2-multimer as an in silico approach for protein–protein complex predictions [23]. The predicted structures are documented on GitHub (https://github.com/LabWolfrum/Fritze_et_al.2023.git). The AlphaFold2 structural predictions aligned to the structures of PRPF31 and PRPF6 previously obtained by cryoelectron microscopy ([28], PDB: 6QW6) (Figure S2A,B). For SANS, AlphaFold2 predicted a central unstructured intrinsically disordered region (IDR) flanked by an α-helix representing the N-terminus of CENTn and the SAM domain in the C-terminus (Figure S2C).

To analyze the protein complexes, we used AlphaFold2-multimer [23], which predicts an alignment error (PAE) representing the accuracy of the predicted models, summarized by the PAE_{mean} score for each model (Figure S3A). We compared our prediction workflow with the harmonin–SANS complex previously determined by X-ray crystallography as a benchmark [26]. AlphaFold2-multimer predicted a complex similar to the experimentally resolved structure, with a $PAE_{mean} \geq 12.24$ Å in the interaction region, namely, SANS-SAM/PBM and the N-terminal harmonin homology domain of harmonin (Figure S3B) [29]. It should be noted that during development, AlphaFold2 was trained on accessible PDB data [23,30], and the data for SANS/harmonin structures may have been among them.

AlphaFold2-multimer predicted low confidence ($PAE_{mean} \geq 25.66$ Å) for a complex of full-length PRPF31 and SANS, except for two small regions containing the N-terminal domains of both proteins (Figure S3C), namely, the N-terminal part of the CENTn domain (aa 128–173) of SANS and the NOP domain (aa 215–333) of PRPF31 (Figure 1). Subsequent AlphaFold2-multimer predictions of these areas predicted a complex of SANS CENTn and the PRPF31 NOP domain, with high confidence of a $PAE_{mean} \geq 11.83$ Å (Figure 4A). No other regions of SANS, such as the ankyrin repeats, CENTc domain, and SAM/PBM domain, were predicted in a complex with the PRPF31 NOP domain with such high confidence (Figure S3D–F). The amino acid sequence analyses of these domains predicted that the SANS CENTn-PRPF31 NOP complex is stabilized by multiple hydrophobic interactions (aa 140–165, Figure 4A and Table S2). In summary, these data suggest a protein complex of SANS N-terminal CENTn domain and PRPF31 NOP domain, stabilized by hydrophobic interactions.

AlphaFold2-multimer predictions for a complex of full-length PRPF6 and SANS were also of low confidence in the model ($PAE_{mean} \geq 31.02$ Å) (Figure S4A). However, AlphaFold2-multimer predicted a complex of the C-terminal part of PRPF6, containing HAT domains, and a short region of SANS CENTn (aa 166–194) domain, with high confidence of a $PAE_{mean} \geq 10.21$ Å (Figure 4B). Interestingly, AlphaFold2-multimer predicted that a short α-Helix (aa 183–198) was formed in this complex by a part of the unstructured region of SANS CENTn domain. No other region of SANS could be predicted with PRPF6 with such high confidence (Figure S4B–E). Taken together, our in silico experiments suggest two

different regions of the CENTn domain, hereafter referred to as CENTn1 (aa 128–173) and CENTn2 (aa 174–243). These data suggested direct binding of PRPF31 and PRPF6 to SANS. PRPF31 interacted exclusively with CENTn1, while PRPF6 interacted predominantly with CENTn2 and seven residues of CENTn1, indicating that the binding site for both PRPFs do not overlap (Figure 4C).

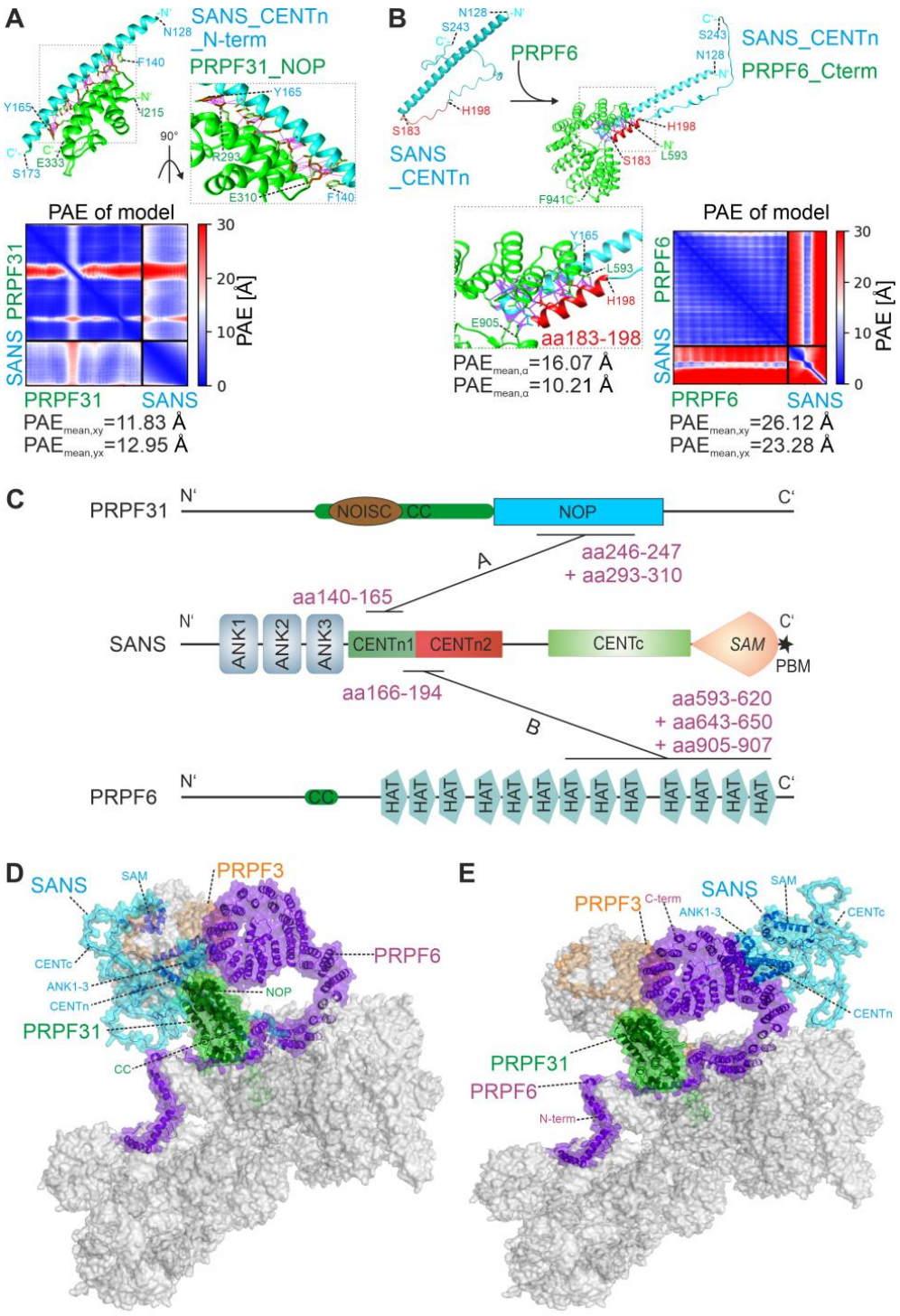

Figure 4. Molecular structure predictions of the interaction of SANS with PRPF31 and PRPF6. (**A**,**B**) In silico predictions of SANS and PRPFs complexes by AlphaFold2. Purple lines indicate hydrophobic interactions (Table S2). (**A**) PRPF31 NOP domain (green, amino acids (aa) 215–333) binds to the N-terminal part of SANS CENTn (blue, aa 128–173). Close-up is shown on the right (zoomed box).

(**B**) PRPF6 binds via aa 593–941 of the C-terminus (green) to the SANS CENTn domain (blue, aa 128–243); PAE is predicted with high confidence for a small region of the two proteins. In SANS CENTn, a small α-Helix (red, aa 183–198) is formed from an unstructured region upon interaction with PRPF6 (zoomed box). (**C**) Illustration of the binding regions on the domain structure of SANS, PRPF31, and PRPF6 predicted (**A**,**B**); aa of binding sites are indicated in purple. Note: SANS CENTn is divided into CENTn1 (aa 128–173) and CENTn2 (aa 174–243) based on structural differences (see Figure 5A,B). (**D**,**E**) Illustration of SANS binding to the U5.U4/U6-tri-snRNP complex (cryoEM structure, [28], PDB: 6QW6), as predicted in (**A**,**B**). (**D**) SANS (blue) fits into the tri-snRNP complex in a small pocket between PRPF31 (green) and PRPF6 (purple) when interacting with PRPF31. (**E**) SANS position in the tri-snRNP complex changes when interacting with PRPF6.

To predict the integration of SANS with the tri-snRNP complex, we made use of the AlphaFold2-multimer predictions for SANS structural complexes with PRPF31 and PRPF6 described above (Figure 4A,B) and fitted these in the experimental confirmed tri-snRNP complex ([28], PDB: 6QW6) (Figure 4D,E). However, SANS did not fit into the structure of the tri-snRNP complex in a single conformation based on the predicted interactions with both PRPFs. Also, it should be noted that PRPF31 interaction with SANS (Figure 4D) may clash with SNU13 and the U4-snRNA in the U4.U6 di-snRNP. Nevertheless, in both predicted conformations, SANS was structurally separated from PRPF3. Taken together, these data suggest a spatial separation of SANS binding platform in the tri-snRNP complex.

2.3. In Silico Analysis Predicts Evolutionary Conserved Multi-Conformational Intrinsically Disordered Regions (IRDs) for SANS

To decipher the structural characteristics of SANS domains, we used the in silico tool Metapredict [24] in combination with the pLDDT scores of AlphaFold2 (Figure 5A). Metapredict is a bidirectional recurrent neural network that gives a predicted disordered value for each residue. While high values in Metapredict indicate intrinsically disordered regions (IDRs), the pLDDT scores of AlphaFold2 decrease in IDRs [31].

Metapredict and AlphaFold2 predicted the ankyrin repeats (aa 1–126), the CENTn1 (aa 128–177), and the SAM domain (aa 386–447) as folded and three unfolded IDRs in SANS, namely, the CENTn2 domain (aa 178–243), the CENTc domain (aa 278–385), and the PBM (aa 451–461) (Figures 1 and 5A). These predictions also strengthen the observation that the SANS CENTn domain consists of two different regions: a structured region (CENTn1, aa 128–177) and an IDR (CENTn2, aa 178–243).

To analyze the evolutionary conservation of SANS domains, we performed multiple sequence alignments. The alignment of SANS amino acid sequences of more than 98 mammals and 266 vertebrate species demonstrated that SANS overall is highly conserved among species (Figure 5B; Figure S5A and Table S3). Even IDRs, which are commonly known for evolutionary low conservation [32], namely, the CENTn2, CENTc, and the C-terminal PBM, were highly conserved overall among vertebrate and mammal species (Figures 5B and S5A).

Next, we analyzed the physicochemical properties of the SANS CENTn2 domain by applying the CIDER analyzer [33]. The CENTn2 of SANS was predicted by CIDER to be a Janus sequence (Figure 5C). Janus sequences can change their structure depending on the binding partner [34]. Furthermore, CIDER predicted that SANS CENTn2 is positively charged overall (Figure S5B,C), a feature that is known to foster protein binding [35].

In summary, our results indicate three distinct conserved IDRs in CENTn2, CENTc, and PBM of SANS. Moreover, the physicochemical properties predicted for SANS CENTn2 indicate a high potential for protein–protein interactions, which is confirmed by the binding of PRPF6 to this domain described above.

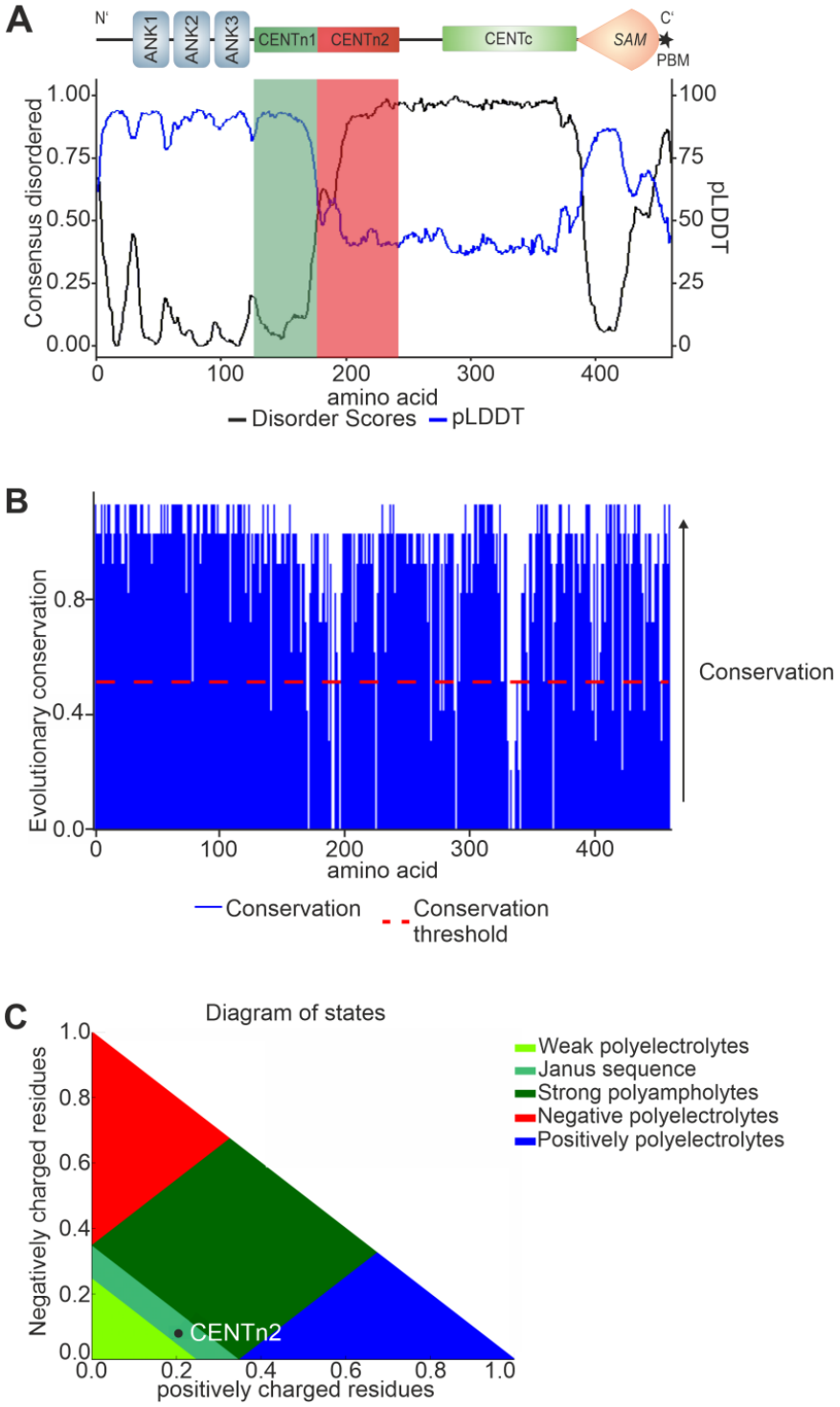

Figure 5. Predictions of SANS domain structure and their evolutionary conservation. (**A**) SANS predicted disordered state by Metapredict (black line) and AlphaFold2 (blue line). An increase of Metapredict prediction (disordered score) above 0.5 or a decrease in the AlphaFold2 prediction (shown by pLDDT) below 50 indicates an intrinsically disordered region (IDR). Metapredict and AlphaFold2 predicted SANS CENTn1 (green box) as structured and SANS CENTn2 (red box) as IDR. (**B**) Evolutionary conservation (blue) of SANS proteins for 266 vertebrates. The conservation threshold (red dotted line) indicates high conservation of SANS in vertebrates, except for small regions of CENTn and CENTc domains. (**C**) SANS CENTn2 (black dot) in a Das–Pappu plot predicted by CIDER is identified as a flexible Janus sequence.

2.4. USH-Causing Pathogenic Variants of SANS Show Altered Interaction with PRPFs

We have previously shown that pathogenic variants in the *USH1G* gene interrupt the interactions in the ternary USH protein complex of SANS, *USH2A*, and whirlin [9]. Here, we tested whether *USH1G* pathogenic frameshift mutations *USH1G*/SANS^{V132Gfs*3} and *USH1G*/SANS^{S278Pfs*71} (www.LOVD.nl/USH1G, accessed on 25 July 2023), which lead to a premature stop in the CENTn1 or CENTc domain, respectively (Figure 1), also alter the binary interaction between SANS and PRPFs.

We co-expressed eYFP-tagged versions of both *USH1G*/SANS mutations, with either eCFP-tagged PRPF31, PRFP6, or harmonin as control, in HEK293T cells (Figure S6). Confocal microscopy and fluorescent intensity plots demonstrated that both *USH1G*/SANS variants still co-localized with both PRPFs in the nucleus, confirmed by the positive Pearson coefficients (R) (Figure S6A,B). However, while in co-expression with the *USH1G*/SANS variants, many PRPF6 droplets were still distributed all over the nucleus, as in the *USH1G*/SANS wildtype expressing cells, where fluorescent PRPF31 appeared in a few larger droplets in the nucleus. The expression of *USH1G*/SANS variants destroyed the specific localization of harmonin in the cytoplasm and led to an even distribution of the proteins throughout the cell (Figure S6C).

Subsequent FRET assays with eYFP-SANS^{S278Pfs*71} and both eCFP-tagged PRPFs showed significant reductions in FRET efficiencies compared to eYFP-SANS (Figure 6A,B). This indicated that the S278Pfs*71 mutation disrupts the binding of SANS to PRPF31 and PRFP6. However, we predicted no change in the IDR for SANS^{S278Pfs*71} compared to SANS (Figure S7A).

In FRET assays with eYFP-SANS^{V132Gfs*3} and PRPF6-eCFP, FRET efficiencies were also significantly reduced compared to the efficiency of eYFP-tagged full-length SANS and PRPF6-eCFP (Figure 6C).

Interestingly, in FRET assays with eYFP-SANS^{V132Gfs*3} and eCFP-PRPF31, FRET efficiency was not reduced, indicating a binding of PRPF31 also to the N-terminal part of SANS (Figure 6D). Since this finding was contradictory to our previous results from in vitro pull-down assays [3], we validated this observation by additional FRET assays with the truncated eYFP-SANS-Nterm construct (Figure 1) and eCFP-PRPF31 (Figure 6E). eCFP-eYFP FRET pairs of SANS-Nterm-PRPF31 showed no reduction of FRET efficiency compared to eYFP-tagged full-length SANS supporting binding of PRPF31 to the N-terminal part of SANS, which mainly consists of three ankyrin repeats (Figure 1).

Both *USH1G*/SANS variants (V132Gfs*3 and S278Pfs*71) did not show a significant FRET signal in all FRET controls performed (Figure S7B,C). In addition, FRET assays with harmonin, which are known to bind to the SAM/PBM region of the C-terminus of SANS, which is absent in both *USH1G*/SANS variants, showed significantly reduced efficiencies compared to full-length eYFP-SANS (Figure S7D). Thereby, interaction with both fluorescent-tag proteins, eYFP and eCFP, could be excluded. Moreover, we confirmed the correct expression of all eYFP-SANS constructs via Western blot analysis (Figure S7E). Further, AlphaFold2-multimer did not predict a model for PRPF31 full-length or coiled-coil domain and SANS-Nterm with high confidence (Figure S8A,B).

Taken together, our data showed that both pathogenic variants, *USH1G*/SANS^{V132Gfs*3} and *USH1G*/SANS^{S278Pfs*71}, disrupted the interaction with PRPF6. In contrast, the interaction of PRPF31 was disrupted for *USH1G*/SANS^{S278Pfs*71}, but not with the shorter eYFP-SANS^{V132Gfs*3} revealing a binding site for PRPF31 in the N-terminal part of SANS alternative to the binding to SANS CENTn1.

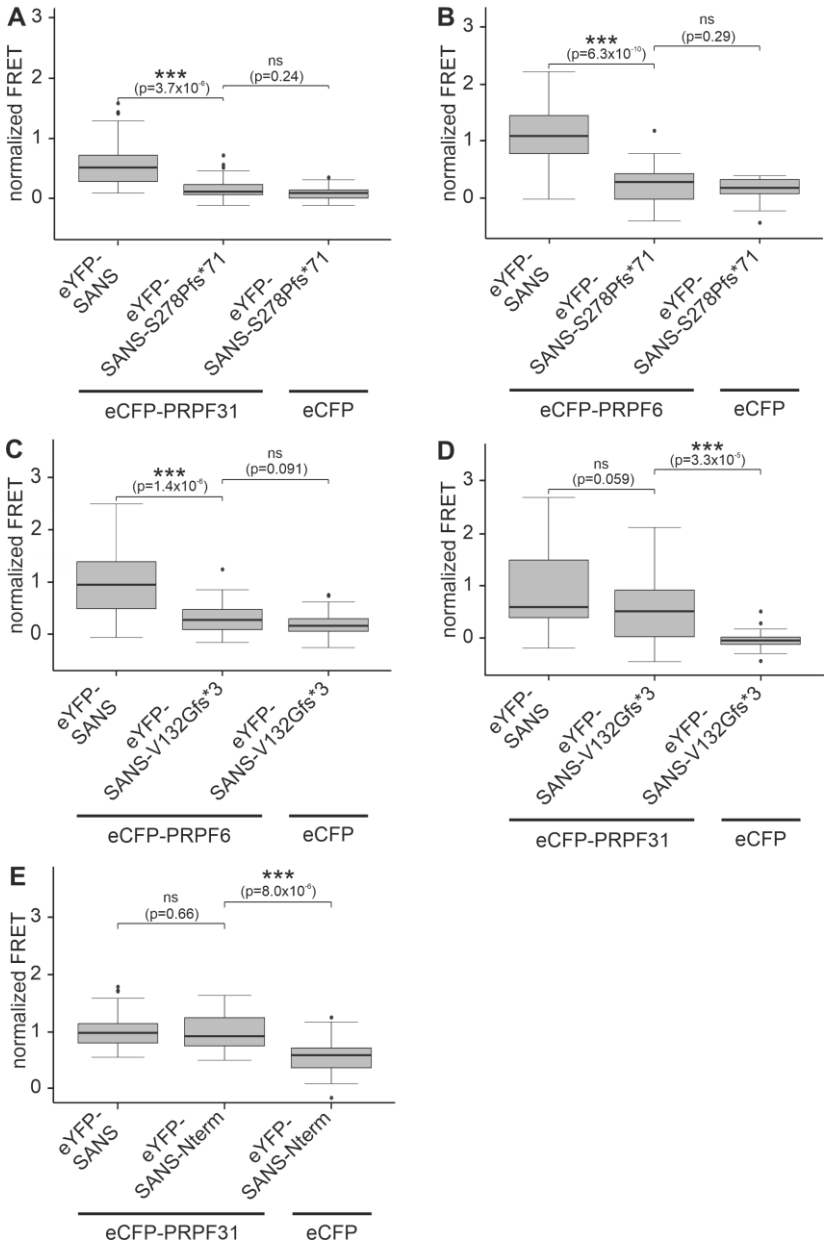

Figure 6. Interaction of pathogenic variants of *USH1G*/SANS to PRPF31 and PRPF6 analyzed by FRET in HEK293T cells. (**A**,**B**) FRET assays with eYFP-SANS, eYFP-SANS^{S278Pfs*71} paired with eCFP-PRPF31 (**A**), and PRPF6-eCFP (**B**) normalized to FRET of eCFP-c-eYFP fused tandem pair. Normalized FRET efficiencies are significantly decreased in both SANS^{S278Pfs*71}-PRPF pairs to levels of the negative control eYFP-SANS^{S278Pfs*71}-eCFP compared to eYFP-SANS, indicating no binding of eYFP-SANS^{S278Pfs*71} to both PRPFs. (**C**) Normalized FRET efficiency is also decreased in the eYFP-SANS^{V132Gfs*3}-PRPF6-eCFP pair, indicating no binding of SANS^{V132Gfs*3} to PRPF6. (**D**,**E**) Normalized FRET efficiencies of eYFP-SANS^{V132Gfs*3} (**D**) and eYFP-SANS-Nterm (**E**) paired with eCFP-PRPF31 are similar to eYFP-SANS-eCFP-PRPF31 pair values, but significantly different from eCFP control pairs, indicating no binding of both truncated variants to PRPF31. Outliers are shown as dots above/below the boxplots. Wilcoxon signed-rank test was performed for three independent experiments.

3. Discussion

Pre-mRNA splicing is a fundamental process in eukaryotic cells that almost exclusively occurs in the nucleus, catalyzed by the spliceosome, a highly dynamic macromolecular complex composed of small nuclear ribonucleoproteins (snRNPs) and numerous other polypeptides [1]. We previously identified the *USH1G* protein SANS as one of these proteins

regulating pre-mRNA splicing by mediating the intranuclear transfer of the spliceosomal U4/U6.U5 tri-snRNP complexes from the Cajal body and nuclear speckles essential for the spliceosome activation [3]. During these processes, SANS interacts through the CENTn domain with the spliceosomal U4/U6 and U5 snRNP-specific proteins PRPF31 and PRPF6, respectively [3]. However, questions of the mode of binding of SANS to PRPFs, by direct or mediated by other spliceosome proteins, or even by RNA, remained unanswered. In addition, the exact binding site in the CENTn domain of the SANS protein, which comprises more than one-fourth of the entire protein, has not yet been determined.

In our study, we found FRET efficiencies for both eCFP-eYFP FRET pairs, PRPF31-SANS and PRPF6-SANS, in the range of the tandem eCFP-c-eYFP construct (positive control), were significantly higher than the negative controls. Since positive FRET signals are only achieved at a distance of 8–10 nm or less between the two complex partners [25,36], these findings not only confirm the interactions of PRPF31 and PRPF6 to SANS, but also suggest that both PRPFs bind directly to SANS without any mediator involved as previously considered [37]. Microscopic analyses, including fluorescence intensity plots and consistently positive Pearson coefficient R values, demonstrated the co-localization of PRPFs with SANS in the cell nucleus, further supporting a direct binary interaction.

Using AlphaFold2-multimer, we pinpointed the binding of PRPF31 and PRPF6 to different, separate regions of the CENTn domain of SANS, namely, to aa 140–165 of the long α-helix of CENTn1 and to aa 166–194, respectively. The predicted binding of PRPF31 via the NOP domain to the helical structures of SANS was also found for the interaction of PRPF31 with the helical structures in the small nuclear ribonucleoprotein 13 (SNU13) (also known as 15.5k protein or NHP2-like protein 1) of the U4/U6.U5 tri-snRNP complex [28]. Both observations are in line with the common interaction modes of NOP domains present in other ribonucleoproteins [38].

For the interaction of PRPF6 with SANS, we confirmed C-terminal HAT domains as the interacting region in PRPF6 previously reported [3]. These domains bind to the seven amino acids of the α-helix of SANS CENTn1 but mainly to a region of SANS CENTn2, which was consistently predicted as an evolutionary conserved IDR by Metapredict and AlphaFold2. Here, we note that the model of the PRPF6-SANS complex had low overall confidence by AlphaFold2-multimer, probably since AlphaFold2-multimer is trained on structured protein data [23]. Nevertheless, the model is supported by the ability of PRPF6 to bind IDRs in other proteins, such as the translation initiation factor eIF4E enrolled in splicing [39].

Our in silico predictions by AlphaFold2-multimer also suggested that this IDR of the CENTn2 forms a newly derived small α-helix upon binding to PRPF6. This structural change is supported by the observation that SANS CENTn2 represents a highly conserved Janus sequence, a protein region with the characteristic to specifically change the structure by binding different proteins [34]. The properties of a Janus sequence in the SANS CENTn domain are probably also the basis for allowing the interaction of the numerous additional binding partners that have been previously identified [3,9,14,21].

Although our data consistently indicate that the binding of SANS to PRPF31 and PRPF6 is mediated by distinct subdomains of the SANS molecule, we observed a decrease in FRET efficiency for the PRPF6-SANS pair upon co-transfection with PRPF31, indicating a competition between the two PRPFs. This finding is in line with the fact that the complexes predicted for SANS and the two PRPFs did not simultaneously fit into the structure of the U4/U6.U5 tri-snRNP complex [28]. These results suggest that SANS molecules bind to both PRPFs separately, either sequentially in the tri-snRNP complex or independently to the snRNP subunits. Sequential binding of proteins to the tri-snRNP complex was previously shown for U6-LSm ring proteins, which also change their spatial arrangement in the tri-snRNP complex, binding first to PRPF6 and then to PRPF3 during the formation of spliceosomal complex B [40]. Nevertheless, separate binding of SANS to the two PRPFs could also occur during the formation of the tri-snRNP complex in the Cajal bodies when the U4/U6 snRNP containing PRPF31 and U5 snRNP harboring PRPF6 maturate separately

from each other [41]. Alternatively, in the tri-snRNP complex, SANS may preferentially bind to PRPF31, as indicated by our FRET data, and interacts with PRPF6 during the recycling process of the tri-snRNP complex components after activation of the spliceosome when sufficient free U5 snRNP/PRPF6 is present [2,42]. Although the latter alternative is supported by previous work showing that SANS deficiency does not affect the maturation of the tri-snRNP complex but does affect the recycling of U5-snRNP after activation of the spliceosome [3], in the tri-snRNP complex, the SANS binding site of PRPF31 might already be occupied by SNU13 and U4-snRNA, which could interfere with the binding of SANS [28].

More than 70 pathogenic variants in *USH1G*/SANS have been identified thus far in *USH1* patients ([43]; www.LOVD.nl/USH1G, accessed on 25 July 2023). However, the molecular mechanisms underlying the pathophysiology caused by these defects remain poorly understood. Our previous study provided evidence that SANS is part of the pre-mRNA splicing machinery and demonstrated that pathogenic variants in *USH1G*/SANS, including both frameshift mutants, *USH1G*/SANS^{V132Gfs*3} and *USH1G*/SANS^{S278Pfs*71}, investigated here, alter the pre-mRNA splicing of target genes [3]. These genes include *USH1C*, which is frequently alternatively spliced in the human retina [3,44]. Present FRET assays showed that for both pathogenic variants, the binding of PRPF6 was disrupted. *USH1G*/SANS^{S278Pfs*71} did not interact with either PRPF6 or PRPF31 in the cell, although the binding sites for both PRPFs in the CENTn domain are still present in the truncated SANS variant. Neither Metapredict nor AlphaFold2 predicted structural changes in *USH1G*/SANS^{S278Pfs*71} that could interfere with the binding of the two PRPFs. However, the content of proline residues in the frameshift sequence changes from 2 to 9 in *USH1G*/SANS^{S278Pfs*71}, which might lead to steric changes in the CENTn and CENTc domains and the binding sites for the PRPFs interfering with the binding of PRPF6 and PRPF31.

The short, truncated SANS variants, SANS^{V132Gfs*3} and the SANS-Nterm construct, lack the entire CENTn1 domain, which we identified above as the binding site of PRPF31, and all other downstream domains. However, both truncated SANS molecules consistently interact with PRPF31 in present FRET assays in cells, which was previously not found in in vitro pull-down assays [3]. The interaction of PRPF31 and SANS^{V132Gfs*3} is in line with the co-localization of both polypeptides in the nucleus of the cell observed by our microscopy analyses. Consequently, this novel finding suggests a binding site for PRPF31 in the three ankyrin repeats of the N-terminal portion of SANS alternative to SANS CENTn1. Ankyrin repeats are common protein–protein interaction platforms [45], and we have recently demonstrated that a set of intraflagellar transport (IFT) molecules bind to the ankyrin repeats of SANS [17]. Unfortunately, we failed to predict a site for PRPF31 that can bind to the region of ankyrin repeats in the N-terminus of SANS using the prediction tools employed.

In recent years, pathogenic variants leading to retinitis pigmentosa (RP) have been associated with many genes encoding proteins of the U4/U6.U5 tri-snRNP complex [4,46,47]. Besides PRPF31 (RP11) and PRPF6 (RP60), this list includes several other components, such as PRPF8 (RP13), PRPF3 (RP18), SNRNP200 (RP33), and PRPF4 (RP70). Here, we showed that mutations in *USH1G*/SANS lead to disruption of binary binding properties with the key molecules of the U4/U6.U5 tri-snRNP complex, PRPF31 and PRPF6. Vice versa, several pathogenic RP mutations in the genes of the two PRPFs are also located in binding sites to SANS ([48]; https://www.hgmd.cf.ac.uk/ac/index.php, accessed on 27 July 2023) and most likely also result in alterations in their interaction with SANS. Perturbations in the molecular interactions between the components of the U4/U6.U5 tri-snRNP complex are consistent with the fact that mutations in PRPF6, PRPF31, and *USH1G*/SANS have almost identical effects on splicing and that similar pathomechanisms leading to RP also cause similar retinal phenotypes.

Alternative splicing certainly increases the diversity of the transcriptome and proteome. Compared to other tissues, the retina exhibits the highest rates of alternative splicing [49,50]. Specific splicing programs are essential for the function and maintenance of the retina, which is uniquely regulated in a highly complex manner [51,52]. Thus, alterations in the splicing machinery may affect the retina more prominently than other tissues, which may explain why pathogenic variants in *USH1G* and in the genes of other splicing factors predominantly lead to retinal defects.

4. Materials and Methods

4.1. DNA Constructs and Primers

All nucleic acids used are listed in Table S1.

4.2. Cloning

cDNAs for expression of proteins were obtained by RT-PCR from human HEK293T cells and cloned into pENTR™, as described by the manufacturer (Thermo Fisher, Karlsruhe, Germany, #K240020). Gateway™ LR reaction into the appropriate destination vector was performed according to the manufacturer's protocol (Thermo Fisher, #11791020). USH-causing mutants and SANS-Nterm, PRPF31, and PRPF6 were cloned into pENTR™, with the template described previously [3]. eCFP-c-eYFP was cloned from the eYFP vector into the pDest vector with eCFP.

4.3. Cell Culture and Cell Lines

Dulbecco's modified Eagle's medium (DMEM #31966021) containing 10% heat-inactivated fetal calf serum (FCS) (Thermo Fisher #A4766801 or Cytiva, Freiburg, Germany, #SV30160.03) was used to culture HEK293T cells (ATCC: CRL-3216). Cells were fixed with 4% PFA in PBS for 10 min at room temperature. Nuclear DNA was stained by SPY650-DNA (TebuBio, Offenbach, Germany, #SC501).

4.4. Fluorescence Co-Localization Observation

HEK293T cells were seeded in 24 well plates with a density of 40,000 cells/well. Cells were transfected with Lipofectamine™ LTX, as described by the manufacturer (Thermo Fisher #15338100). Fixed HEK293T cells were observed with a Leica TCS SP5. Images were analyzed with Fiji 64 v5 [53]. The Pearson coefficient was performed with the Fiji Plugin *Coloc 2* for the whole nucleus. The intensity plot was performed over the indicated region of interest with the Fiji Plugin *Plot Profile*.

4.5. Fluorescence Resonance Energy Transfer (FRET) Acceptor Photobleaching Assay

HEK293T cells were seeded in six well plates with a density of 500,000 cells/well. Cells were transfected with Lipofectamine™ LTX, as described by the manufacturer (Thermo Fisher #15338100). Fixed HEK293T cells were analyzed with a Leica TCS SP8 and FRET acceptor photobleaching was performed following the Leica protocol (https://downloads.leica-microsystems.com/TCS%20SP8/Application%20Note/FRET_AB_with%20SP8-AppLetter_EN.pdf, accessed on 1 January 2023). eCFP was used as the donor (D) and eYFP as the acceptor (A). The acceptor was bleached at 100% laser intensity for 10 repeats. FRET efficiency was calculated via: $FRET_{eff} = \frac{(D_{post} - D_{pre})}{D_{post}}$. To exclude cellular structure, the mean of six regions of interest (ROI) in the bleached area was calculated and FRET efficiency of an unbleached region ($\geq$3 µm away from bleached ROI) was subtracted from the mean. Bleach efficiency was calculated via the formula $Bleach_{eff} = \left(1 - \frac{A_{post}}{A_{pre}}\right) * 100$. Only ROIs with >60% bleach efficiency were used for analysis. Data were normalized by the positive control eCFP-c-eYFP if indicated. Example images of FRET acceptor bleaching are shown in Figure S9.

4.6. AlphaFold2-Multimer

AlphaFold2-multimer prediction was performed using the hetero-oligomer options of ColabFold [54]. The FASTA sequence of the respective protein was used from UniProt (https://www.uniprot.org, accessed on January–April 2023) and a colon between the respective sequences simulated complexes. The following sequences were used: SANS: Q495M9; PRPF31: Q8WWY3; PRPF6: O94906; harmonin: Q9Y6N9. AlphaFold2 notebook was used in the ColabFold version (https://colab.research.google.com/github/sokrypton/ColabFold/blob/main/AlphaFold2.ipynb#scrollTo=G4yBrceuFbf3, accessed on 12 July 2023) and the standard options were extended by the template mode pdb70/pdb100, model type AlphaFold2-multimer_v2 recycling 24 times. Predicted structures are documented in GitHub (https://github.com/LabWolfrum/Fritze_et_al.2023.git). Structures were visualized, inspected, and superimposed using PyMOL (https://pymol.org/2, accessed on 1 August 2022, version: 0.99rc6) or UCSF Chimera V5 [55], which was also used to generate all structure images. PAE_{mean} was calculated as the mean of all PAE in the corresponding PAE plot area. Contacts for some protein complexes (Table S1) were predicted by the UCSF Chimera tool "Find Clashes/Contacts" (https://www.cgl.ucsf.edu/chimera/docs/ContributedSoftware/findclash/findclash.html, accessed on 3 March 2023). The following options were chosen: themselves, contact (default criteria −0.4). As output, an overlap and a distance value can be observed.

The predicted protein complexes were fitted to a previously published PDB structure of the human tri-snRNP complex ([28], PDB: 6QW6).

4.7. Evolutionary Conservation

A previously described protocol was used as a foundation [56]. The complete code can be found on GitHub (https://github.com/LabWolfrum/Fritze_et_al.2023.git). The evolutionary conservation was performed with the help of Jupyter Notebook and Jalview [57]. Python code was designed with the help of ChatGPT-3.5 (OpenAI). For graphs, areas not present in human SANS were excluded.

4.8. Western Blot

HEK293T cells were seeded in six well dishes with a confluency of 500,000 cells per/well. Cells were transfected with Lipofectamine^{TM} LTX, as described by the manufacturer (Thermo Fisher #15338100). Cells were lysed 24 h after transfection with TritonX-100, protein amount was measured with a BCA assay, and proteins were eluted with 5x Laemmli buffer, separated by SDS-PAGE followed by Western blotting. Monoclonal mouse-anti-GFP (cross-reaction to eYFP, Proteintech, Planegg-Martinsried, Germany # 66002-1-Ig) was used.

4.9. Additional Bioinformatic Analyses

CIDER was accessed via the online platform (http://pappulab.wustl.edu/CIDER/, accessed on 2 February 2023) and the FASTA sequence was analyzed with default options. SANS USH-causing mutants were chosen through the online Usher syndrome database (www.LOVD.nl/USH1G, accessed on 25 July 2023). Metapredict was used by the Python library option [24]. PDB structures were obtained from the PDBe webserver (https://www.ebi.ac.uk/pdbe/, accessed in March 2023).

4.10. Statistics

Statistical analysis was performed with R-Studio version 4.3.2 [58]. The statistical methods and the significance criteria are listed in corresponding individual legends. Results are shown as a boxplot of data from at least three separate experiments. Significance was determined as: * $p \leq 0.05$, ** $p \leq 0.009$, *** $p \leq 0.0009$.

5. Conclusions

Our data strengthen the evidence that SANS participates in alternative splicing by interaction with components of the U4/U6.U5 tri-snRNP complex. For this SANS directly

binds with different binding sites of its CENTn to the splicing factors PRPF31 and PRPF6. Our data also suggest that SANS molecules bind sequentially to the two PRPFs in the tri-snRNP complex (Figure 7). Finally, we provide evidence that perturbations in the molecular interaction of SANS with both PRPF molecules underlie the pathophysiology of pathogenic variants in *USH1G*/SANS, leading to the ocular phenotype in USH1.

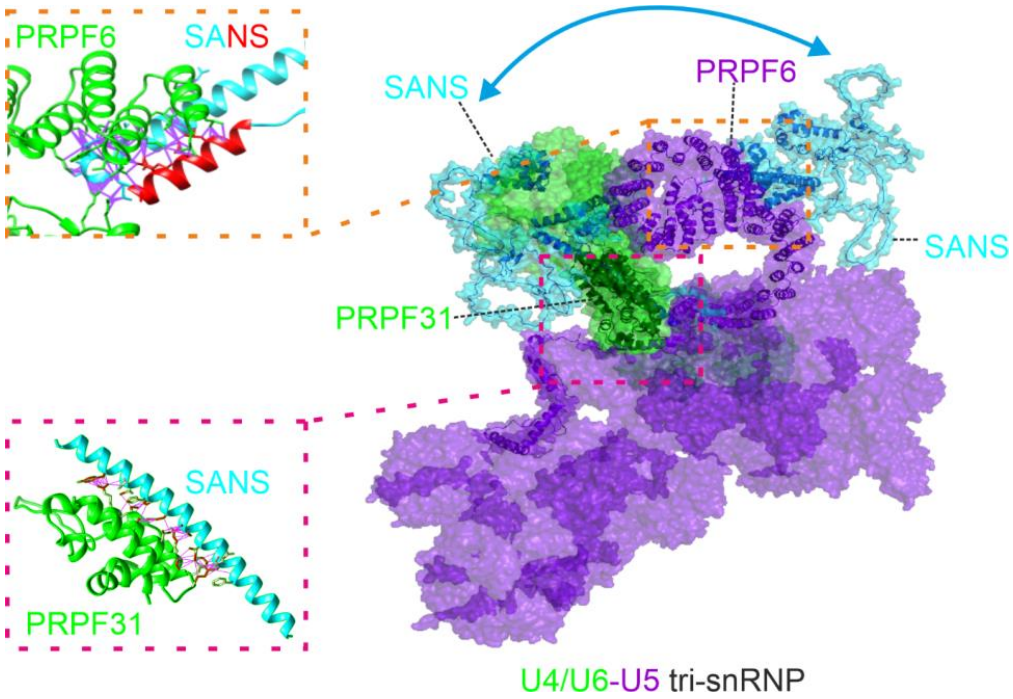

Figure 7. Schema of proposed conformation of SANS in the tri-snRNP complex. SANS interacts with PRPF31 and PRPF6 in the tri-snRNP. Two conformations of SANS are used to bind to either PRPF6 or PRPF31, respectively.

Supplementary Materials: The supporting information can be downloaded at https://www.mdpi.com/article/10.3390/ijms242417608/s1.

Author Contributions: Experiments, J.S.F.; cloning, F.F.S.; FRET assays, F.F.S.; study designs, J.S.F. and U.W.; writing—original draft preparation, J.S.F. and U.W. All authors have read and agreed to the published version of the manuscript.

Funding: This research was funded by the FAUN-Stiftung, Nuremberg, the Foundation Fighting Blindness (FFB) [PPA-0717-0719-RAD], and the DFG (Project 521147274) to U.W.

Institutional Review Board Statement: Not applicable.

Informed Consent Statement: Not applicable.

Data Availability Statement: All raw data are available through contacting the corresponding author. Python code and AlphaFold2-multimer predictions used in this study are available via GitHub (https://github.com/LabWolfrum/Fritze_et_al.2023.git).

Acknowledgments: We thank Ronald Roepman (Human Genetics, Nijmegen), Robin Shaw (Cardiovascular Res. Inst., California), and Nasrin Sorusch (iDN, JGU) for the contribution of several plasmids and constructs used in this study. We thank Christof Rickert (LMCF, JGU) for his technical support. Support by the IMB Microscopy Core Facility is also gratefully acknowledged. We thank Lukas Stelzl (CMT, JGU) and Marcel Conrady (imP, JGU) for their valuable discussion about this manuscript. J.S.F. was enrolled in the International PhD Programme (IPP) Mainz.

Conflicts of Interest: The authors declare that this research was conducted in the absence of any commercial or financial relationships that could be construed as potential conflict of interest.

References

1. Papasaikas, P.; Tejedor, J.R.; Vigevani, L.; Valcárcel, J. Functional Splicing Network Reveals Extensive Regulatory Potential of the Core Spliceosomal Machinery. *Mol. Cell* **2015**, *57*, 7–22. [CrossRef] [PubMed]
2. Will, C.L.; Lührmann, R. Spliceosome Structure and Function. *Cold Spring Harb. Perspect. Biol.* **2011**, *3*, a003707. [CrossRef] [PubMed]
3. Yildirim, A.; Mozaffari-Jovin, S.; Wallisch, A.K.; Schäfer, J.; Ludwig, S.E.J.; Urlaub, H.; Lührmann, R.; Wolfrum, U. SANS (USH1G) Regulates Pre-MRNA Splicing by Mediating the Intra-Nuclear Transfer of Tri-SnRNP Complexes. *Nucleic Acids Res.* **2021**, *49*, 5845–5866. [CrossRef]
4. Matera, A.G.; Wang, Z. A Day in the Life of the Spliceosome. *Nat. Rev. Mol. Cell Biol.* **2014**, *15*, 108–121. [CrossRef]
5. Fuster-Garcia, C.; Garcia-Bohorquez, B.; Rodriguez-Munoz, A.; Aller, E.; Jaijo, T.; Millan, J.M.; Garcia-Garcia, G. Usher Syndrome: Genetics of a Human Ciliopathy. *Int. J. Mol. Sci.* **2021**, *22*, 6723. [CrossRef]
6. Velde, H.M.; Reurink, J.; Held, S.; Li, C.H.Z.; Yzer, S.; Oostrik, J.; Weeda, J.; Haer-Wigman, L.; Yntema, H.G.; Roosing, S.; et al. Usher Syndrome Type IV: Clinically and Molecularly Confirmed by Novel ARSG Variants. *Hum. Genet.* **2022**, *141*, 1723–1738. [CrossRef] [PubMed]
7. Peter, V.G.; Quinodoz, M.; Sadio, S.; Held, S.; Rodrigues, M.; Soares, M.; Sousa, A.B.; Coutinho Santos, L.; Damme, M.; Rivolta, C. New Clinical and Molecular Evidence Linking Mutations in ARSG to Usher Syndrome Type IV. *Hum. Mutat.* **2021**, *42*, 261–271. [CrossRef]
8. Weil, D.; El-Amraoui, A.; Masmoudi, S.; Mustapha, M.; Kikkawa, Y.; Laine, S.; Delmaghani, S.; Adato, A.; Nadifi, S.; Ben Zina, Z.; et al. Usher Syndrome Type I G (USH1G) Is Caused by Mutations in the Gene Encoding SANS, a Protein That Associates with the USH1C Protein, Harmonin. *Hum. Mol. Genet.* **2003**, *12*, 463–471. [CrossRef]
9. Sorusch, N.; Baub, K.; Plutniok, J.; Samanta, A.; Knapp, B.; Nagel-Wolfrum, K.; Wolfrum, U. Characterization of the Ternary Usher Syndrome SANS/Ush2a/Whirlin Protein Complex. *Hum. Mol. Genet.* **2017**, *26*, 1157–1172. [CrossRef]
10. Caberlotto, E.; Michel, V.; Foucher, I.; Bahloul, A.; Goodyear, R.J.; Pepermans, E.; Michalski, N.; Perfettini, I.; Alegria-Prévot, O.; Chardenoux, S.; et al. Usher Type 1G Protein sans Is a Critical Component of the Tip-Link Complex, a Structure Controlling Actin Polymerization in Stereocilia. *Proc. Natl. Acad. Sci. USA* **2011**, *108*, 5825–5830. [CrossRef]
11. He, Y.; Li, J.; Zhang, M. Myosin VII, USH1C, and ANKS4B or USH1G Together Form Condensed Molecular Assembly via Liquid-Liquid Phase Separation. *Cell Rep.* **2019**, *29*, 974–986.e4. [CrossRef] [PubMed]
12. Géléoc, G.G.S.; El-Amraoui, A. Disease Mechanisms and Gene Therapy for Usher Syndrome. *Hear. Res.* **2020**, *394*, 107932. [CrossRef] [PubMed]
13. Maerker, T.; van Wijk, E.; Overlack, N.; Kersten, F.F.J.; Mcgee, J.; Goldmann, T.; Sehn, E.; Roepman, R.; Walsh, E.J.; Kremer, H.; et al. A Novel Usher Protein Network at the Periciliary Reloading Point between Molecular Transport Machineries in Vertebrate Photoreceptor Cells. *Hum. Mol. Genet.* **2008**, *17*, 71–86. [CrossRef] [PubMed]
14. Overlack, N.; Kilic, D.; Bauss, K.; Marker, T.; Kremer, H.; van Wijk, E.; Wolfrum, U.; Bauß, K.; Märker, T.; Kremer, H.; et al. Direct Interaction of the Usher Syndrome 1G Protein SANS and Myomegalin in the Retina. *Biochim. Biophys. Acta* **2011**, *1813*, 1883–1892. [CrossRef] [PubMed]
15. Bauss, K.; Knapp, B.; Jores, P.; Roepman, R.; Kremer, H.; Wijk, E.V.; Marker, T.; Wolfrum, U. Phosphorylation of the Usher Syndrome 1G Protein SANS Controls Magi2-Mediated Endocytosis. *Hum. Mol. Genet.* **2014**, *23*, 3923–3942. [CrossRef] [PubMed]
16. Papal, S.; Cortese, M.; Legendre, K.; Sorusch, N.; Dragavon, J.; Sahly, I.; Shorte, S.; Wolfrum, U.; Petit, C.; El-Amraoui, A. The Giant Spectrin βV Couples the Molecular Motors to Phototransduction and Usher Syndrome Type I Proteins along Their Trafficking Route. *Hum. Mol. Genet.* **2013**, *22*, 3773–3788. [CrossRef] [PubMed]
17. Sorusch, N.; Yildirim, A.; Knapp, B.; Janson, J.; Fleck, W.; Scharf, C.; Wolfrum, U. SANS (USH1G) Molecularly Links the Human Usher Syndrome Protein Network to the Intraflagellar Transport Module by Direct Binding to IFT-B Proteins. *Front. Cell Dev. Biol.* **2019**, *7*, 216. [CrossRef]
18. Sahly, I.; Dufour, E.; Schietroma, C.; Michel, V.; Bahloul, A.; Perfettini, I.; Pepermans, E.; Estivalet, A.; Carette, D.; Aghaie, A.; et al. Localization of Usher 1 Proteins to the Photoreceptor Calyceal Processes, Which Are Absent from Mice. *J. Cell Biol.* **2012**, *199*, 381–399. [CrossRef]
19. Cowan, C.S.; Renner, M.; De Gennaro, M.; Gross-Scherf, B.; Goldblum, D.; Hou, Y.; Munz, M.; Rodrigues, T.M.; Krol, J.; Szikra, T.; et al. Cell Types of the Human Retina and Its Organoids at Single-Cell Resolution. *Cell* **2020**, *182*, 1623–1640.e34. [CrossRef] [PubMed]
20. Adato, A.; Michel, V.; Kikkawa, Y.; Reiners, J.; Alagramam, K.N.; Weil, D.; Yonekawa, H.; Wolfrum, U.; El-Amraoui, A.; Petit, C. Interactions in the Network of Usher Syndrome Type 1 Proteins. *Hum. Mol. Genet.* **2005**, *14*, 347–356. [CrossRef] [PubMed]
21. Sorusch, N.; Wunderlich, K.; Bauá, K.; Nagel-Wolfrum, K.; Wolfrum, U. Usher Syndrome Protein Network Functions in the Retina and Their Relation to Other Retinal Ciliopathies. In *Retinal Degenerative Diseases*; Ash, J., Grimm, C., Hollyfield, J., Anderson, R., LaVail, M., Bowes Rickman, C., Eds.; Advances in Experimental Medicine and Biology; Springer: New York, NY, USA, 2014. [CrossRef]
22. Overlack, N.; Maerker, T.; Latz, M.; Nagel-Wolfrum, K.; Wolfrum, U. SANS (USH1G) Expression in Developing and Mature Mammalian Retina. *Vis. Res.* **2008**, *48*, 400–412. [CrossRef]
23. Evans, R.; O'neill, M.; Pritzel, A.; Antropova, N.; Senior, A.; Green, T.; Žídek, A.; Bates, R.; Blackwell, S.; Yim, J.; et al. Protein Complex Prediction with AlphaFold-Multimer. *bioRxiv* **2021**, preprint. [CrossRef]

24. Emenecker, R.J.; Griffith, D.; Holehouse, A.S. Metapredict: A Fast, Accurate, and Easy-to-Use Predictor of Consensus Disorder and Structure. *Biophys. J.* **2021**, *120*, 4312–4319. [CrossRef] [PubMed]
25. Karpova, T.S.; Baumann, C.T.; He, L.; Wu, X.; Grammer, A.; Lipsky, P.; Hager, G.L.; McNally, J.G. Fluorescence Resonance Energy Transfer from Cyan to Yellow Fluorescent Protein Detected by Acceptor Photobleaching Using Confocal Microscopy and a Single Laser. *J. Microsc.* **2003**, *209*, 56–70. [CrossRef] [PubMed]
26. Yan, J.; Pan, L.; Chen, X.; Wu, L.; Zhang, M. The Structure of the Harmonin/sans Complex Reveals an Unexpected Interaction Mode of the Two Usher Syndrome Proteins. *Proc. Natl. Acad. Sci. USA* **2010**, *107*, 4040–4045. [CrossRef] [PubMed]
27. Liu, S.; Li, P.; Dybkov, O.; Nottrott, S.; Hartmuth, K.; Lührmann, R.; Carlomagno, T.; Wahl, M.C. Binding of the Human Prp31 Nop Domain to a Composite RNA-Protein Platform in U4 SnRNP. *Science* **2007**, *316*, 115–120. [CrossRef] [PubMed]
28. Charenton, C.; Wilkinson, M.E.; Nagai, K. Mechanism of 5′ Splice Site Transfer for Human Spliceosome Activation. *Science* **2019**, *364*, 362–367. [CrossRef]
29. Colcombet-Cazenave, B.; Druart, K.; Bonnet, C.; Petit, C.; Sperandio, O.; Guglielmini, J.; Wolff, N. Phylogenetic Analysis of Harmonin Homology Domains. *BMC Bioinform.* **2021**, *22*, 190. [CrossRef]
30. Jumper, J.; Evans, R.; Pritzel, A.; Green, T.; Figurnov, M.; Ronneberger, O.; Tunyasuvunakool, K.; Bates, R.; Žídek, A.; Potapenko, A.; et al. Highly accurate protein structure prediction with AlphaFold. *Nature* **2021**, *596*, 583–589. [CrossRef]
31. Alderson, T.R.; Pritišanac, I.; Kolarić, E.; Moses, A.M.; Forman-Kay, J.D. Systematic Identification of Conditionally Folded Intrinsically Disordered Regions by AlphaFold2. *bioRxiv* **2023**, preprint. [CrossRef]
32. Nguyen Ba, A.N.; Yeh, B.J.; Van Dyk, D.; Davidson, A.R.; Andrews, B.J.; Weiss, E.L.; Moses, A.M. Proteome-Wide Discovery of Evolutionary Conserved Sequences in Disordered Regions. *Sci. Signal.* **2012**, *5*, rs1. [CrossRef] [PubMed]
33. Holehouse, A.S.; Das, R.K.; Ahad, J.N.; Richardson, M.O.G.; Pappu, R.V. CIDER: Resources to Analyze Sequence-Ensemble Relationships of Intrinsically Disordered Proteins. *Biophys. J.* **2017**, *112*, 16–21. [CrossRef] [PubMed]
34. Das, R.K.; Ruff, K.M.; Pappu, R.V. Relating Sequence Encoded Information to Form and Function of Intrinsically Disordered Proteins. *Curr. Opin. Struct. Biol.* **2015**, *32*, 102–112. [CrossRef]
35. Sheinerman, F.B.; Norel, R.; Honig, B. Electrostatic Aspects of Protein-Protein Interactions. *Curr. Opin. Struct. Biol.* **2000**, *10*, 153–159. [CrossRef] [PubMed]
36. Hevekerl, H.; Spielmann, T.; Chmyrov, A.; Widengren, J. Förster Resonance Energy Transfer beyond 10 Nm: Exploiting the Triplet State Kinetics of Organic Fluorophores. *J. Phys. Chem.* **2011**, *115*, 13360–13370. [CrossRef] [PubMed]
37. Roszik, J.; Tóth, G.; Szöllosi, J.; Vereb, G. Validating Pharmacological Disruption of Protein-Protein Interactions by Acceptor Photobleaching FRET Imaging. In *Target Identification and Validation in Drug Discovery*; Moll, J., Colombo, R., Eds.; Methods in Molecular Biology; Humana Press: Totowa, NJ, USA, 2013; Volume 986, pp. 165–178. [CrossRef]
38. Tancredi, T.; Carrà, G.; Guerrini, R.; Arduin, M.; Calò, G.; Regoli, D.; Salvadori, S.; Temussi, P.A. The Interaction of Highly Helical Structural Mutants with the NOP Receptor Discloses the Role of the Address Domain of Nociceptin/Orphanin FQ. *Chem. Eur. J.* **2005**, *11*, 2061–2070. [CrossRef] [PubMed]
39. Ghram, M.; Morris, G.; Culjkovic-Kraljacic, B.; Mars, J.; Gendron, P.; Skrabanek, L.; Revuelta, M.V.; Cerchietti, L.; Guzman, M.L.; Borden, K.L.B. The Eukaryotic Translation Initiation Factor EIF4E Reprograms Alternative Splicing. *EMBO J.* **2023**, *42*, e110496. [CrossRef]
40. Bertram, K.; Agafonov, D.E.; Dybkov, O.; Haselbach, D.; Leelaram, M.N.; Will, C.L.; Urlaub, H.; Kastner, B.; Lührmann, R.; Stark, H. Cryo-EM Structure of a Pre-Catalytic Human Spliceosome Primed for Activation. *Cell* **2017**, *170*, 701–713.e11. [CrossRef]
41. Novotny, I.; Blazikova, M.; Stanek, D.; Herman, P.; Malinsky, J. In Vivo Kinetics of U4/U6 U5 Tri-SnRNP Formation in Cajal Bodies. *Mol. Biol. Cell* **2011**, *22*, 513–523. [CrossRef]
42. Stanek, D.; Pridalova-Hnilicova, J.; Novotny, I.; Huranova, M.; Blazikova, M.; Wen, X.; Sapra, A.K.; Neugebauer, K.M. Spliceosomal Small Nuclear Ribonucleoprotein Particles Repeatedly Cycle through Cajal Bodies. *Mol. Biol. Cell* **2008**, *19*, 2534–2543. [CrossRef]
43. Fokkema, I.F.A.C.; Taschner, P.E.M.; Schaafsma, G.C.P.; Celli, J.; Laros, J.F.J.; den Dunnen, J.T. LOVD v.2.0: The next Generation in Gene Variant Databases. *Hum. Mutat.* **2011**, *32*, 557–563. [CrossRef]
44. Nagel-Wolfrum, K.; Fadl, B.R.; Becker, M.M.; Wunderlich, K.A.; Schäfer, J.; Sturm, D.; Fritze, J.; Gür, B.; Kaplan, L.; Andreani, T.; et al. Expression and Subcellular Localization of USH1C/Harmonin in Human Retina Provides Insights into Pathomechanisms and Therapy. *Hum. Mol. Genet.* **2023**, *32*, 431–449. [CrossRef] [PubMed]
45. Islam, Z.; Nagampalli, R.S.K.; Fatima, M.T.; Ashraf, G.M. New Paradigm in Ankyrin Repeats: Beyond Protein-Protein Interaction Module. *Int. J. Biol. Macromol.* **2018**, *109*, 1164–1173. [CrossRef] [PubMed]
46. Tanackovic, G.; Ransijn, A.; Ayuso, C.; Harper, S.; Berson, E.L.; Rivolta, C. A Missense Mutation in PRPF6 Causes Impairment of Pre-MRNA Splicing and Autosomal-Dominant Retinitis Pigmentosa. *Am. J. Hum. Genet.* **2011**, *88*, 643–649. [CrossRef]
47. Buskin, A.; Zhu, L.; Chichagova, V.; Basu, B.; Mozaffari-Jovin, S.; Dolan, D.; Droop, A.; Collin, J.; Bronstein, R.; Mehrotra, S.; et al. Disrupted Alternative Splicing for Genes Implicated in Splicing and Ciliogenesis Causes PRPF31 Retinitis Pigmentosa. *Nat. Commun.* **2018**, *9*, 4234. [CrossRef] [PubMed]
48. Stenson, P.D.; Ball, E.V.; Mort, M.; Phillips, A.D.; Shiel, J.A.; Thomas, N.S.T.; Abeysinghe, S.; Krawczak, M.; Cooper, D.N. Human Gene Mutation Database (HGMD®): 2003 Update. *Hum. Mutat.* **2003**, *21*, 577–581. [CrossRef] [PubMed]
49. Zelinger, L.; Swaroop, A. RNA Biology in Retinal Development and Disease. *Trends Genet.* **2018**, *34*, 341–351. [CrossRef] [PubMed]

50. Aisa-Marin, I.; Garcia-Arroyo, R.; Mirra, S.; Marfany, G. The Alter Retina: Alternative Splicing of Retinal Genes in Health and Disease. *Int. J. Mol. Sci.* **2021**, *22*, 1855. [CrossRef]
51. Murphy, D.; Cieply, B.; Carstens, R.; Ramamurthy, V.; Stoilov, P. The Musashi 1 Controls the Splicing of Photoreceptor-Specific Exons in the Vertebrate Retina. *PLoS Genet.* **2016**, *12*, e1006256. [CrossRef]
52. Sundar, J.; Matalkah, F.; Jeong, B.; Stoilov, P.; Ramamurthy, V. The Musashi Proteins MSI1 and MSI2 Are Required for Photoreceptor Morphogenesis and Vision in Mice. *J. Biol. Chem.* **2020**, *296*, 100048. [CrossRef]
53. Schindelin, J.; Rueden, C.T.; Hiner, M.C.; Eliceiri, K.W. The ImageJ Ecosystem: An Open Platform for Biomedical Image Analysis. *Mol. Reprod. Dev.* **2015**, *82*, 518–529. [CrossRef] [PubMed]
54. Mirdita, M.; Schütze, K.; Moriwaki, Y.; Heo, L.; Ovchinnikov, S.; Steinegger, M. ColabFold: Making Protein Folding Accessible to All. *Nat. Methods* **2022**, *19*, 679–682. [CrossRef] [PubMed]
55. Pettersen, E.F.; Goddard, T.D.; Huang, C.C.; Couch, G.S.; Greenblatt, D.M.; Meng, E.C.; Ferrin, T.E. UCSF Chimera—A Visualization System for Exploratory Research and Analysis. *J. Comput. Chem.* **2004**, *25*, 1605–1612. [CrossRef] [PubMed]
56. Nunez-Castilla, J.; Siltberg-Liberles, J. An Easy Protocol for Evolutionary Analysis of Intrinsically Disordered Proteins. In *Intrinsically Disordered Proteins*; Kragelund, B.B., Skriver, K., Eds.; Methods in Molecular Biology; Humana Press Inc.: Totowa, NJ, USA, 2020; Volume 2141, pp. 147–177.
57. Waterhouse, A.M.; Procter, J.B.; Martin, D.M.A.; Clamp, M.; Barton, G.J. Jalview Version 2-A Multiple Sequence Alignment Editor and Analysis Workbench. *Bioinformatics* **2009**, *25*, 1189–1191. [CrossRef]
58. Positteam Download RStudio—Posit. Available online: https://posit.co/downloads/ (accessed on 24 July 2023).

6.2 Publication 2: Nuclear-cytoplasmic shuttling of the Usher syndrome 1G protein SANS differs from its paralogue ANKS4B (Fritze et al., 2024)

cells

MDPI

Article

Nuclear–Cytoplasmic Shuttling of the Usher Syndrome 1G Protein SANS Differs from Its Paralog ANKS4B

Jacques S. Fritze, Felizitas F. Stiehler and Uwe Wolfrum *

Institute of Molecular Physiology, Johannes Gutenberg University Mainz, 55128 Mainz, Germany; jfritze@uni-mainz.de (J.S.F.); f.stiehler@imb-mainz.de (F.F.S.)
* Correspondence: wolfrum@uni-mainz.de; Tel.: +49-(0)-6131-39-25148

Abstract: The *USH1G* protein SANS is a small multifunctional scaffold protein. It is involved in several different cellular processes, such as intracellular transport, in the cytoplasm, or splicing of pre-mRNA, in the cell nucleus. Here, we aimed to gain insight into the regulation of the subcellular localization and the nuclear–cytoplasmic shuttling of SANS and its paralog ANKS4B, not yet reported in the nucleus. We identified karyopherins mediating the nuclear import and export by screening the nuclear interactome of SANS. Sequence analyses predicted in silico evolutionarily conserved nuclear localization sequences (NLSs) and nuclear export sequences (NESs) in SANS, but only NESs in ANKS4B, which are suitable for karyopherin binding. Quantifying the nuclear–cytoplasmic localization of wild-type SANS and NLS/NES mutants, we experimentally confirmed in silico predicted NLS and NES functioning in the nuclear–cytoplasmic shuttling in situ in cells. The comparison of SANS and its paralog ANKS4B revealed substantial differences in the interaction with the nuclear splicing protein PRPF31 and in their nuclear localization. Finally, our results on pathogenic USH1G/SANS mutants suggest that the loss of NLSs and NESs and thereby the ability to control nuclear–cytoplasmic shuttling is disease-relevant.

Keywords: Usher syndrome; USH1G; SANS; ANKS4B; karyopherin; nuclear–cytoplasmic shuttling

Citation: Fritze, J.S.; Stiehler, F.F.; Wolfrum, U. Nuclear–Cytoplasmic Shuttling of the Usher Syndrome 1G Protein SANS Differs from Its Paralog ANKS4B. *Cells* **2024**, *13*, 1855. https://doi.org/10.3390/cells13221855

Academic Editor: Manfred Alsheimer

Received: 14 October 2024
Revised: 4 November 2024
Accepted: 6 November 2024
Published: 8 November 2024

1. Introduction

SANS (scaffold protein containing ankyrin repeats and SAM domain) is encoded by the *USH1G* gene [1]. Pathogenic variants of *USH1G* lead to the human Usher syndrome (USH), the most common form of combined hereditary deaf-blindness in humans [2,3]. SANS is a small 52 kDa protein that consists of 461 amino acids. It is composed of three N-terminal ankyrin repeats (ANK1-3), a central domain (CENT), a sterile alpha motif (SAM), and a PDZ-binding motif at the C-terminal end (Figure 1A) [1]. Based on its different functional properties the CENT can be further divided into three subdomains, CENTn1, CENTn2, and CENTc [4]. Context-dependent binding of numerous proteins to its different domains characterizes SANS as a potent scaffold protein [5–12]. In auditory hair cells, SANS plays a crucial role in arranging the four other USH type-1 proteins in the mechanosensitive tip-link complex of the stereocilia [13].

In photoreceptor cells of the retina, SANS functions have been associated with ciliogenesis and the intracellular transport of cargoes to their photosensitive outer segment [6–11]. In addition to these cytoplasm-associated processes, SANS has also been found in the nucleus [7,12,14]. In the nucleus, SANS has been recently linked to the control of pre-mRNA splicing and the activation of the spliceosome by interacting with several spliceosomal components [4,12]. However, the question of how the distribution of SANS between the two cellular compartments the cytoplasm and the nucleus is regulated in the cell remained open.

Interestingly, SANS has a paralog protein in ANKS4B (ankyrin repeat and SAM domain-containing protein 4B) [14]. Both scaffold proteins are composed of the same principal domain structure (Figure 1A); possess high, up to 80%, amino acid sequence homology;

and share common binding partners, such as the USH1C protein harmonin [5,14–16]. ANKS4B and SANS are both located at the tips of microvilli, the brush border microvilli of intestinal enterocytes and the stereocilia, highly modified microvilli of inner ear hair cells, respectively [13,17]. However, while both are found in the cytoplasm, ANKS4B has not yet been reported in the nucleus [14,18]. Moreover, the mechanisms underlying this difference in nuclear–cytoplasmic partitioning have yet to be determined and are one of the questions we address here.

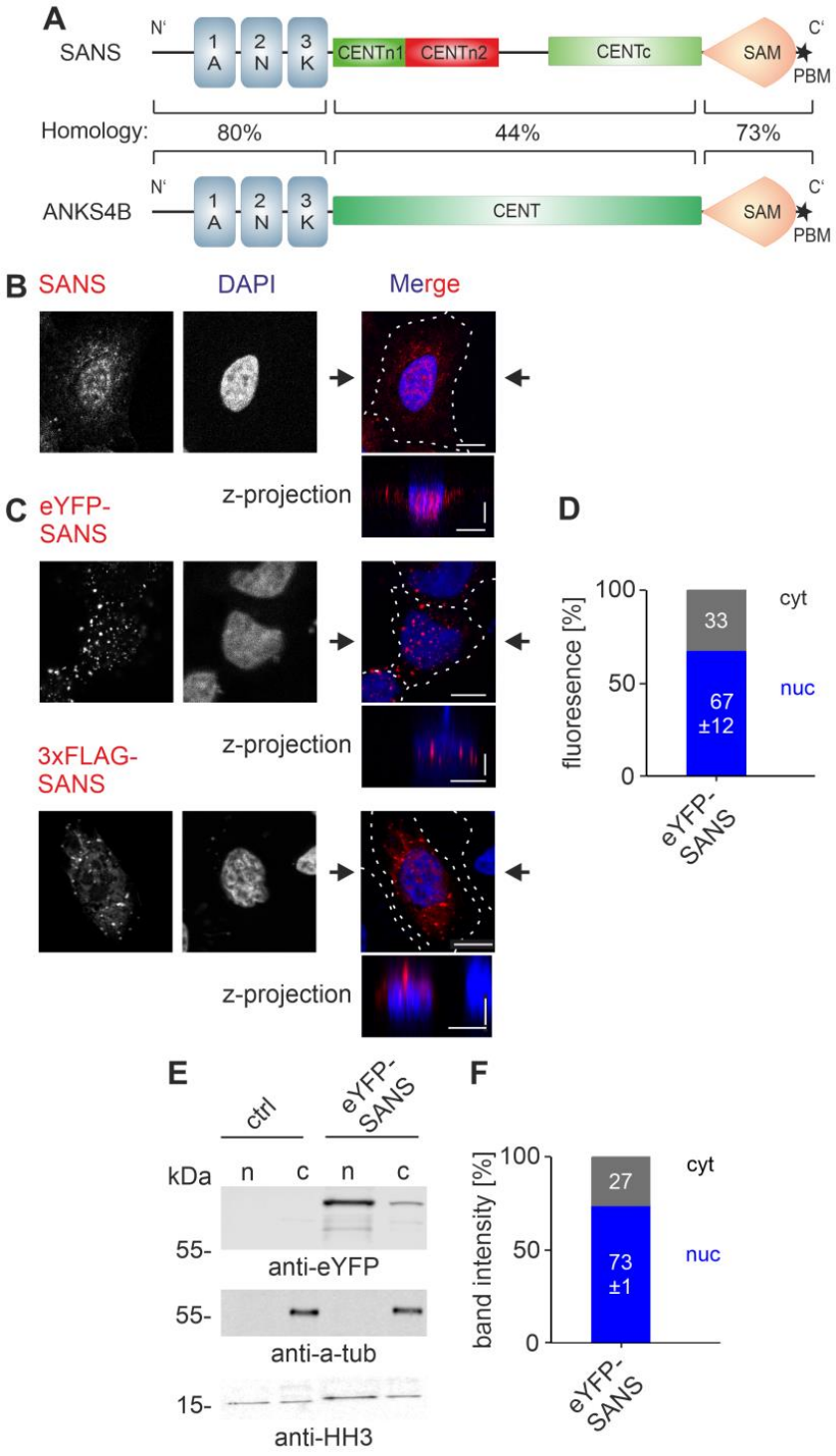

Figure 1. Nuclear localization of SANS. (**A**) Domain structure of SANS and its paralog ANKS4B: Both consist of three ankyrin repeats (ANK1-3), a central domain (CENT), divided in SANS into three

parts (CENTn1 (green), CENTn2 (red), and CENTc (green)), a sterile alpha motif (SAM), and a C-terminal type-I PDZ-binding motif (PBM =asterisk). ANKS4B and SANS amino acid sequences are highly similar in their N- and C-terminal regions. (**B**,**C**) Confocal microscopy of HeLa cells either stained for endogenous SANS (**B**) or transfected with eYFP-SANS, 3xFLAG-SANS (**C**), counterstained with DAPI. Endogenous SANS and 3xFLAG-SANS were visualized by indirect immunofluorescence of anti-SANS and anti-FLAG. (**B**,**C**) Endogenous SANS, eYFP-SANS, and 3xFLAG-SANS were localized in the cytoplasm and the nucleus. (**D**) Quantification of eYFP-SANS localization by CellProfiler v4.2.6 in HeLa cells. eYFP-SANS is localized in both the nucleus and cytoplasm. (**E**) Western blot analysis of eYFP SANS in the nuclear (n) and cytoplasmic (c) fraction of eYFP-SANS-transfected HeLa cells using anti-eYFP, anti-tubulin (cytoplasmic housekeeping protein), and anti-HH3 (nuclear housekeeping protein). In each lane, 30 µg of the total protein was loaded. (**F**) Quantification of the eYFP-SANS bands in the nuclear (n) and cytoplasmic fraction (c). Band intensity was normalized to the total protein amount. The qualifications of the microscopic and biochemical analysis consistently demonstrate that the majority of eYFP-SANS (~70%) is localized in the nucleus. Black arrows: position of Z-projections. Scale bars: horizontal = 10 µm; vertical = 2 µm. Data show mean values ± standard deviation from three independent experiments.

Nuclear transport is a fundamental cellular process that regulates the localization of macromolecules within the nuclear or cytoplasmic compartments. In humans, approximately 60 proteins participate in nuclear transport, including Ran system proteins that ensure directed and rapid transport, components that form nuclear pore complexes (NPCs) in the nuclear membrane, and karyopherins that transport cargoes through the NPCs [19]. For bidirectional shuttling of nuclear cargo proteins, karyopherins, namely importins and exportins, are needed [20]. These bind specifically to linear elements in the nuclear cargos, which are called nuclear localization sequences (NLSs) and nuclear export sequences (NESs), respectively.

In the present study, we aimed to shed light on the nuclear–cytoplasmic shuttling of SANS and its paralog ANKS4B. We screened the SANS interactome to identify importins and exportins and used in silico prediction tools to find conserved NLSs and NESs in SANS protein sequences of several vertebrates. We validated the nuclear–cytoplasmic shuttling potential of wild-type and mutated NLS/NES versions of SANS in HeLa and HEK293T cells by quantifying the nuclear–cytoplasmic localization, which confirmed predicted NLSs and NESs to be important for correct nuclear–cytoplasmic shuttling of SANS. In contrast, strict localization of the SANS paralog ANKS4B in the cytoplasm is ensured in the absence of any NLS by several NESs. Finally, we provide evidence that the dysregulation and disruption of SANS's nuclear–cytoplasmic shuttling are relevant for the development of the USH disease in USH1G patients.

2. Materials and Methods

2.1. DNA Constructs and Antibodies

DNA Constructs (Table 1), PCR Primers (Table 2) and Antibodies (Table 3) shown below.

Table 1. DNA constructs. Asterisk indicates that the mutations.

DNA Constructs	Reference
eYFP-SANS-S243*	this work
eYFP-SANS-K213E	this work
eYFP-SANS-R447W	this work
eYFP-SANS-L195E	this work
eYFP-SANS-L249E	this work
eYFP-ANKS4B	this work
harmonin-mCherry	this work

Table 1. *Cont.*

DNA Constructs	Reference
eYFP-SANS	[4]
eYFP-SANS-S278Pfs*71	[4]
eYFP-SANS-V132Gfs*3	[4]
eCFP-PRPF31	[4]
harmonin-eCFP	[4]
eCFP-c-eYFP (FRET positive control)	[4]
mRFP-PRPF31	[4]
FLAG-SANS	[12]
pDONR-SANS	[10]
pDONR-SANS-S243*	[10]
pDest-743 (eYFP control)	kindly provided by Ronald Roepman
pDONR-ANKS4B	kindly provided by Katja Luck [21]

Table 2. PCR Primers.

Primer Name	Sequence 5′-3′
K213E_fwd	GGCGAGACCAAGATGCAG
K231E_rev	CCTGGCCGTGCCGTG
R447W_fwd	CGGTGGCAGGCGATG
R447W_rev	CCTCCTCACGGCCC
L195E_fwd	GCGGAGGGCAGCC
L195E_rev	CAGATGCTGCAGCCGG
L249E_fwd	CAGGAGGGCAGCGAC
L249E_rev	CAGGCCCGAGAGCG
qPCR PRPF31 F	CAGACACAGGTAAACGAGGC
qPCR PRPF31 R	CTGGAGTGGGGTGAAGGC

Table 3. Antibodies.

Antibody Name	Supplier	Catalog No.
Rabbit-anti-SANS	Proteintech, Planegg-Martinsried, Germany	21936-1-AP
Rabbit-anti-histonH3	Cell Signaling Technology, Danvers, MA, USA	4499
Mouse-anti-α-tubulin	Merck, Darmstadt, Germany	T9026
Mouse-anti-FLAG	Merck, Darmstadt, Germany	F1804
Mouse-anti-GFP (cross-reaction to eYFP)	Proteintech, Planegg-Martinsried, Germany	66002-1-Ig
Rat-anti-RFP	Proteintech, Planegg-Martinsried, Germany	5f8
Rabbit-anti-γ-tubulin	Merck, Darmstadt, Germany	T6557
Donkey-anti-rabbit Alexa488	ThermoFisher, Darmstadt, Germany	A-21206
Donkey-anti-rabbit Alexa680	ThermoFisher, Darmstadt, Germany	A-10043
Donkey-anti-mouse Alexa800	ThermoFisher, Darmstadt, Germany	SA5-10172
Donkey-anti-rat Alexa680	ThermoFisher, Darmstadt, Germany	A-78947

2.2. Cloning

NLS/NES mutants were created by Q5® Site-Directed Mutagenesis Kit according to the manufacturer's protocol (NEB, Frankfurt am Main, Germany, #E0554S) with pDONR-SANS as a template. pDONR-ANKS4B was kindly provided by Katja Luck [21]. Gateway™ LR reaction into the appropriate destination vector was performed according to the manufacturer's protocol (ThermoFisher, Darmstadt, Germany, #11791020).

2.3. Cell Lines and Culture

Dulbecco's modified Eagle's medium (DMEM) (ThermoFisher, Darmstadt, Germany, #31966021) containing 10% heat-inactivated fetal calf serum (FCS) (Cytiva, Freiburg, Germany, #SV30160.03) was used to culture HeLa (kindly provided by AG Dormann, IMP, Mainz, Germany) and HEK293T cells (ATCC: CRL-3216).

2.4. Cell Transfections

HeLa cells and HEK293T cells were seeded on coverslips in 6-well plates with a density of 250,000 cells/well. Cells were transfected with tagged constructs using Lipofectamine™ LTX as described by the manufacturer (ThermoFisher, Darmstadt, Germany, #15338100) and incubated for 24 h. Protein expression levels of the constructs were compared in Western blots (Figure S1). CRM1 cells were treated with 5 nM Leptomycin-B (Selleck Chemicals GmbH, Munich, Germany, #S7580) for the inhibition of the exportin or 40 µM Importazole (Merck, Darmstadt, Germany, #401105) for the inhibition of importins for 4 h before fixation.

2.5. siRNA-Mediated Knockdown

For siRNA-mediated knockdowns, we used siRNA for PRPF31 (IDT, Leuven, Belgien, #TriFECTa®Kit DsiRNA Duplex, 5′-AGCUAUGGGAUAGUAAGAUGUUUGC-3′) with previously validated knockdown efficiency by qPCR [12]. The siRNA was co-transfected with eYFP-SANS into HeLa cells using Lipofectamine™ RNAiMAX and incubated for 24 h as described by the manufacturer (ThermoFisher, Darmstadt, Germany, #13778075). The siRNA transfection was subsequently detected by qPCR.

2.6. Live Cell Imaging and Fluorescence Recovery After Photobleaching (FRAP)

HeLa cells were seeded in an Ibidi 4-well plate (Ibidi, Gräfelfing, Germany #80426) with a density of 40,000 cells/well. Cells were transfected with the fluorescently tagged constructs using Lipofectamine™ LTX. Living cells were analyzed with a Nikon Yokogawa spinning disc microscope with a 60× water objective at 37 °C and imaged every second. FRAP was performed with a 514 nm laser at 36% laser intensity for 100 iterations. Recovery was observed every second for up to 4 min. Quantification was performed with Fiji and EasyFRAP-web [22]. Data are presented as Full-Scale Normalization, and T-half was calculated with Double curve fitting.

2.7. Immunocytochemistry

Cells were fixed with 4% paraformaldehyde in PBS for 10 min at RT, washed with PBS, permeabilized with PBST (0.1% Triton-X100 (Roth, Karlsruhe, Germany, # 3051.1)) for 5 min at RT, and blocked with 0.1% ovalbumin and 0.5% fish gelatine in PBS for 1 h at RT. Primary antibodies were incubated overnight at 4 °C, followed by washing with PBS and secondary antibody in a blocking solution containing DAPI (1 mg/mL) (Roth, Karlsruhe, #6335.1) with incubation for 1 h at RT. After washing, samples were mounted in Mowiol (Roth, Karlsruhe, #0713.2).

2.8. Cytochemical Staining of Aggresomes

HeLa cells were transfected with eYFP-SANS and NLS/NES mutants with Lipofectamine™ LTX as described by the manufacturer (ThermoFisher, Darmstadt, Germany, #15338100). Control cells were treated 18 h before fixation with DMSO as negative control or with the proteasomal inhibitor MG-132 (5 µM) in DMSO to induce the formation of aggresomes. Cells were fixed with 4% paraformaldehyde in PBS for 10 min at RT, washed with PBS, and permeabilized with PBST (0.1% Triton-X100 (Roth, Karlsruhe, # 3051.1)) 5 min at RT. Subsequently, cells were fluorescently stained for aggresomes with a commercial kit following the supplier's protocol (Enzo, Lausen, Germany, #ENZ-51035-K100).

2.9. Fluorescence Microscopy Analysis

Fixed cells were observed with a Leica TCS SP5 or Zeiss LSM900 (Leica, Wetzlar, Germany). Images were analyzed with Fiji [23] (https://imagej.net/software/fiji/downloads, accessed 1 April 2022). Z-projections were performed over the indicated region of interest with the Fiji Plugin Orthogonal Views. Pearson coefficient calculation was performed with the Fiji Plugin Coloc 2.

2.10. Western Blot Analysis

Cells were lysed in Triton-X-100 lysis buffer (50 mM Tris/HCl, 150 mM NaCl, 0.5% Triton-X-100, pH 7.4) containing complete protease inhibitor cocktail (Roche Diagnostics, Mannheim, Germany #04693132001) by sonication. Protein content was quantified using a BCA protein assay (Merck, Darmstadt, #B9643, #C2284) and subjected to SDS-PAGE. The proteins were transferred to a polyvinylidene difluoride (PVDF) membrane (Merck, Darmstadt, #IPVH00010). After blotting, membranes were blocked in AppliChem blocking reagent (AppliChem, Darmstadt, Germany) for 1 h and subsequently incubated with primary antibodies overnight at 4 °C followed by appropriate secondary antibodies. Blots were scanned employing the Odyssey infrared imaging system (LI-COR Biosciences, Lincoln, NE, USA).

2.11. In Silico Prediction

The amino acid sequence of the protein of interest was used from uniprot. The following sequences were used: *Homo sapiens* SANS (Q495M9); *Macaca nemestrina* SANS (A0A2K6BVI9); *Mus musculus* SANS (Q80T11); *Danio rerio* SANS (A0A8M1RQW2); *Xenopus laevis* SANS (A0A8J0TLE4); *H. sapiens* ANKS4B (Q8N8V4). NLSs were predicted with a given amino acid sequence by NLStradamus [24]. NESs were predicted with a given amino acid sequence by LocNES [25]. The homology of SANS NLS/NES was aligned with Blastp (https://blast.ncbi.nlm.nih.gov/Blast.cgi?PAGE =Proteins, accessed on 2 April 2024). The homology of SANS and ANKS4B was calculated from the alignment of Blastp (https://blast.ncbi.nlm.nih.gov/Blast.cgi?PAGE =Proteins, accessed on 1 March 2024).

Missense3D or Missense3D-PPI was used as a web-based version (http://missense3d.bc.ic.ac.uk/, accessed on 30 September 2024). For Missense3D, the AlphaFold2-based structure of SANS was used (AF-Q495M9-F1-v4). For Missense3D-PPI, the previously described structures of SANS-PRPF31 and SANS-harmonin were used [4]. The predicted SANS-harmonin is in line with the previously described complex structure [15].

2.12. CellProfiler-Based Nuclear/Cytoplasmic Ratio Quantification

Images were preanalyzed with Fiji and then analyzed automatically with CellProfiler [26]. For analysis, we used the pipeline "Human cells" (https://cellprofiler-examples.s3.amazonaws.com/ExampleHuman.zip, accessed on 1 January 2023) with adjustments available on Supplementary Materials (Github: https://github.com/LabWolfrum/Fritze_et_al_2024_SANS_Nuclear_localization).

In short, three tif files (protein of interest, DAPI, Brightfield) were used as input. Primary and secondary structures were identified with CellProfiler, and the mean intensity of the eYFP channel of the nucleus and cytoplasm was used for further statistical analysis.

2.13. Cell Fractionation Assay

Cells were seeded in 6-well plates with a density of 250,000 cells/well. Cells were transfected with Lipofectamine™ LTX as described by the manufacturer (ThermoFisher, Darmstadt, Germany, #15338100) and incubated for 24 h. Cells were harvested and lysed into nuclear and cytoplasmic fractions with the commercial kit NE-PER™ (ThermoFisher, Darmstadt, Germany, #78833). Protein amount was measured with a BCA assay, and proteins were eluted with 5x Laemmli buffer and separated by SDS-PAGE, followed by total protein measurement (Revert™ 700 Total Protein Staining) (LI-COR, Lincoln, NE, USA, #926-11010) and Western blotting. Relative intensity was calculated with Fiji for the GFP (cross-reaction for eYFP) band and normalized to total protein and the HistoneH3 band.

2.14. Fluorescence Resonance Energy Transfer (FRET) Acceptor Photobleaching Assay

HeLa cells were seeded in 6-well plates with a density of 250,000 cells/well. Cells were transfected with Lipofectamine™ LTX as described by the manufacturer (ThermoFisher, Darmstadt, Germany, #15338100). Fixed HeLa cells were analyzed with a

Leica TCS SP8, and FRET acceptor photobleaching was performed following the Leica protocol (https://downloads.leica-microsystems.com/TCS%20SP8/Application%20Note/FRET_AB_with%20SP8-AppLetter_EN.pdf, accessed 1 September 2022). eCFP was used as a donor (D), and eYFP as an acceptor (A). The acceptor was bleached at 100% laser intensity for 10 repeats. FRET efficiency was calculated via $FRET_{eff} = \left(\frac{(D_{post} - D_{pre})}{D_{post}}\right)$. To exclude the cellular structure, the mean of six regions of interest (ROIs) in the bleached area was calculated, and the FRET efficiency of an unbleached region ($\geq$3 µm away from bleached ROI) was subtracted from the mean. Bleach efficiency was calculated via the formula $Bleach_{eff} = \left(\frac{1-A\_post}{A\_pre}\right) \times 100$. Only ROIs with > 60% bleach efficiency were used for analysis. Data were normalized to 1 by the positive control eCFP-c-eYFP.

2.15. SANS Nuclear Interactome Analysis

SANS nuclear interactome analysis in HEK293T cells [12] was used as input for the Cytoscape plugin ClueGO according to gene names based on HGNC. Gene Ontology (GO) term enrichment analysis was performed by ClueGO v2.3.3.

2.16. Statistics

Statistical analysis was performed with R-Studio [27]. The statistical methods are listed in corresponding individual legends. Results are shown from at least 3 separate experiments. Significance was determined as follows: * $p \leq 0.05$, ** $p \leq 0.009$, *** $p \leq 0.0009$.

3. Results

3.1. Subcellular Localization of SANS

Recent work indicated that SANS shuttles from the cytoplasm into the nucleus [7,12,14]. We confirmed cytoplasmic and nuclear localization of endogenous SANS in HeLa cells by immunocytochemistry using anti-SANS antibodies (Figure 1B) and in HeLa cells transfected with eYFP-SANS and 3xFLAG-SANS monitoring eYFP fluorescence and indirect anti-FLAG immunofluorescence, respectively (Figure 1C). Confocal microscopy also showed that endogenous SANS and both transfected SANS constructs are not homogeneously distributed in the cytoplasm and the nucleus but appear as speckles of different sizes (Figure 1B,C). To verify the nature of these SANS speckles, we performed FRAP (fluorescence recovery after photobleaching) experiments, live cell imaging, and cytochemical staining for aggresomes in eYFP-SANS-expressing HeLa cells (Figures S2 and S3). FRAP analysis revealed that eYFP-SANS fluorescence recovered in a fast manner; after less than ~39 sec, almost 50% of its original intensity was recovered, indicating a high mobile fraction (Figure S2A). In live cell imaging experiments, we observed fission and fusion of eYFP-SANS speckles on the order of a few seconds (Figure S2B). Both the high mobile fraction in FRAP and the fission–fusion properties of eYFP-SANS speckles indicate liquid–liquid phase separation (LLPS) behavior [28].

In addition, we stained eYFP-SANS speckles for aggresomes by applying a cytochemical aggresome staining kit (Figure S3). We did not observe fluorescent aggresome staining of the eYFP-SANS speckles (Figure S3A), which contrasted with aggresome-positive controls (Figure S3B). Taken together, our analyses indicate that the eYFP-SANS speckles do not represent aggresomes, but rather are formed by LLPS, which is consistent with previous observations for Venus-SANS in HeLa cells [14].

In addition, we noticed a high variance in the subcellular localization of eYFP-SANS in the transfected HeLa cells. While in most cells, eYFP-SANS was mainly found in the nucleus (Figure 1C), there were also cells in which it was rather localized in the cytoplasm (Figure S4). Quantification of eYFP-SANS fluorescence in cytoplasmic and nuclear compartments of over 225 cells by CellProfiler revealed that approximately 30% of SANS was present in the cytoplasm and 70% in the nucleus in HeLa cells (Figure 1D). Quantitative analysis of the compartmental distribution in eYFP-SANS-expressing HEK293T cells confirmed that most SANS (77%) was localized in the nucleus (Figure S5A). Next, we

biochemically validated the compartmental distribution of SANS by cytoplasmic–nuclear cell fractionations in eYFP-SANS-transfected HeLa cells (Figure 1E,F). Western blot analysis of the nuclear and cytoplasmic fractions showed that approximately 70% of SANS was present in the nucleus, confirming the obtained in situ data.

Taken together our experimental data consistently demonstrated that SANS is predominantly localized in the nucleus.

3.2. Identification of Karyopherins in the Nuclear Interactome of SANS

To identify potential karyopherins that bind to SANS, we screened the previously published nuclear interactome of SANS in HEK293T cells [12] for importins and exportins. In the GO-term gene clusters "nuclear import" (GO:0051170) and "nuclear export" (GO:0051168) (Cytoscape plugin ClueGO, https://apps.cytoscape.org/apps/cluego, accessed on 6 June 2024; Table S1), we identified eight nuclear importins and three exportins including exportin-1/CRM1, the main nuclear protein exporter (Table 4).

Table 4. Nuclear exportins and importins identified as potential SANS-interacting proteins in the nucleus [12].

Gene	Protein	Export/Import	NLS/NES Recognition
KPNB1	Importin-β	Protein importer	classic NLS [20] non-classic NLS [20]
IPO4	Importin-4	Protein importer	classic NLS [29] non-classic NLS [20]
IPO5	Importin-5	Protein importer	classic NLS [30] non-classic NLS [20]
IPO7	Importin-7	Protein importer	classic NLS [31] non-classic NLS [20]
IPO8	Importin-8	Protein importer	classic NLS [31] non-classic NLS [20]
IPO9	Importin-9	Protein importer	non-classic NLS [20]
IPO11	Importin-11	Protein importer	non-classic NLS [20]
IPO13	Importin-13	Protein importer	classic NLS [32] non-classic NLS [32]
XPO1	CRM1/Exportin-1	Protein exporter	NES
XPO5	Exportin-5	dsRNA exporter	-
XPOT	Exportin-T	amino-acylated tRNAs export	-

Subsequently, we investigated their role by applying commercially available importin and exportin inhibitors to eYFP-SANS-transfected HeLa cells followed by confocal microscopy analysis and quantification with CellProfiler [26]. Applying the importin-β inhibitor Importazole (IPZ) to transfected HeLa had no effect on eYFP-SANS subcellular localization (Figure S6A,B). Further, we investigated the role of the exportin CRM1 in SANS nuclear export by treating eYFP-SANS HeLa cells with the CRM1 inhibitor Leptomycin-B (LMB) [33]. Confocal microscopy and CellProfiler-based quantification of the subcellular localization of SANS revealed that applications of LMB to the cells resulted in a significant increase in the nuclear localization of SANS when compared to the untreated control (Figure 2A,B). In contrast, treatments with the LMB solvent DMSO had no effect on the nuclear localization. Combined, the treatment revealed that the core export of SANS is mediated by CRM1.

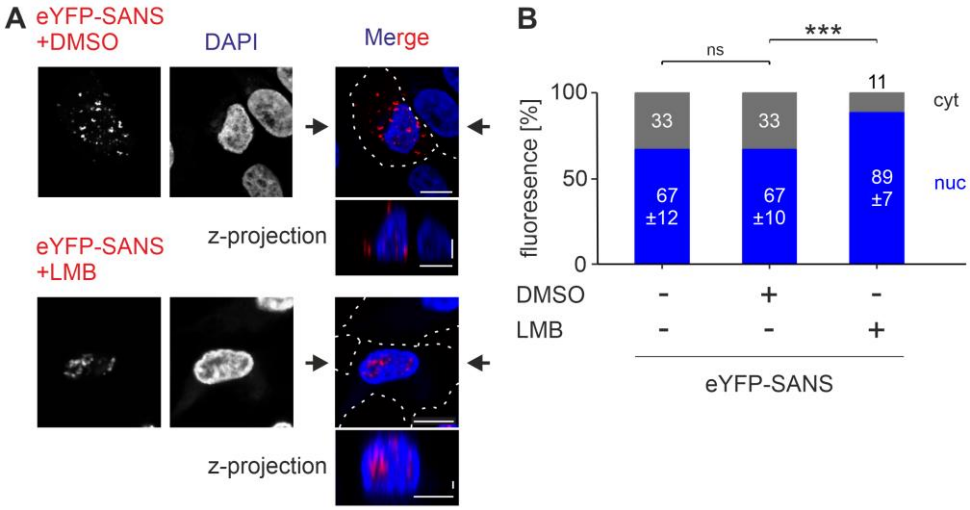

Figure 2. Nuclear localization of SANS in HeLa after treatment with the exportin CRM1 inhibitor Leptomycin-B. (**A**) Confocal microscopy of HeLa cells transfected with eYFP-SANS (red) and treated with 5 nM CRM1 inhibitor Leptomycin-B (LMB) or its solvent DMSO. (**B**) Quantification of (A) by CellProfiler. eYFP-SANS was significantly enriched in the nucleus after LMB treatment. Black arrows: position of Z-projections. Scale bars: horizontal = 10 µm; vertical = 2 µm. Data show mean values ± standard deviation from three independent experiments. Student's *t*-test was performed for three independent experiments with a minimum of 75 cells; ns = not significant; *** = $p \leq 0.0009$.

3.3. In Silico Prediction and Evolutionary Conservation of Nuclear Localization Sequences (NLSs) and Nuclear Export Sequences (NESs) in SANS

For nuclear transport, karyopherins bind to nuclear localization sequences (NLSs) and nuclear export sequences (NESs) present in the cargo molecules [20]. To identify NLSs and NESs in the human SANS sequence, we used the prediction tools NLStradamus [24] and LocNES [25], respectively (Table 5). In addition, the predicted consensus sequences were scored from 0 to 1.

Table 5. Nuclear localization (NLSs) and export sequences (NESs) of SANS predicted by LocNES and NLStradamus.

NLS/NES	Sequence	Score	CRM1-Class	NLS/NES Mutations
NLS_1$^{213–224}$	213-KTKMQKKLERRK-224	0.733	-	K213E: ETKMQKKLERRK
NLS_2$^{436–447}$	436-RKKILGAVRRRR-447	0.679	-	R447W: RKKILGAVRRRW
NES_1$^{181–195}$	181-LTSSTLSRRLQHLAL-195	0.262	1a	L195E: LTSSTLSRRLQHLAE
NES_2$^{235–249}$	235-EDGRKSARSLSGLQL-249	0.250	1b	L249E: EDGRKSARSLSGLQE
NES_3$^{406–420}$	406-ALLRQEKIDLEALML-420	0.462	2	n.a.

NLStradamus predicted two NLSs within SANS, located in the CENTn2 (NLS_1$^{213–224}$) and SAM domains (NLS_2$^{436–447}$), with scores of 0.733 and 0.679, respectively, both above the NLS threshold of 0.6 [24] (Figure 3A). LocNES identified three NESs within SANS, two in the CENTn2 domain (NES_1$^{181–195}$ and NES_2$^{235–249}$) and one in the SAM domain (NES_3$^{406–420}$), with scores ranging from 0.250 to 0.462, all above the NES threshold of 0.1 [25] (Figure 3A). In addition, we classified the predicted NESs into distinct classes of NES motifs binding to the exportin CRM1 (Table 2).

Sequence alignments of the identified NLS and NES motifs of SANS across five diverse vertebrates from humans to frogs, namely *H. sapiens*, *M. nemestrina*, *M. musculus*, *D. rerio*, and *X. laevis* revealed high to medium conservation of the motifs (Figure 3B–F). Notably, *D. rerio* and *X. laevis* have two and three *Ush1g* genes encoding SANS, respectively. However, all sequences of the predicted NLSs and NESs in the multiple genes of the respective species are identical.

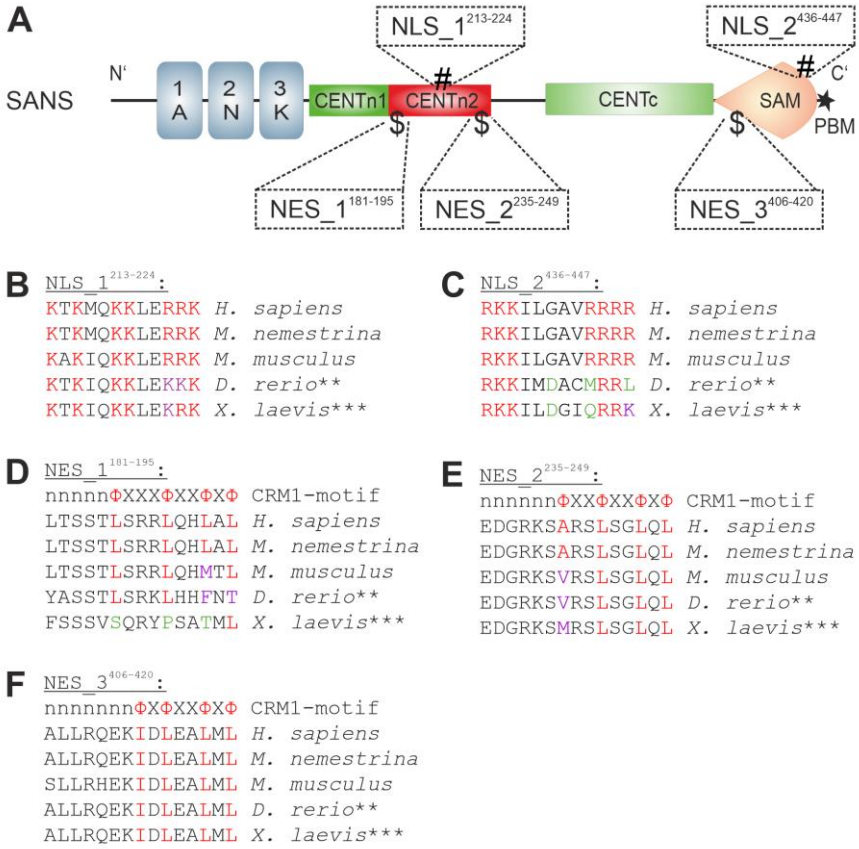

Figure 3. Prediction of nuclear localization sequences (NLSs) and nuclear export sequences (NESs) of SANS. (**A**) Three NESs ($; NES_1$^{181–195}$, NES_2$^{235–249}$, NES_3$^{406–420}$) and two NLSs (#; NLS_1$^{213–224}$, NLS_2$^{436–447}$) were predicted for SANS by NLStradamus and LocNES. (**B**–**F**) Conservation of SANS NLS_1$^{213–224}$ (**B**), NLS_2$^{436–447}$ (**C**), NES_1$^{181–195}$ (**D**), NES_2$^{235–249}$ (**E**), and NES_3$^{406–420}$ (**F**) with blastp in comparison to human SANS for five model organisms. In (**B**,**C**), positively charged residues (red), arginine-to-lysine exchanges (purple), and charge changes (green) are indicated in NLSs. In (**D**–**F**), in the first line, the position of consensus amino acid residues in the CRM1 motif is indicated in red. Valid (purple) and invalid (green) residue changes in the consensus sequence of the CRM1 motif are indicated. ** and *** indicate that the genomes of *D. rerio* and *X. laevis* possess two and three *Ush1g* genes encoding for SANS orthologs, respectively, which do not differ in the NLS and NES sequences.

Both NLSs are 100% conserved throughout all the three mammals. In NLS_1$^{213–224}$ of *D. rerio* and *X. laevis*, we observed exchanges of two positively charged amino acids, namely arginine to lysine. However, in NLS_2$^{436–447}$ of both species, exchanges between charged and uncharged amino acids were found.

The CRM1-consensus motif of NES_3$^{406–420}$ is 100% conserved throughout all vertebrate species tested. In contrast, NES_1$^{181–195}$ was conserved in all vertebrates except for *X. laevis*. NES_2$^{235–249}$ was also conserved in all tested species but differed in its starting residue in *M. musculus*, *D. rerio*, and *X. laevis*. Taken together, in silico analyses predicted two NLSs and three NES/CRM1 motifs in SANS that differ in their probabilities and evolutionary conservation in vertebrates.

3.4. Analysis of the Nuclear Localization Efficiency of Predicted NLSs in SANS in the Cell

Next, we examined the efficiency of the two predicted NLSs of SANS in cells. Using site-specific mutagenesis, we mutated positively charged residues to uncharged or negatively charged residues in the NLSs of human SANS that should prevent karyopherin binding to the mutated NLS (Table 5, Figure 4A). eYFP-tagged wild-type SANS and SANS

NLS mutants (SANS^{K213E}/ΔNLS_1$^{213–224}$, SANS^{R447W}/ΔNLS_2$^{436–447}$) were transfected into HeLa cells (Figure 4B) and HEK293T cells (Figure S5A), and the subcellular distribution of the SANS variants was then assessed by confocal microscopy. Confocal images and their z-projections of eYFP-tagged SANS^{K213E} and SANS^{R447W} indicated an increase in SANS in the cytoplasm of HeLa and HEK293T cells. The speckles formed by the SANS-NLS mutants were not stained with the commercial aggresome staining kit (Figure S3C), indicating that they are not aggresomes.

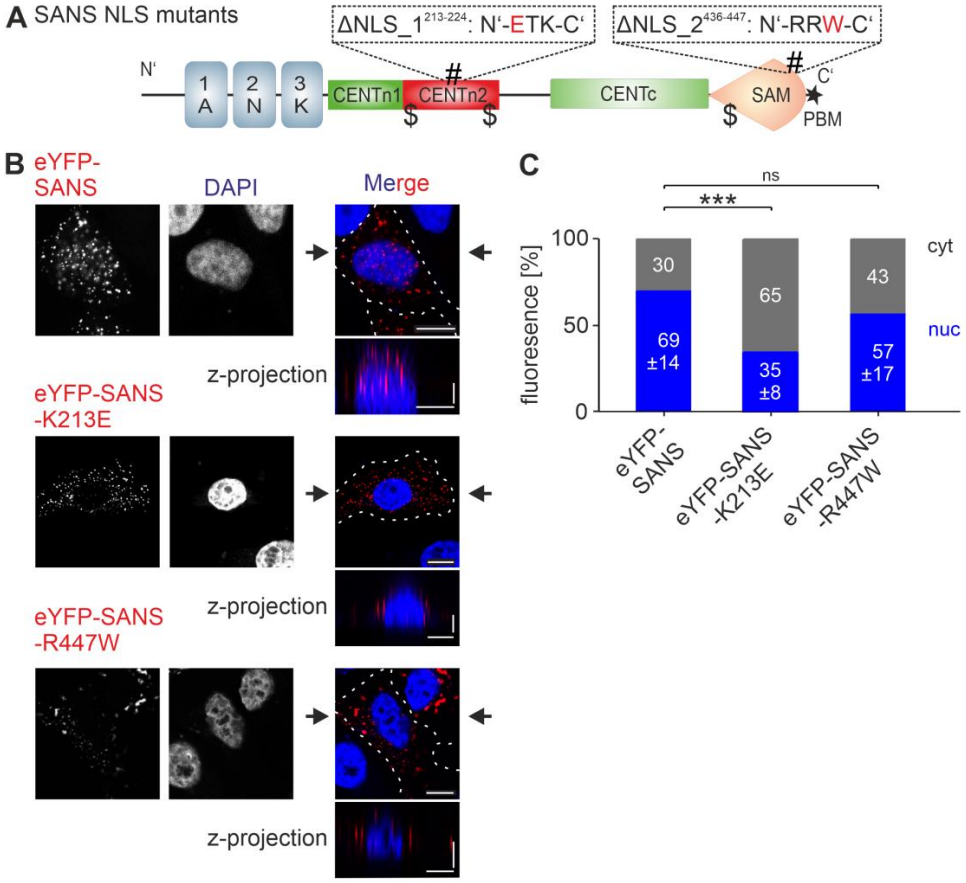

Figure 4. Subcellular localization of SANS NLS mutants. (**A**) Domain structure of SANS; the two NLS (#) mutants K213E (ΔNLS_1$^{213–224}$) and R447W (ΔNLS_2$^{436–447}$) are indicated above the cartoon. (**B**) Confocal microscopy of HeLa cells transfected with eYFP-SANS (red) or SANS NLS mutants, counterstained with DAPI. (**C**) Quantification of (**B**) by CellProfiler. eYFP-SANS^{K213E} differed significantly from eYFP-SANS. Black arrows: position of Z-projections. Scale bars: horizontal = 10 µm; vertical = 2 µm. Data show mean values ± standard deviation from three independent experiments. Student's *t*-test was performed for three independent experiments with a minimum of 75 cells. ns = not significant; *** = $p \leq 0.0009$.

CellProfiler-based quantification of the SANS localization showed a significant decrease in nuclear localization of SANS^{K213E} (ΔNLS_1$^{213–224}$) compared to wild-type SANS in both HeLa and HEK293T cells (Figures 4C and S5B). Analysis of SANS^{R447W} (ΔNLS_2$^{436–447}$) showed a decrease in its nuclear localization that was not significant in HeLa cells but was significant in HEK293T cells (Figures 4C and S5B). In summary, our findings indicate that NLS_1$^{213–224}$ has a stronger role in the nuclear localization of SANS than NLS_2$^{436–447}$.

3.5. Analysis of the Nuclear Export Efficiency of Predicted NESs in SANS in the Cell

We examined the nuclear export efficiency of the predicted NESs of SANS in the cell. We designed and generated SANS NES mutants by exchanging hydrophobic residue leucine (L) for glutamic acid (E) by site-specific mutagenesis for SANS NES_1$^{181–195}$ and

SANS NES_2$^{235–249}$ (Table 5, Figure 5A). This resulted in SANS^{L195E} (ΔNES_1$^{181–195}$) and SANS^{L249E} (ΔNES_2$^{235–249}$), which were no longer predicted as NESs by LocNES.

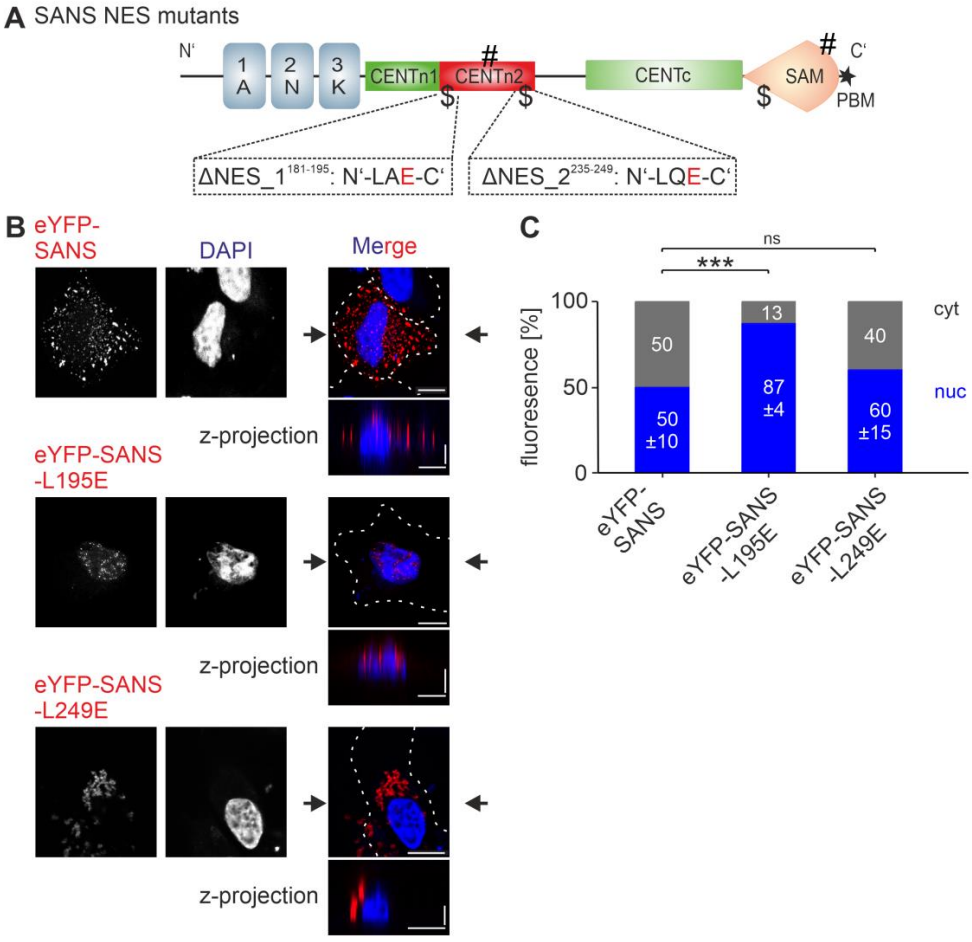

Figure 5. Localization of SANS NES mutants. (**A**) Domain structure of SANS; the two NES ($) mutants L195E (ΔNES_1$^{181–195}$) and L249E (ΔNES_2$^{235–249}$) are indicated below the cartoon. (**B**) Confocal microscopy of HeLa cells transfected with eYFP-SANS (red) or NES mutants, counterstained with DAPI. (**C**) Quantification of (**B**) by CellProfiler. eYFP-SANS^{L195E} was significantly enriched in the nucleus compared to eYFP-SANS. Black arrows: position of Z-projections. Scale bars: horizontal = 10 μm; vertical = 2 μm. Data show mean values ± standard deviation from three independent experiments. Student's *t*-test was performed for three independent experiments with a minimum of 75 cells. ns = not significant; *** = $p \leq 0.0009$.

The two NES mutants were tagged with eYFP, transfected into HeLa and HEK293T cells, and examined by confocal microscopy (Figures 5B and S7A). Unexpectedly, eYFP-SANS^{L249E} formed prominent cytoplasmic speckles, while eYFP-SANS^{L195E} predominantly localized in small nuclear droplets, as shown by z-projection. The speckles formed by the SANS-NES mutants were not stained with the commercial aggresome staining kit (Figure S3D), indicating that they are also not aggresomes. CellProfiler-based quantifications showed no significant difference in the nuclear–cytoplasmic ratio of eYFP-SANS^{L249E} (ΔNES_2$^{235–249}$) compared with eYFP-SANS (Figures 5C and S7B). In contrast, the quantification for eYFP-SANS^{L195E} (ΔNES_1$^{181–195}$) exhibited a significant increase in the nuclear localization compared to eYFP-SANS. These findings suggest that NES_1$^{181–195}$ but not NES_2$^{235–249}$ plays a role in SANS nuclear export.

Unfortunately, we failed to design any synthetic mutant for SANS NES_3$^{406–420}$ since all genetic modifications introduced by site-specific mutagenesis in this region led to the emergence of a new NES in near proximity. Therefore, we decided to evaluate the role of

SANS NES_3$^{406–420}$ in deletion constructs lacking the domains containing NES_3$^{406–420}$. The confirmed pathogenic frameshift variants of the human *USH1G* gene, SANS^{S278Pfs*71} and SANS^{S243*} (www.LOVD.nl/USH1G, accessed on 4 January 2023), which result in a premature stop at the end of CENTn2 or CENTc domain of SANS, respectively, fulfill this criterion (Figure 6A). Confocal microscopy of eYFP-tagged SANS^{S278Pfs*71} and SANS^{S243*} expressed in HeLa and HEK293T cells revealed enrichments of the pathogenic variants in the nucleus when compared to wild-type SANS, as indicated by z-projection (Figures 6B and S8A). CellProfiler-based quantifications confirmed the significant enrichment of both pathogenic variants in the nucleus compared to eYFP-SANS (Figures 6C and S8B). The retention of SANS^{S278Pfs*71} and SANS^{S243*} in the nucleus indicates that NES_3$^{406–420}$ plays an additional pivotal role in SANS nuclear export.

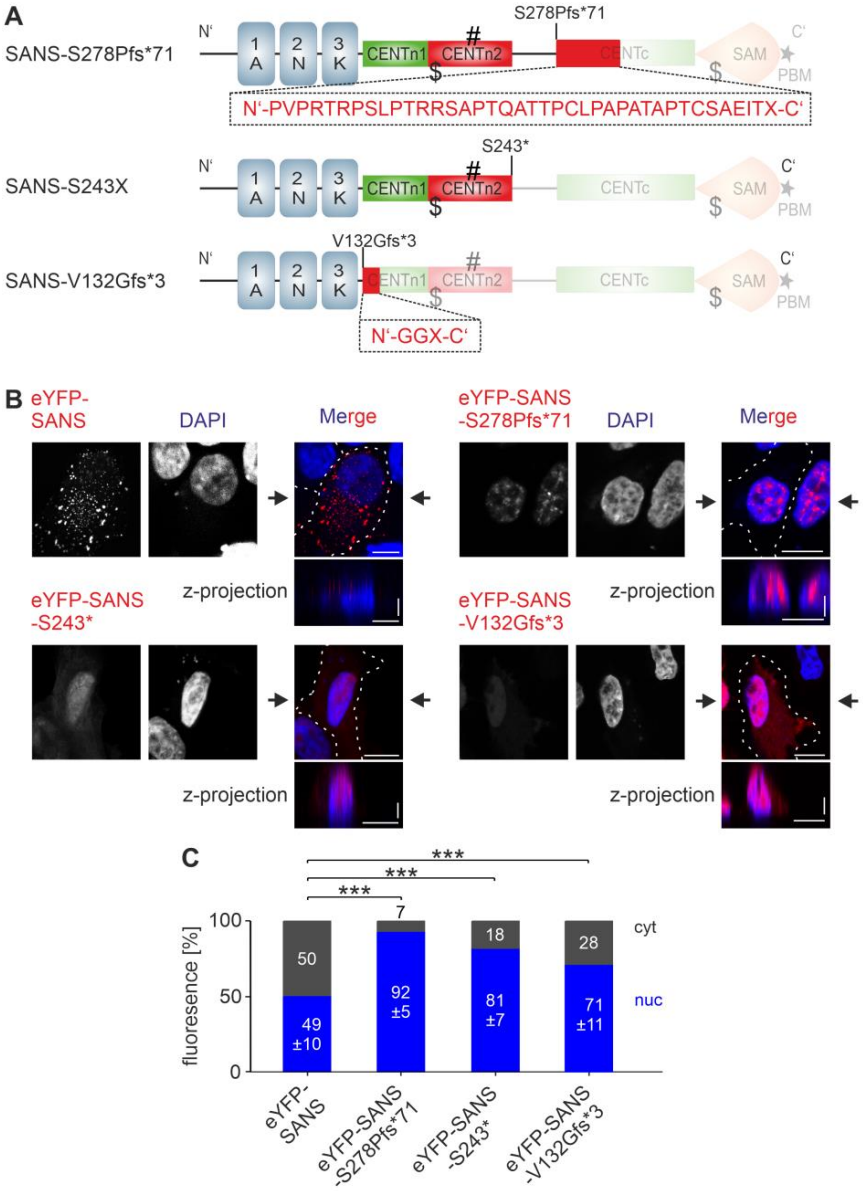

Figure 6. Localization of pathogenic variant of SANS in HeLa cells. (**A**) The pathogenic variant SANS^{S278Pfs*71} and SANS^{V132Gfs*3} are frameshift mutations which lead to missense extension (red boxes and amino acid sequences below) and a premature stop in CENTc or CENTn1, respectively. The pathogenic variant SANS^{S243*} has a premature stop codon after the CENTn2 domain. (**B**) Confocal microscopy of HeLa cells transfected with eYFP-SANS (red), eYFP-SANS^{S278Pfs*71}, eYFP-SANS^{S243*}

and eYFP-SANS^{V132Gfs*3}, counterstained with DAPI. (**C**) Quantification of (**B**) with CellProfiler. All pathogenic variants were significantly enriched in the nucleus. Black arrows: position of z-projections. Scale bars: horizontal = 10 µm; vertical = 2 µm. Data show mean values ± standard deviation from three independent experiments. Student's *t*-test was performed for three independent experiments with a minimum of 75 cells. *** = $p \leq 0.0009$.

In addition, we investigated the cellular localization of the frameshift mutation SANS^{V132Gfs*3}, which lacks almost the entire CENTn1 and all following C-terminal domains including all NLSs and NESs (Figure 6A). eYFP-tagged SANS^{V132Gfs*3} localized predominantly in the nucleus of HeLa and HEK293T cells, as indicated by z-projection (Figures 6B and S8A). CellProfiler-based quantifications confirmed the significant enrichment of SANS^{V132Gfs*3} in the nucleus compared to eYFP-SANS (Figures 6C and S8B).

Taken together, our findings suggest that NES_1$^{181–195}$ and NES_3$^{406–420}$ but not NES_2$^{235–249}$ play a role in SANS nuclear export. Furthermore, the present results on SANS pathogenic variants also suggest that alterations in nuclear shuttling may be part of the pathomechanisms leading to USH1G.

3.6. Effcts of NLS and NES Mutations of SANS on the Binding to Compartment-Specific Interaction Partners

To fulfill its diverse functions specific for the different compartments in the cell, SANS interacts with compartment-specific interaction partners; for example, in the cytoplasm with scaffold protein harmonin and in the nucleus with splicing factor PRPF31 [4,6,12,34]. Both interacting partners bind to different domains in SANS. While harmonin binds to the SAM-PBM domain, PRPF31 binds to the CENTn1 domain [4,12,15] (Figure 7A). Both SANS^{K213E} (ΔNLS_1) and SANS^{L195E} (ΔNES_1) are located within the CENTn2 domain and should not directly affect the binding of harmonin or PRPF31. However, these mutations may potentially alter the overall structure of SANS, which may influence these interactions. To investigate this, we used the in silico prediction tool Missense3D [35]. Missense3D predicted no structural changes upon mutation of SANS^{K213E} nor SANS^{L195E} (Table S2). In addition, Missense3D-PPI, a pipeline for structural changes in protein–protein interfaces [36], did not predict any structural surface alterations to the previously modeled SANS-PRPF31 and SANS-harmonin complexes (Table S2) [4].

Next, we tested the effects of the SANS^{K213E} (ΔNLS_1) and SANS^{L195E} (ΔNES_1) mutants on their binary interactions with harmonin and PRPF31 in the nucleus of the cell by using fluorescence resonance energy transfer (FRET) acceptor photobleaching assays (Figure 7B) [4]. We co-transfected HeLa cells with eYFP-SANS, eYFP-SANS^{K213E}, or eYFP-SANS^{L195E} and harmonin-eCFP or eCFP-PRPF31, respectively, and determined FRET signals in the nucleus, normalized to 1 by the positive control eCFP-c-eYFP. The FRET pairs eYFP-SANS-harmonin-eCFP and eYFP-SANS^{K213E}-harmonin-eCFP generated normalized FRET signals of the same height, significantly higher than those of the pair eYFP-SANS^{L195E}-harmonin-eCFP (Figure 7C). In contrast, the FRET pairs eYFP-SANS-eCFP-PRPF31 and eYFP-SANS^{L195E}-eCFP-PRPF31 generated normalized FRET signals of the same height, significantly higher than those of eYFP-SANS^{K213E}-eCFP-PRPF31.

Taken together, the ΔNES and ΔNLS SANS mutants still have the potential to bind to SANS binding partners. However, in the cell, ΔNES SANS sticks in the nucleus and is no longer available together with harmonin for its cytoplasmic functions, and ΔNLS_1 SANS cannot interact with PRPF31 in the nucleus for a spliceosome function because it is not targeted into the nucleus.

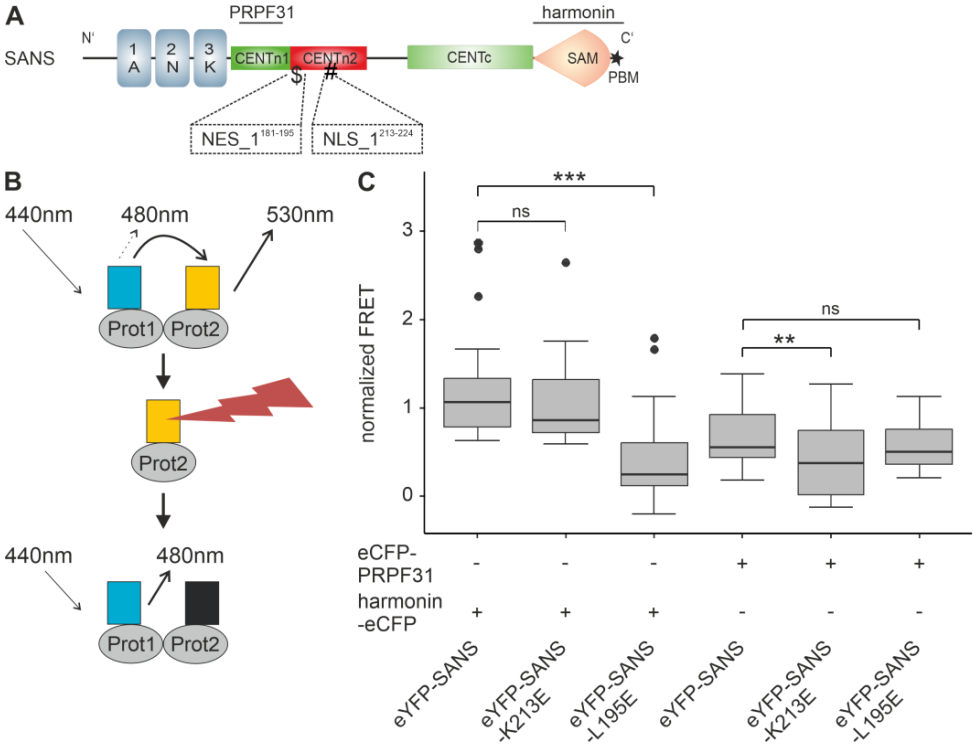

Figure 7. Validation of the interaction of SANS NLS/NES mutants with SANS binding partners fluorescence resonance energy transfer (FRET) in the nuclear compartment. (**A**) Schematic of the SANS domain structure indicating NES1 and NLS1 and the regions for harmonin and PRPF31 binding, black lines in SANS SAM-PBM and CENTn1, respectively. (**B**) Illustration of the FRET acceptor bleach assay. Interaction of two proteins, either eCFP (blue)- or eYFP (yellow)-tagged, leads to FRET (upper). If the acceptor (eYFP) is bleached (flash) (middle), increased emission of the donor (eCFP) can be measured (lower). (**C**) FRET acceptor bleach assay in the nucleus of co-transfected HeLa cells. FRET efficiencies were normalized to 1 by the fused eCFP-c-eYFP FRET pair (positive control). FRET pairs eYFP-SANS^{L195E}-harmonin-eCFP and eYFP-SANS^{K213E}-eCFP-PRPF31 showed a significant decrease in interaction compared to eYFP-SANS. Outliers are shown as dots above the boxplots. Wilcoxon signed-rank test was performed for three independent experiments. ns = not significant; *** = $p \leq 0.0009$; ** = $p \leq 0.009$.

3.7. SANS and Its Paralog ANKS4B Are Localized to Different Subcellular Compartments

SANS and its paralog ANKS4B have nearly the same principal domain structure (Figure 1A), possess a homology of up to 80% in their amino acid sequences, and share common binding partners, such as USH1C/harmonin [5,14–16]. Since the differences in cellular function of closely related proteins often depend on the different spatial arrangements in the cell, we tested whether SANS and ANKS4B differ in their cytoplasmic/nuclear localization.

To determine the subcellular localization of ANKS4B, we analyzed eYFP-tagged ANKS4B in comparison to eYFP-SANS-expressing HeLa cells (Figure 8). Confocal microscopy showed that eYFP-ANKS4B was mainly found in the cytoplasm (Figure 8A), but also occasionally to a lesser extent in the nucleus (Figure 8B). CellProfiler-based quantification demonstrated significantly lower nuclear localization of eYFP-ANKS4B compared to eYFP-SANS (Figure 8C).

NLStradamus predicted no NLS for ANKS4B. However, LocNES predicted six distinct NESs of various CRM1-binding motif classes for ANKS4B spanning its SAM-domain (Table S3) and predicted scores higher than 0.1, the threshold of LocNES [24].

To test whether these motifs are relevant for the subcellular localization, we treated eYFP-ANKS4B-transfected HeLa cells with the CRM1 inhibitor LMB (Figure 8D). CellProfiler-

based quantification demonstrated that the LMB treatment resulted in a significant increase in eYFP-ANKS4B in the nucleus, which was not observed in DMSO-treated control cells (Figure 8E).

Taken together, in contrast to SANS, the SANS paralog ANKS4B is predominantly localized in the cytoplasm guaranteed by nuclear export based on CRM1 exportins.

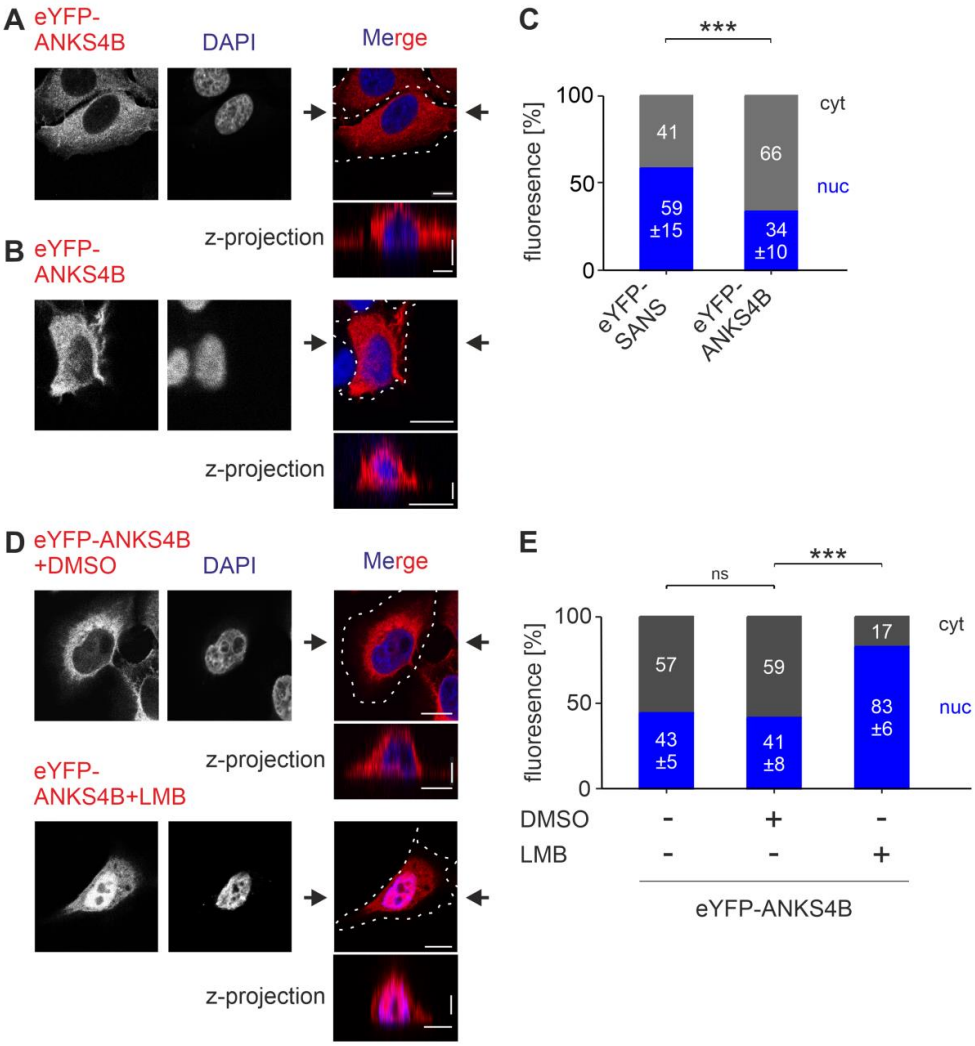

Figure 8. Comparison of the nuclear–cytoplasmic localization of SANS and its paralog ANKS4B in HeLa cells. (**A**,**B**) Confocal microscopy of HeLa cells transfected with eYFP-ANKS4B (red), counterstained with DAPI. (**C**) Quantification with CellProfiler for eYFP-SANS- and eYFP-ANKS4B-transfected cells. eYFP-ANKS4B was highly enriched in the cytoplasm compared to eYFP-SANS. (**D**) Confocal microscopy of HeLa cells transfected with eYFP-ANKS4B (red), counterstained with DAPI. Cells were treated with DMSO or 5 nM Leptomycin-B (LMB), an established inhibitor for CRM1. (**E**) Quantification of (**D**) with CellProfiler. eYFP-ANKS4B was highly enriched in the nucleus after treatment with LMB. Black arrows: position of Z-projections. Scale bars: horizontal = 10 µm; vertical = 2 µm. Data show mean values ± standard deviation from three independent experiments. Student's *t*-test was performed for 3 independent experiments with a minimum of 75 cells. ns = not significant; *** = $p \leq 0.0009$.

3.8. SANS and Its Paralog ANKS4B Differentially Interact with PRPF31

Next, we tested whether SANS and ANKS4B also differ in their binary interaction with the splicing molecule PRPF31 by FRET acceptor photobleaching assays. For this we co-transfected HeLa cells with eYFP-SANS or eYFP-ANKS4B, respectively, and eCFP-PRPF31. As controls, we used eYFP alone and harmonin-eCFP, which was previously shown to bind

to ANKS4B and SANS [5,17]. FRET signals were normalized to 1 by the positive control eCFP-c-eYFP. The FRET pair eYFP-SANS-eCFP-PRPF31 generated significantly higher normalized FRET signals than the control pair eYFP-eCFP-PRPF31, confirming the binary binding of SANS and PRPF31 (Figure 9A) [4,12]. In contrast, the eYFP-ANKS4B-eCFP-PRPF31 FRET pair showed no increase in normalized FRET efficiencies when compared to the control eYFP-eCFP-PRPF31 pair. The height of the normalized FRET signals of eYFP-ANKS4B-harmonin-eCFP was in the range of the FRET signals of the FRET pair eYFP-SANS-eCFP-PRPF31 and significantly higher than the signals of the eYFP-eCFP-PRPF31 control pair, confirming the interaction of ANKS4B with harmonin as previously reported [17].

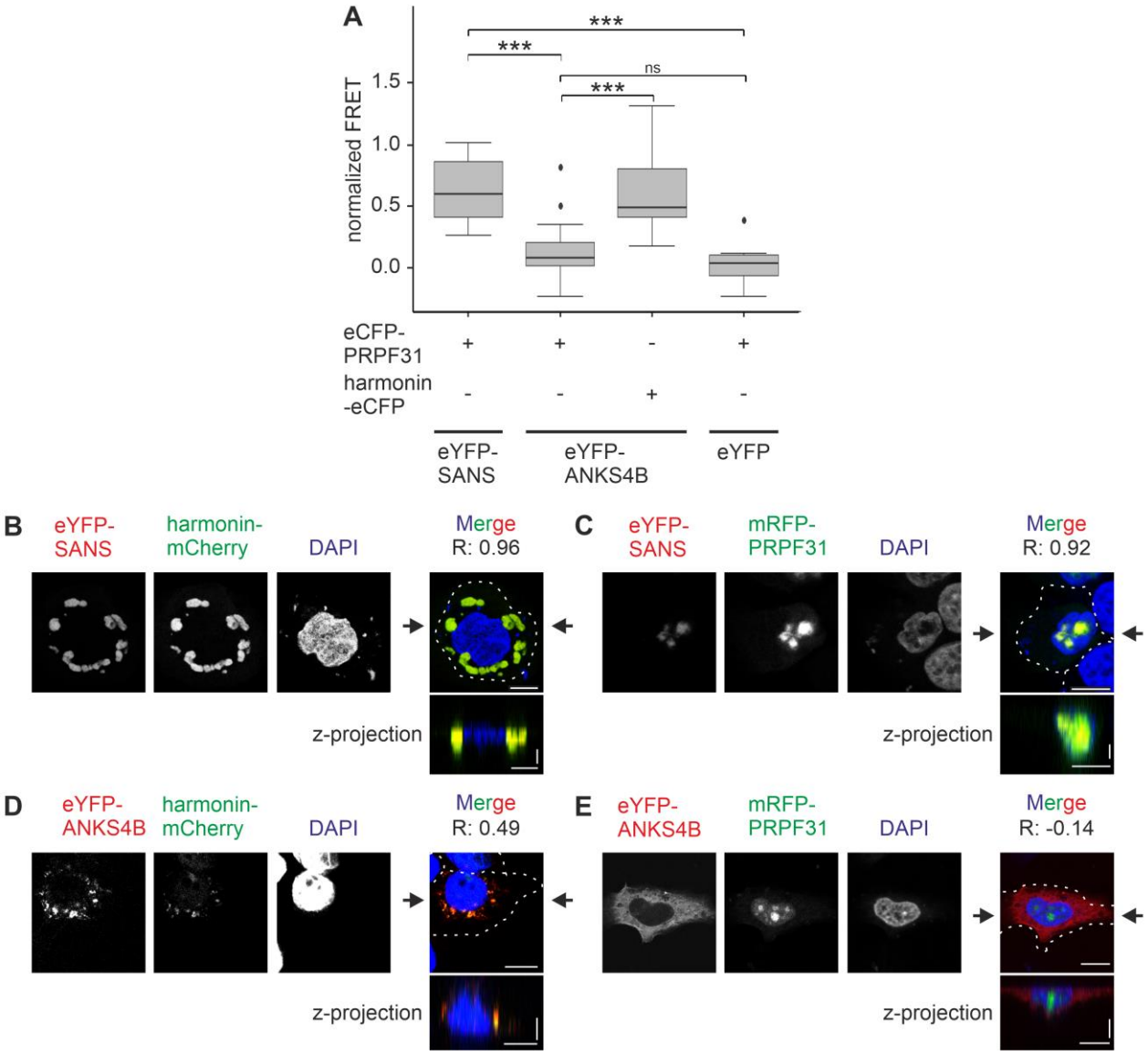

Figure 9. ANKS4B binary interaction in the nucleus. (**A**) FRET assay in co-transfected HeLa cells. FRET efficiencies were normalized to 1 by the fused eCFP-c-eYFP FRET pair (positive control). FRET pair eYFP-ANKS4B-eCFP-PRPF31 does not show a significant increase in the normalized FRET efficiencies when compared to eYFP FRET pair negative controls. Outliers are shown as dots above/below the boxplots. Dunn's test after a Kruskal–Wallis test was performed for three independent experiments. (**B**–**E**) Confocal microscopy of HeLa cells co-transfected with eYFP-SANS

(red, (**B**,**C**)) or eYFP-ANKS4B (red, (**D**,**E**)) and harmonin-mCherry (green) or mRFP-PRPF31 (green), counterstained with DAPI. eYFP-ANKS4B only co-localized with harmonin-mCherry but not with mRFP-PRPF31. Black arrows: position of Z-projections. Scale bars: horizontal = 10 µm; vertical = 2 µm. Pearson coefficient R values indicate co-localization. ns = not significant; *** = $p \leq 0.0009$.

Next, we co-expressed eYFP-SANS or eYFP-ANKS4B with mRFP-PRPF31 or harmonin-mCherry, respectively, in HeLa cells for subsequent confocal microscopy analyses (Figure 9B–E). Our analyses revealed that ANKS4B co-localized with harmonin in small droplets in the cytoplasm as observed before (Figure 9D) [14], but did not colocalize with PRPF31 in the nucleus, strengthened by the negative Pearson coefficient (R = −0.14) (Figure 9E). In contrast, SANS co-localized with both harmonin and PRPF31, but in different compartments, namely in large speckles in the cytoplasm and in the nucleus, respectively (Figure 9B,C). Both co-localizations were supported by high positive Pearson coefficients (R = 0.96 and 0.92, respectively). This finding suggested that SANS nuclear–cytoplasmic shuttling is additionally controlled by the interaction with partner proteins. However, siRNA-based knockdown of endogenous PRPF31 showed no alteration of eYFP-SANS in HeLa cells (Figure S9), which might be due to the low expression of the endogenous PRPF31.

We also like to note that there are differences in the size of the speckles of eYFP-SANS/harmonin-mCherry and eYFP-ANKS4B/harmonin-mCherry in the cytoplasm (Figure 9B,D). This is probably since the two eYFP-tagged proteins are differentially expressed (Figure S1): the more highly expressed eYFP-SANS possibly recruits more harmonin-mCherry molecules, and correspondingly larger speckles are formed.

In summary, our findings underscore the divergent nuclear localization/export sequences between SANS and the ANKS4B paralog resulting in differential subcellular localization patterns and cellular functions.

4. Discussion

The protein traffic across the nuclear pores is mostly mediated by members of the karyopherin-β (or Kap) family commonly known as importins and exportins which specifically recognize NLSs and NESs of the cargo molecules [20]. In the present study, we provide several lines of evidence that the nuclear localization of SANS is regulated by an interplay of importins and exportins. We identified several importins and exportins in the previously described nuclear interactome of SANS [12]. In addition, confocal microscopy showed that Leptomycin-B, a specific inhibitor of CRM1 export, blocks the nuclear export of SANS. Mechanistically, Leptomycin-B binds covalently to the NES binding cleft of CRM1 and thereby competes with the cargo, in this case, SANS, for binding to CRM1 [37]. This also confirms the molecular interaction of SANS with CRM1 as we expected from our SANS interactome data. In silico predictions revealed evolutionary conserved NLSs and NESs in the SANS sequences allowing the binding of importins and exportins. We experimentally confirmed the function of in silico predicted NLSs and NESs by quantifying the subcellular localization of SANS mutants in situ.

Multiple NLSs and NESs have been previously described for nuclear proteins, such as Fanconi anemia group A protein (FANCA) and enzyme 5-lipoxygenase (5-LO), respectively [38,39]. Our data on the two NLSs suggest that NLS_1$^{213–224}$ localized in the central domain of SANS is the major NLS for the nuclear localization of SANS. In comparison to the C-terminal NLS_2$^{436–447}$, NLS_1$^{213–224}$ scored higher in the predictions [24]. In addition, sequence alignments across vertebrates suggest that NLS_2$^{436–447}$ is less conserved. In NLS_2$^{436–447}$, charged amino acids are exchanged for uncharged in lower vertebrates, probably affecting the interaction with importins. Importin binding is based on interactions with positively charged amino acids in NLSs of nuclear proteins [20], and exchanges to uncharged residues have been shown to alter NLS binding to importins [40]. In our study, we also experimentally induced such modifications by site-specific mutations of the NLSs in SANS. The quantitative data obtained showed that the decrease in nuclear localization of SANS with a mutated NLS_1$^{213–224}$ was highly significant in both HeLa and HEK293T

cells. In contrast, mutated NLS_2$^{436–447}$ did not lead to a significant decrease in the nuclear localization of SANS in HeLa cells and only to a decrease in lower significance in HEK293T cells. The observed differences between the cell lines in the distribution of proteins between the nucleus and cytoplasm are consistent with previous studies relating them to differences in metabolism between the cell lines [41–43].

Based on these data, we hypothesize that importins preferentially bind to NLS_1$^{213–224}$ of SANS for the import into the nucleus, e.g., to accomplish SANS's nuclear role in pre-mRNA splicing. Interestingly, NLS_1$^{213–224}$ is present in the central domain of SANS, which represents the major binding site for numerous SANS-interacting proteins [7,10,12]. Thus, the binding of cytoplasmic proteins such as myomegalin and whirlin to the central domain [7,10] is likely to compete with the binding of importins to the NLS_1$^{213–224}$. The competition in binding between importins and other cytoplasmic binding partners as a mechanism controlling the nuclear–cytoplasmic shuttling of nuclear proteins has been described previously [44,45]. Accordingly, the binding competition of cytoplasmic interaction partners of SANS and importins to the NLS sites could guarantee its cytoplasmic localization and thus ensure its cytoplasmic functions, e.g., in intracellular transport or ciliogenesis [7,9,11].

In addition, the binding of nuclear proteins may also facilitate nuclear import in a process known as "piggybacking" [46,47]. Since SANS was not completely removed from the nucleus when NLS_1$^{213–224}$ was mutated, and the overexpression of PRPF31 resulted in almost complete nuclear localization of co-expressed eYFP-SANS, we speculated that PRPF31 may play a piggyback role for SANS during nuclear import. However, since siRNA-mediated silencing of endogenous PRPF31 did not alter the nuclear–cytoplasmic shuttling of SANS, we rejected this hypothesis. Alternatively, binding of importins to NLS_2$^{436–447}$ or binding of the identified importins, found in the SANS interactome, to non-classical NLSs, which are not predictable by prediction tools, may compensate for an absence of NLS_1$^{213–224}$.

Inhibition of the nuclear export by LMB suggests CRM1-dependent nuclear export of SANS. The analysis of the three predicted NESs of SANS suggests NES_1$^{181–195}$ of the CENTn2 domain and NES_3$^{406–420}$ of the SAM domain as the major NESs for the nuclear–cytoplasmic shuttling of SANS. All three predicted NESs are above the threshold for qualifying NESs and are highly conserved, except for NES_2$^{235–249}$, which differs in three of five vertebrates in the first residue. As expected for potent NESs, the site-specific mutations resulting in a non-functional NES_1$^{181–195}$ and the deletion variants of SANS lacking the NES_3$^{406–420}$ led to a highly significant increase in their nuclear localization in HeLa and HEK293T cells. In contrast, mutated NES_2$^{235–249}$ did not lead to a significant increase in its nuclear localization. Interestingly, NES_1$^{181–195}$ and NES_3$^{406–420}$ of SANS belong to different classes of CRM1 motifs that can differ in the binding affinity of CRM1 [48] and, thereby, probably also in the nuclear export efficiency.

In comparison to SANS, its paralog ANSK4B was far less abundantly localized in the nucleus, which correlates with the lack of any known nuclear function of ANKS4B [14,17]. At first glance, the absence of ANKS4B might be caused because its sequence does not contain an NLS since none of the predicted tools applied predicted an NLS for importin binding in ANKS4B, but several NESs suitable for CRM1 exportin binding. The equivalent region of ANKS4B to SANS CENTn2, where the potent NLS_1$^{213–224}$ is localized, lacks any NLS but shows a cryptic apical targeting sequence that directs ANKS4B to the microvilli at the apical membrane of epithelial cells [18]. This is further evidence that the two scaffolds have partially diverged in their molecular composition to form unique properties for the cell.

Interestingly, after inhibition of CRM1, more than 80% of the ANKS4B was located in the nucleus. This raises the question of how ANKS4B shuttles into the nucleus. In comparison to SANS (~51.5 kDa https://www.uniprot.org/uniprotkb/Q495M9/entry, accessed 1 October 2023), ANKS4B (~46 kDa https://www.uniprot.org/uniprotkb/Q8N8V4/entry, accesses 15 February 2024) is smaller, in the range of size for passive transfer through the

nuclear pore complex commonly reported as between 40 and 50 kDa [19]. However, we also found that the much larger eYFP-tagged ANKS4B ~75 kDa, which we monitored in our experiments, localized in the nucleus. A possible reason for this is that this size exclusion for free diffusion through the NPC is not as effective as assumed. Indeed, more recent findings indicate that larger macromolecules of >100 kDa can also diffuse through the NPC [49]. Alternatively, as known for other proteins and already discussed above for SANS the nuclear import of ANKS4B may also be mediated by non-canonical NLSs, nonlinear sequences, which cannot be predicted by prediction tools [20,50]. Although we could not fully elucidate the regulation of ANKS4B import into the nucleus, our results confirm the previously shown predominantly cytoplasmic localization of ANKS4B. However, once ANKS4B enters the nucleus, it is immediately exported back into the cytoplasm mediated by the CRM1 exportin. This mechanism ensures that ANKS4B is available for its primary functions in the cytoplasm.

In our present study, we found evidence that the shuttling of SANS and ANSK4B between the nucleus and cytoplasm is coordinated by the selective binding of karyopherins to NLSs and NESs and determines their compartment-specific function. In the cell, protein functions and their regulations are commonly fine-tuned by post-translational modifications such as site-specific reversible phosphorylation [43,51,52]. Therefore, it is not surprising that reversible phosphorylation also emerges as an important process for regulating the nuclear availability of proteins [53]. Interestingly, we previously demonstrated that the kinase inhibitor D-ribofuranosylbenzimidazole (DRB) increases the abundance of SANS in the nucleus due to the inhibition of the phosphorylation at S422 (see Figure S5 in [9]). S422 is a CK2 (casein kinase 2) phosphosite near NES_3$^{406–420}$. Therefore, it is tempting to speculate that CK2-mediated phosphorylation not only inhibits MAGI2 from binding to the internal PDZ-binding motif (PBM) in SANS-SAM [9] but may also regulate the binding of CRM1 to the NES.

Present confocal microscopy revealed that endogenous SANS and overexpressed tagged SANS form speckles in both the cytoplasm and the nucleus. In our study, we demonstrated that SANS speckles are not insoluble protein aggregates like aggresomes, but rather show features of protein condensates that arise through LLPS: the condensates are not stained for aggresomes; unlike stable aggregates, they are dynamic, and their SANS fraction is highly mobile; furthermore, the overexpression of interacting proteins of SANS, namely of harmonin and PRPF31, increases the size of SANS condensates. These results all suggest that the SANS speckles are formed by LLPS [54,55], which is consistent with previously reported findings [10,12,14]. In these condensates, SANS is probably serving as a scaffold through its multivalent interactions that drive LLPS and organize SANS-containing membrane-less organelles such as Cajal bodies and nuclear speckles or at the base of primary cilia in LLPS [6–12,34]. LLPS-driven condensates are in a dynamic exchange with their environment, and their components can easily be released and re-integrated [55]. Accordingly, SANS monomers or dimers in the cell could, for example, be easily released from the speckles into the cytoplasm to be transported into the nucleus and reintegrated into nuclear membrane-less organelles and vice versa.

While for the SANS-encoding *USH1G* gene, more than 70 pathogenic variants have been identified thus far as leading to deaf-blindness in patients [56] (www.LOVD.nl/USH1G, accessed on 4 January 2023), to our knowledge, defects in ANKS4B have not been associated with a disease [18]. We have previously demonstrated that pathogenic variants of USH1G/SANS variants can lead to the disruption of fundamental cellular processes in both the cytoplasm and the nucleus: while USH1G/SANS variants lead to altered ciliogenesis and intracellular transport in the cytoplasm [10,11], they cause defects in pre-mRNA splicing in the nucleus [12]. Here, we show that these SANS variants are highly enriched in the nucleus due to the defect in nuclear–cytoplasmic shuttling. It is probable that the lack of NESs leads to defects in nuclear export.

Although the SANS variants are targeted into the nucleus, they cannot fulfill their functions in the splicing process there, as we have previously demonstrated [12]. It is

possible that not all interaction partners that interact with SANS during proper activation of the spliceosome can interact with the mutated, truncated versions of the scaffold protein. Probably more importantly, due to its pathogenic mutations, SANS is no longer available for its functions in the cytoplasm. A combination of defects in possibly unbalanced cytoplasmic trafficking and ciliogenesis as well as in pre-RNA splicing in the nucleus may underlie the pathology leading to USH1G. This complex scenario may be present in the retinal cells in the eye. In the inner ear, USH1G-associated deafness is more likely caused by defects in the assembly of mechanosensitive tip-link complex in the stereocilia of auditory hair cells [13].

5. Conclusions

USH1G/SANS is a multifunctional scaffold protein that participates in various cellular processes executed in different compartments of the cell, namely in the cytoplasm or nucleus. To fulfill its specific tasks, efficient and controlled nuclear–cytoplasmic shuttling of the SANS protein is mediated by karyopherins binding to NLSs and NESs in the SANS. This is very different from its strict cytoplasmic paralog ANKS4B, in which several NESs guarantee its localization and function in the cytoplasm. Finally, we provide evidence that the dysregulation and disruption of SANS's nuclear–cytoplasmic shuttling can be relevant for the development of the USH disease in USH1G patients.

Supplementary Materials: The following supporting information can be downloaded at https://www.mdpi.com/article/10.3390/cells13221855/s1: Supplementary_Figure_File.docx: all Figures S1–S9 referred to in this work; Table_S1.xlsx: GO-term analysis of SANS nuclear interactome from [12]; Table_S2.xlsx: Missense3D prediction of SANSK213E and SANSL195E; Table S3: Predicted nuclear export sequences (NES) of ANKS4B; CellProfiler workflow available on GitHub: https://github.com/LabWolfrum/Fritze_et_al_2024_SANS_Nuclear_localization.

Author Contributions: J.S.F. set up and carried out most of the experiments. F.F.S. carried out some cloning and experiments. J.S.F. and U.W. designed the studies and wrote the manuscript. All authors have read and agreed to the published version of the manuscript.

Funding: This study was supported by funds from the FAUN-Stiftung, Nuremberg, The Foundation Fighting Blindness (FFB) [PPA-0717-0719-RAD], and DFG (Project-No.: 521147274) to U.W.

Data Availability Statement: All raw data are available through contacting the corresponding author.

Acknowledgments: We thank Ronald Roepman (Human Genetics, Nijmegen) and Katja Luck (IMB, Mainz) for the contribution of several plasmids and constructs used in this study. We thank Christof Rickert (LMCF, JGU), the Microscopy Core Facility IMB, Mark Zorin (IMP, Mainz), Ulrike Maas (IMP, Mainz), Michelle Bremser (IMP, Mainz), and Joshua Linnert (IMP, Mainz) for their technical support. J.S.F. was enrolled in the International PhD Programme (IPP) Mainz.

Conflicts of Interest: The authors declare that the research was conducted in the absence of any commercial or financial relationships that could be construed as a potential conflict of interest.

References

1. Weil, D.; El-Amraoui, A.; Masmoudi, S.; Mustapha, M.; Kikkawa, Y.; Laine, S.; Delmaghani, S.; Adato, A.; Nadifi, S.; Zina, Z.B.; et al. Usher Syndrome Type I G (USH1G) Is Caused by Mutations in the Gene Encoding SANS, a Protein That Associates with the USH1C Protein, Harmonin. *Hum. Mol. Genet.* **2003**, *12*, 463–471. [CrossRef]
2. Fuster-Garcia, C.; Garcia-Bohorquez, B.; Rodriguez-Munoz, A.; Aller, E.; Jaijo, T.; Millan, J.M.; Garcia-Garcia, G. Usher Syndrome: Genetics of a Human Ciliopathy. *Int. J. Mol. Sci.* **2021**, *22*, 6723. [CrossRef] [PubMed]
3. Delmaghani, S.; El-Amraoui, A. The Genetic and Phenotypic Landscapes of Usher Syndrome: From Disease Mechanisms to a New Classification. *Hum. Genet.* **2022**, *141*, 709–735. [CrossRef] [PubMed]
4. Fritze, J.S.; Stiehler, F.F.; Wolfrum, U. Pathogenic Variants in USH1G/SANS Alter Protein Interaction with Pre-RNA Processing Factors PRPF6 and PRPF31 of the Spliceosome. *Int. J. Mol. Sci.* **2023**, *24*, 17608. [CrossRef] [PubMed]
5. Adato, A.; Lefevre, G.; Delprat, B.; Michel, V.; Michalski, N.; Chardenoux, S.; Weil, D.; El-Amraoui, A.; Petit, C. Usherin, the Defective Protein in Usher Syndrome Type IIA, Is Likely to Be a Component of Interstereocilia Ankle Links in the Inner Ear Sensory Cells. *Hum. Mol. Genet.* **2005**, *14*, 3921–3932. [CrossRef]

6. Maerker, T.; van Wijk, E.; Overlack, N.; Kersten, F.F.J.; Mcgee, J.; Goldmann, T.; Sehn, E.; Roepman, R.; Walsh, E.J.; Kremer, H.; et al. A Novel Usher Protein Network at the Periciliary Reloading Point between Molecular Transport Machineries in Vertebrate Photoreceptor Cells. *Hum. Mol. Genet.* **2008**, *17*, 71–86. [CrossRef] [PubMed]
7. Overlack, N.; Kilic, D.; Bauss, K.; Marker, T.; Kremer, H.; van Wijk, E.; Wolfrum, U.; Bauß, K.; Märker, T.; Kremer, H.; et al. Direct Interaction of the Usher Syndrome 1G Protein SANS and Myomegalin in the Retina. *Biochim. Biophys. Acta* **2011**, *1813*, 1883–1892. [CrossRef]
8. Papal, S.; Cortese, M.; Legendre, K.; Sorusch, N.; Dragavon, J.; Sahly, I.; Shorte, S.; Wolfrum, U.; Petit, C.; El-Amraoui, A. The Giant Spectrin BetaV Couples the Molecular Motors to Phototransduction and Usher Syndrome Type I Proteins along Their Trafficking Route. *Hum. Mol. Genet.* **2013**, *22*, 3773–3788. [CrossRef]
9. Bauss, K.; Knapp, B.; Jores, P.; Roepman, R.; Kremer, H.; Wijk, E.V.; Marker, T.; Wolfrum, U. Phosphorylation of the Usher Syndrome 1G Protein SANS Controls Magi2-Mediated Endocytosis. *Hum. Mol. Genet.* **2014**, *23*, 3923–3942. [CrossRef]
10. Sorusch, N.; Baub, K.; Plutniok, J.; Samanta, A.; Knapp, B.; Nagel-Wolfrum, K.; Wolfrum, U. Characterization of the Ternary Usher Syndrome SANS/Ush2a/Whirlin Protein Complex. *Hum. Mol. Genet.* **2017**, *26*, 1157–1172. [CrossRef]
11. Sorusch, N.; Yildirim, A.; Knapp, B.; Janson, J.; Fleck, W.; Scharf, C.; Wolfrum, U. SANS (USH1G) Molecularly Links the Human Usher Syndrome Protein Network to the Intraflagellar Transport Module by Direct Binding to IFT-B Proteins. *Front. Cell Dev. Biol.* **2019**, *7*, 216. [CrossRef] [PubMed]
12. Yildirim, A.; Mozaffari-Jovin, S.; Wallisch, A.K.; Schäfer, J.; Ludwig, S.E.J.; Urlaub, H.; Lührmann, R.; Wolfrum, U. SANS (USH1G) Regulates Pre-MRNA Splicing by Mediating the Intra-Nuclear Transfer of Tri-SnRNP Complexes. *Nucleic Acids Res.* **2021**, *49*, 5845–5866. [CrossRef] [PubMed]
13. Caberlotto, E.; Michel, V.; Foucher, I.; Bahloul, A.; Goodyear, R.J.; Pepermans, E.; Michalski, N.; Perfettini, I.; Alegria-Prévot, O.; Chardenoux, S.; et al. Usher Type 1G Protein sans Is a Critical Component of the Tip-Link Complex, a Structure Controlling Actin Polymerization in Stereocilia. *Proc. Natl. Acad. Sci. USA* **2011**, *108*, 5825–5830. [CrossRef] [PubMed]
14. He, Y.; Li, J.; Zhang, M. Myosin VII, USH1C, and ANKS4B or USH1G Together Form Condensed Molecular Assembly via Liquid-Liquid Phase Separation. *Cell Rep.* **2019**, *29*, 974–986.e4. [CrossRef]
15. Yan, J.; Pan, L.; Chen, X.; Wu, L.; Zhang, M. The Structure of the Harmonin/sans Complex Reveals an Unexpected Interaction Mode of the Two Usher Syndrome Proteins. *Proc. Natl. Acad. Sci. USA* **2010**, *107*, 4040–4045. [CrossRef]
16. Li, J.; He, Y.; Lu, Q.; Zhang, M. Mechanistic Basis of Organization of the Harmonin/USH1C-Mediated Brush Border Microvilli Tip-Link Complex. *Dev. Cell* **2016**, *36*, 179–189. [CrossRef]
17. Crawley, S.W.; Weck, M.L.; Grega-Larson, N.E.; Shifrin, D.A.; Tyska, M.J. ANKS4B Is Essential for Intermicrovillar Adhesion Complex Formation. *Dev. Cell* **2016**, *36*, 190–200. [CrossRef] [PubMed]
18. Graves, M.J.; Matoo, S.; Choi, M.S.; Storad, Z.A.; El Sheikh Idris, R.A.; Pickles, B.K.; Acharya, P.; Shinder, P.E.; Arvay, T.O.; Crawley, S.W. A Cryptic Sequence Targets the Adhesion Complex Scaffold ANKS4B to Apical Microvilli to Promote Enterocyte Brush Border Assembly. *J. Biol. Chem.* **2020**, *295*, 12588–12604. [CrossRef]
19. Yang, Y.; Guo, L.; Chen, L.; Gong, B.; Jia, D.; Sun, Q. Nuclear Transport Proteins: Structure, Function, and Disease Relevance. *Signal Transduct. Target. Ther.* **2023**, *8*, 425. [CrossRef]
20. Wing, C.E.; Fung, H.Y.J.; Chook, Y.M. Karyopherin-Mediated Nucleocytoplasmic Transport. *Nat. Rev. Mol. Cell Biol.* **2022**, *23*, 307–328. [CrossRef]
21. Wiemann, S.; Pennacchio, C.; Hu, Y.; Hunter, P.; Harbers, M.; Amiet, A.; Bethel, G.; Busse, M.; Carninci, P.; Diekhans, M.; et al. The ORFeome Collaboration: A Genome-Scale Human ORF-Clone Resource. *Nat. Methods* **2016**, *13*, 191–192. [CrossRef]
22. Koulouras, G.; Panagopoulos, A.; Rapsomaniki, M.A.; Giakoumakis, N.N.; Taraviras, S.; Lygerou, Z. EasyFRAP-Web: A Web-Based Tool for the Analysis of Fluorescence Recovery after Photobleaching Data. *Nucleic Acids Res.* **2018**, *46*, W467–W472. [CrossRef] [PubMed]
23. Schindelin, J.; Rueden, C.T.; Hiner, M.C.; Eliceiri, K.W. The ImageJ Ecosystem: An Open Platform for Biomedical Image Analysis. *Mol. Reprod. Dev.* **2015**, *82*, 518–529. [CrossRef] [PubMed]
24. Ba, A.N.N.; Pogoutse, A.; Provart, N.; Moses, A.M. NLStradamus: A Simple Hidden Markov Model for Nuclear Localization Signal Prediction. *BMC Bioinform.* **2009**, *10*, 202. [CrossRef]
25. Xu, D.; Marquis, K.; Pei, J.; Fu, S.C.; Cağatay, T.; Grishin, N.V.; Chook, Y.M. LocNES: A Computational Tool for Locating Classical NESs in CRM1 Cargo Proteins. *Bioinformatics* **2015**, *31*, 1357–1365. [CrossRef]
26. Stirling, D.R.; Swain-Bowden, M.J.; Lucas, A.M.; Carpenter, A.E.; Cimini, B.A.; Goodman, A. CellProfiler 4: Improvements in Speed, Utility and Usability. *BMC Bioinform.* **2021**, *22*, 433. [CrossRef]
27. Positteam Download RStudio-Posit. Available online: https://posit.co/downloads/ (accessed on 24 July 2023).
28. Alberti, S.; Gladfelter, A.; Mittag, T. Considerations and Challenges in Studying Liquid-Liquid Phase Separation and Biomolecular Condensates. *Cell* **2019**, *176*, 419–434. [CrossRef]
29. Zhou, Y.; Liu, F.; Xu, Q.; Yang, B.; Li, X.; Jiang, S.; Hu, L.; Zhang, X.; Zhu, L.; Li, Q.; et al. Inhibiting Importin 4-Mediated Nuclear Import of CEBPD Enhances Chemosensitivity by Repression of PRKDC-Driven DNA Damage Repair in Cervical Cancer. *Oncogene* **2020**, *39*, 5633–5648. [CrossRef]
30. Levin, A.; Neufeldt, C.J.; Pang, D.; Wilson, K.; Loewen-Dobler, D.; Joyce, M.A.; Wozniak, R.W.; Tyrrell, D.L.J. Functional Characterization of Nuclear Localization and Export Signals in Hepatitis C Virus Proteins and Their Role in the Membranous Web. *PLoS ONE* **2014**, *9*, e114629. [CrossRef]

31. Pemberton, L.F.; Paschal, B.M. Mechanisms of Receptor-Mediated Nuclear Import and Nuclear Export. *Traffic* **2005**, *6*, 187–198. [CrossRef]
32. Shoubridge, C.; Tan, M.; Fullston, T.; Cloosterman, D.; Coman, D.; McGillivray, G.; Mancini, G.; Kleefstra, T.; Gécz, J. Mutations in the Nuclear Localization Sequence of the Aristaless Related Homeobox; Sequestration of Mutant ARX with IPO13 Disrupts Normal Subcellular Distribution of the Transcription Factor and Retards Cell Division. *Pathogenetics* **2010**, *3*, 1. [CrossRef] [PubMed]
33. Jans, D.A.; Martin, A.J.; Wagstaff, K.M. Inhibitors of Nuclear Transport. *Curr. Opin. Cell. Biol.* **2019**, *58*, 50–60. [CrossRef] [PubMed]
34. Adato, A.; Michel, V.; Kikkawa, Y.; Reiners, J.; Alagramam, K.N.; Weil, D.; Yonekawa, H.; Wolfrum, U.; El-Amraoui, A.; Petit, C. Interactions in the Network of Usher Syndrome Type 1 Proteins. *Hum. Mol. Genet.* **2005**, *14*, 347–356. [CrossRef]
35. Ittisoponpisan, S.; Islam, S.A.; Khanna, T.; Alhuzimi, E.; David, A.; Sternberg, M.J.E. Can Predicted Protein 3D Structures Provide Reliable Insights into Whether Missense Variants Are Disease Associated? *J. Mol. Biol.* **2019**, *431*, 2197–2212. [CrossRef] [PubMed]
36. Pennica, C.; Hanna, G.; Islam, S.A.; Sternberg, M.J.E.; David, A. Missense3D-PPI: A Web Resource to Predict the Impact of Missense Variants at Protein Interfaces Using 3D Structural Data. *J. Mol. Biol.* **2023**, *435*, 168060. [CrossRef]
37. Dickmanns, A.; Monecke, T.; Ficner, R. Structural Basis of Targeting the Exportin CRM1 in Cancer. *Cells* **2015**, *4*, 538–568. [CrossRef]
38. Lou, M.; Pang, C.W.M.; Gerken, A.E.; Brock, T.G. Multiple Nuclear Localization Sequences Allow Modulation of 5-Lipoxygenase Nuclear Import. *Traffic* **2004**, *5*, 847–854. [CrossRef]
39. Ferrer, M.; Rodríguez, J.A.; Spierings, E.A.; de Winter, J.P.; Giaccone, G.; Kruyt, F.A.E. Identification of Multiple Nuclear Export Sequences in Fanconi Anemia Group A Protein That Contribute to CRM1-Dependent Nuclear Export. *Hum. Mol. Genet.* **2005**, *14*, 1271–1281. [CrossRef] [PubMed]
40. Smith, K.M.; Di Antonio, V.; Bellucci, L.; Thomas, D.R.; Caporuscio, F.; Ciccarese, F.; Ghassabian, H.; Wagstaff, K.M.; Forwood, J.K.; Jans, D.A.; et al. Contribution of the Residue at Position 4 within Classical Nuclear Localization Signals to Modulating Interaction with Importins and Nuclear Targeting. *Biochim. Biophys. Acta Mol. Cell. Res.* **2018**, *1865*, 1114–1129. [CrossRef]
41. De Ganck, A.; Hubert, T.; Van Impe, K.; Geelen, D.; Vandekerckhove, J.; De Corte, V.; Gettemans, J. A Monopartite Nuclear Localization Sequence Regulates Nuclear Targeting of the Actin Binding Protein Myopodin. *FEBS Lett.* **2005**, *579*, 6673–6680. [CrossRef]
42. Kopp, M.; Rotan, O.; Papadopoulos, C.; Schulze, N.; Meyer, H.; Epple, M. Delivery of the Autofluorescent Protein R-Phycoerythrin by Calcium Phosphate Nanoparticles into Four Different Eukaryotic Cell Lines (HeLa, HEK293T, MG-63, MC3T3): Highly Efficient, but Leading to Endolysosomal Proteolysis in HeLa and MC3T3 Cells. *PLoS ONE* **2017**, *12*, e0178260. [CrossRef]
43. Napolitano, G.; Esposito, A.; Choi, H.; Matarese, M.; Benedetti, V.; Di Malta, C.; Monfregola, J.; Medina, D.L.; Lippincott-Schwartz, J.; Ballabio, A. MTOR-Dependent Phosphorylation Controls TFEB Nuclear Export. *Nat. Commun.* **2018**, *9*, 3312. [CrossRef]
44. Kumagai, A.; Dunphy, W.G. Binding of 14-3-3 Proteins and Nuclear Export Control the Intracellular Localization of the Mitotic Inducer Cdc25. *Genes Dev.* **1999**, *13*, 1067–1072. [CrossRef]
45. Eberhard, D.A.; Karns, L.R.; VandenBerg, S.R.; Creutz, C.E. Control of the Nuclear-Cytoplasmic Partitioning of Annexin II by a Nuclear Export Signal and by P11 Binding. *J. Cell. Sci.* **2001**, *114*, 3155–3166. [CrossRef]
46. Macara, I.G. Transport into and out of the Nucleus. *Microbiol. Mol. Biol. Rev.* **2001**, *65*, 570–594. [CrossRef]
47. Tessier, T.M.; Macneil, K.M.; Mymryk, J.S. Piggybacking on Classical Import and Other Non-Classical Mechanisms of Nuclear Import Appear Highly Prevalent within the Human Proteome. *Biology* **2020**, *9*, 188. [CrossRef]
48. Fung, H.Y.J.; Fu, S.C.; Chook, Y.M. Nuclear Export Receptor CRM1 Recognizes Diverse Conformations in Nuclear Export Signals. *eLife* **2017**, *6*, e23961. [CrossRef]
49. Timney, B.L.; Raveh, B.; Mironska, R.; Trivedi, J.M.; Kim, S.J.; Russel, D.; Wente, S.R.; Sali, A.; Rout, M.P. Simple Rules for Passive Diffusion through the Nuclear Pore Complex. *J. Cell. Biol.* **2016**, *215*, 57–76. [CrossRef]
50. Bourgeois, B.; Hutten, S.; Gottschalk, B.; Hofweber, M.; Richter, G.; Sternat, J.; Abou-Ajram, C.; Göbl, C.; Leitinger, G.; Graier, W.F.; et al. Nonclassical Nuclear Localization Signals Mediate Nuclear Import of CIRBP. *Proc. Natl. Acad. Sci. USA* **2020**, *117*, 8503–8514. [CrossRef] [PubMed]
51. Sakiyama, H.; Wynn, R.M.; Lee, W.R.; Fukasawa, M.; Mizuguchi, H.; Gardner, K.H.; Repa, J.J.; Uyeda, K. Regulation of Nuclear Import/Export of Carbohydrate Response Element-Binding Protein (ChREBP): Interaction of Anα-Helix of ChREBP with the 14-3-3 Proteins and Regulation by Phosphorylation. *J. Biol. Chem.* **2008**, *283*, 24899–24908. [CrossRef] [PubMed]
52. Wang, L.; Liu, X.; Gusev, E.; Wang, C.; Fagotto, F. Regulation of the Phosphorylation and Nuclear Import and Export of β-Catenin by APC and Its Cancer-Related Truncated Form. *J. Cell. Sci.* **2014**, *127*, 1647–1659. [CrossRef] [PubMed]
53. Nardozzi, J.D.; Lott, K.; Cingolani, G. Phosphorylation Meets Nuclear Import: A Review. *Cell. Commun. Signal* **2010**, *8*, 32. [CrossRef] [PubMed]
54. Alberti, S.; Dormann, D. Liquid-Liquid Phase Separation in Disease. *Annu. Rev. Genet.* **2019**, *53*, 171–194. [CrossRef]

55. Alberti, S.; Hyman, A.A. Biomolecular Condensates at the Nexus of Cellular Stress, Protein Aggregation Disease and Ageing. *Nat. Rev. Mol. Cell Biol.* **2021**, *22*, 196–213. [CrossRef]
56. Fokkema, I.F.A.C.; Taschner, P.E.M.; Schaafsma, G.C.P.; Celli, J.; Laros, J.F.J.; den Dunnen, J.T. LOVD v.2.0: The Next Generation in Gene Variant Databases. *Hum. Mutat.* **2011**, *32*, 557–563. [CrossRef]

7 Summary of results

Previous research demonstrated that SANS regulates nuclear splicing through interactions with spliceosome components (Yildirim et al., 2021). This chapter provides an overview of the key findings from publications 1 and 2 (Fritze et al., 2023, 2024). Additionally, it presents new data on the nuclear mobility of PRPF31 and the role of SANS in regulating this process (Chapter 7.3 and 7.4).

7.1 Sequential binding of SANS to spliceosome components is altered by pathogenic variants

In publication 1 (Fritze et al., 2023), we strengthened the evidence that SANS participates in alternative splicing through its interaction with components of the U4/U6.U5 tri-snRNP complex. Using fluorescence resonance energy transfer (FRET) based acceptor bleach assays, we demonstrated that SANS directly interacts with the tri-snRNP proteins PRPF31 and PRPF6. FRET acceptor bleaching was chosen due to its reliability in confirming binary protein interactions within an 8–10 nm spatial range (Karpova et al., 2003; Hevekerl et al., 2011).

Using AlphaFold2-multimer, we pinpointed the binding sites of PRPF31 and PRPF6 to distinct regions of the CENTn domain of SANS, specifically to residues 140–165 and to residues 166–194, respectively. Interestingly, our *in silico* data suggest that a simultaneous binding of SANS to PRPF31 and PRPF6 is unlikely and our *in vitro* FRET data indicate a preference of SANS to PRPF31. By integrating our current findings to previously obtained cryoEM data (Charenton et al., 2019), we hypothesize that SANS binds sequentially to PRPF31 and PRPF6 at two distinct sites within the tri-snRNP complex.

Moreover, our *in silico* predictions point to distinct structural properties of the SANS' CENTn domain, leading to a more refined definition of the structured CENTn1 (aa 128-173) and unstructured CENTn2 (aa 174-243) domains. AlphaFold2 modeling predicted the CENTn1 domain to form a long α-helix. Metapredict and AlphaFold2 consistently predicted the CENTn2 as an intrinsically disordered region (IDR). Furthermore, our AlphaFold2 predictions suggest that the IDR of SANS' CENTn2 forms a newly derived small α-helix upon binding to PRPF6. This structural change is supported by the observation that SANS' CENTn2 represents a highly conserved

Janus sequence, a protein region characterized by its ability to change structure upon binding to different proteins (Das et al., 2015; Wright & Dyson, 2015).

Finally, we identified changes in the interactions of SANS with PRPF31 and PRPF6 when expressing pathogenic variants of SANS. While the pathogenic variant SANS^{S278Pfs*71} was unable to interact with either PRPF31 or PRPF6, SANS^{V132Gfs*3} still interacted with PRPF31, but not PRPF6.

In summary, our data suggest a subsequent binding of SANS to PRPF31 and PRPF6 through two distinct domains of SANS, which is altered in the presence of pathogenic variants. After confirming SANS' role in interacting with spliceosome components and its binding preference for PRPF31, we investigated its transport between cellular compartments to support nuclear functions.

7.2 SANS nuclear export and import sequences dictate subcellular localization

SANS is localized in both the cytoplasm and nucleus, where it contributes to cytoplasmic ciliogenesis and nuclear splicing (Sorusch et al., 2017; Yildirim et al., 2021). Our previous work demonstrated that SANS regulates nuclear splicing by interacting with components such as PRPF31 and PRPF6 (Yildirim et al., 2021; Fritze et al., 2023). Therefore, we asked in the following, how SANS is transferred from the cytoplasm to the nucleus and vice versa to fullfill its function.

In publication 2 (Fritze et al., 2024), we confirmed SANS localization in both the nucleus and cytoplasm using immunofluorescence labeling of endogenous SANS, eYFP-tagged SANS transfection, fluorescence imaging, and cell fractionation assays. SANS' nuclear localization is regulated by an interplay of karyopherin's, namely importins and exportins, which we identified using the previously described nuclear interactome of SANS (Yildirim et al., 2021). Using specific inhibitors, we identified CRM-1/Exportin-1 as the primary nuclear exporter of SANS.

Additionally, we predicted evolutionary conserved nuclear localization sequences (NLSs) and nuclear export sequences (NESs) in SANS' sequence using NLStradamus and LocNES *in silico* tools. We identified two NLSs and three NESs, which we validated in the following through fluorescence imaging of SANS deletion constructs in HeLa and HEK293T cells. While the deletion of NLS_1$^{213-224}$ led to a higher cytoplasmic localization of SANS in HeLa and HEK293T cells, the deletion of NLS_2$^{436-447}$ had only an effect in HEK293T cells but not in HeLa. Additionally, the deletion of SANS

NES_1$^{181\text{-}195}$ or NES_3$^{406\text{-}420}$ led to a significant increase of SANS in the nucleus, indicating that both NESs play a role in the subcellular localization of SANS. By analyzing three pathogenic variants of SANS that lack one or more NLS and NES, we found that these variants are enriched in the nucleus, suggesting a potential alteration in the subcellular localization of SANS in affected patients.

Compared to SANS, its paralogue ANKS4B showed significantly lower nuclear abundance. Initially, the lack of ANKS4B in the nucleus appeared to be due to the absence of NLSs. However, after CRM1/Exportin-1 inhibition, over 80% of ANKS4B was found in the nucleus, highlighting the significant role of ANKS4B's predicted NESs. Additionally, we demonstrated that ANKS4B, unlike SANS, neither co-localizes nor interacts with PRPF31 in the nucleus.

In summary, our data suggest a karyopherin based transport of SANS and ANKS4B into and out of the nucleus, which is dependent on NLSs and NESs. Our findings on the nuclear transport of SANS raised intriguing questions about its functional consequences in the nucleus, particularly its influence on nuclear dynamics such as mobility within Cajal bodies.

7.3 SANS alters the mobility of PRPF31 in Cajal bodies of the nucleus

Previous studies have demonstrated that SANS knockdown alters the nuclear mobility of PRPF31 (Yildirim et al., 2021). In this thesis, I started to strengthen a role of SANS in regulating the mobility of PRPF31 within Cajal bodies.

HeLa cells were co-transfected with eCFP-PRPF31 and the Cajal body marker eGFP-Coilin (Figure 6A). PRPF31s mobility within Cajal bodies was analyzed using fluorescence recovery after photobleaching (FRAP) (Figure 6B). FRAP was chosen for its capability to measure protein mobility in live cells over defined time frames (Cai et al., 2022). The FRAP signal of eCFP-PRPF31 recovered rapidly, with a mobile fraction of ~83%, indicating a fast exchange of PRPF31 within Cajal bodies. This behavior is consistent with other splicing-related proteins, such as coilin, present in Cajal bodies (Sleeman et al., 2003). Co-transfection with eYFP-SANS significantly reduced the mobile fraction of eCFP-PRPF31 to ~38% (Figure 6C), indicating a role for SANS in PRPF31s mobility in Cajal bodies.

We demonstrated in publication 1 that the pathogenic variants SANS^{S278Pfs*71} and SANS^{V132Gfs*3} altered the interaction with PRPF31 (Fritze et al., 2023). Following, I examined whether pathogenic variants affect PRPF31s mobility. Both pathogenic

variants possess frameshift mutations, either in the CENTn1 or in the CENTc domain, which lead to truncated proteins and a premature termination codon (Figure 6D). We co-transfected HeLa cells with eCFP-PRPF31, eGFP-Coilin, and either eYFP-SANS^{V132Gfs*3} (Figure 6E) or eYFP-SANS^{S278Pfs*71} (Figure 6F). The presence of eYFP-SANS^{V132Gfs*3} or eYFP-SANS^{S278Pfs*71} significantly reduced the mobile fraction of eCFP-PRPF31 compared to eYFP-SANS.

Together, these results indicate that SANS regulates PRPF31 mobility within Cajal bodies, a process disrupted by pathogenic variants.

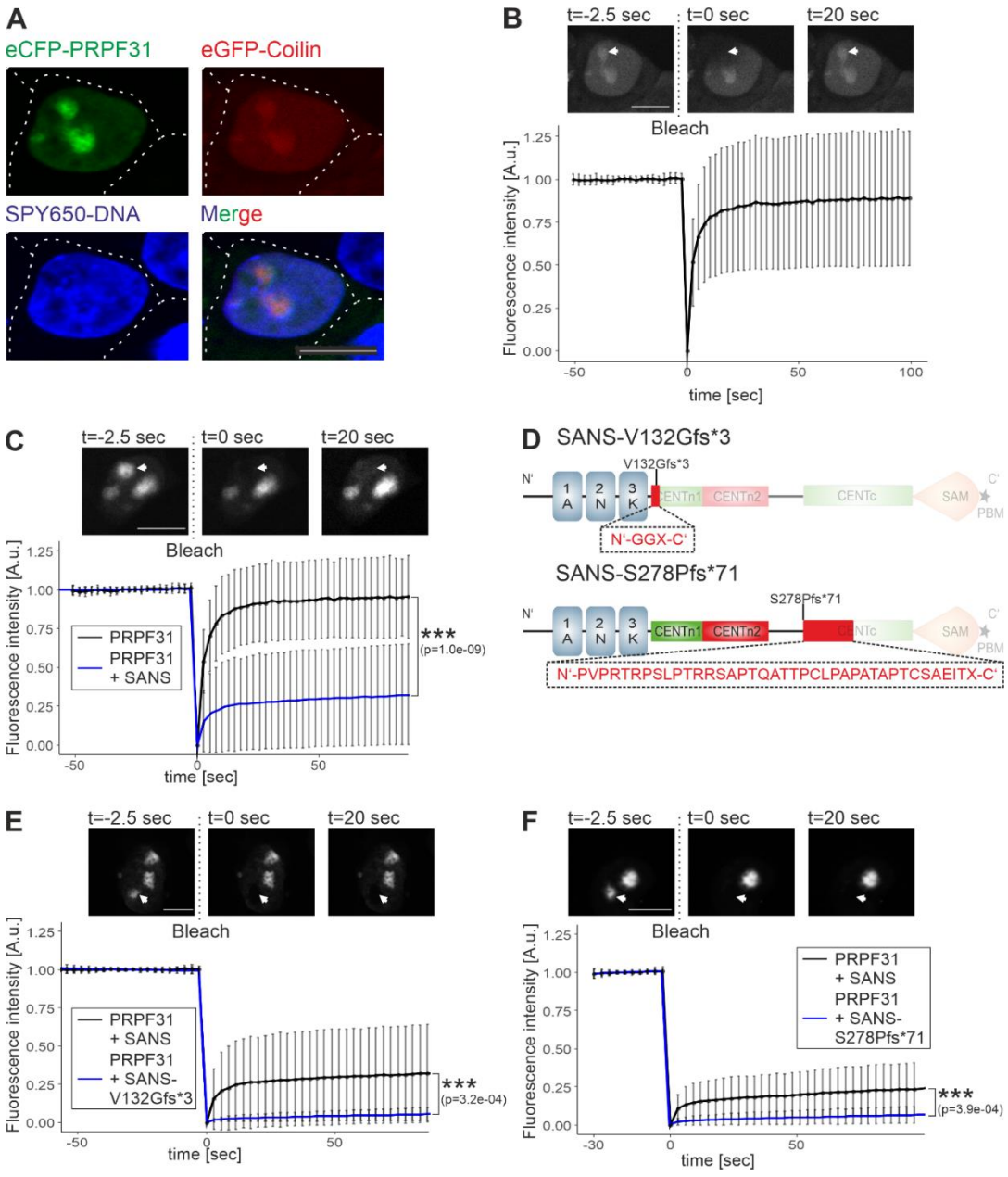

Figure 6. PRPF31's mobility in Cajal bodies in dependence of SANS and pathogenic variants of SANS monitored by FRAP. (A-C, E-F) HeLa cells were transfected with eCFP-PRPF31, eGFP-Coilin and eYFP-SANS or pathogenic variants

of SANS and counterstained with SPY650-DNA. Cajal bodies were bleached with 36% laser intensity. **(A)** eCFP-PRPF31 localized to Cajal bodies labeled by eGFP-Coilin. **(B)** eCFP-PRPF31 recovered with a half-time of 22.5 sec to ~83% of its original intensity. **(C)** eCFP-PRPF31 recovered with a half time of 63 sec to ~38% of its original intensity in eGFP-Coilin positive Cajal bodies in the presence of eYFP-SANS. The mobile fraction of eCFP-PRPF31 was significantly decreased in presence of eYFP-SANS. **(D)** Domain structure of pathogenic variants $SANS^{S278Pfs*71}$ and $SANS^{V132Gfs*3}$. Both, $SANS^{S278Pfs*71}$ and $SANS^{V132Gfs*3}$ are frameshift mutations which lead to a premature termination codon. **(E, F)** The mobile fraction of eCFP-PRPF31 was significantly decreased in the presence of both eYFP-$SANS^{V132Gfs*3}$ or eYFP-$SANS^{S278Pfs*71}$ compared to eYFP-SANS. Normalized fluorescence intensity (A.u.) ± standard deviation is shown over time for ≥ 24 cells in n=3 experiments. Mean of mobile fraction was analyzed with a Welch two-sample t-test. Scale bar 10 µm.

7.4 Assessment of PRPF31 nuclear mobility

Given that PRPF31 is a core component of the U4/U6.U5 tri-snRNP complex, its nuclear mobility can serve as a valuable indicator of tri-snRNP dynamics within nuclear compartments. Building on our previous findings that SANS influences PRPF31' behavior within Cajal bodies (Chapter 7.3), we next aimed to decipher the broader mobility of the tri-snRNP complex, particularly its transfer to nuclear speckles, the final maturation site of this complex.

We used photoactivatable PRPF31 as a marker to observe the nuclear mobility of the tri-snRNP complex (Figure 7). Since PRPF31 stably associates with the tri-snRNP complex, tracking its movement from Cajal bodies to nuclear speckles offers critical insights into the dynamics and timing of tri-snRNP transfer. To ensure specificity, fluorescent PRPF31 was activated in defined nuclear regions, such as Cajal bodies, given its distribution across various compartments. We used the photoactivatable fluorescence protein paGFP, which can be activated by UV light and remains in its activated state for an extended period (Patterson & Lippincott-Schwartz, 2002). The experimental approach involves starting with non-fluorescent PRPF31 protein in living cells. Fluorescence is specifically activated within the Cajal bodies by UV light (Figure 7). The subsequent movement of the PRPF31-containing tri-snRNP complex from the Cajal bodies to nuclear speckles is then monitored using live-cell microscopy (Figure 7).

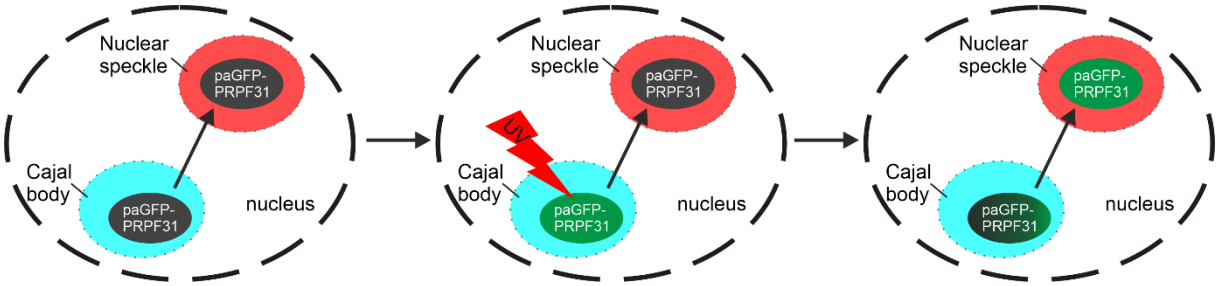

Figure 7. paGFP-PRPF31 schematic approach. Methodical concept of PRPF31s nuclear mobility analysis through activatable fluorescence proteins. paGFP-PRPF31 is located in both Cajal bodies and nuclear speckles, but is specifically activated in Cajal bodies through UV light.

Initially, HeLa cells were transiently transfected with paGFP-PRPF31, eCFP-Coilin as a Cajal body marker (Shpargel et al., 2003), and mCherry-SRRM1 as a nuclear speckle marker (Rai et al., 2018). We analyzed fixed cells with confocal microscopy and activated paGFP-PRPF31 with UV light (Figure 8A). UV activation resulted in increased paGFP fluorescence in Cajal bodies and nuclear speckles, confirming the localization of paGFP-PRPF31 to both compartments (Figure 8B).

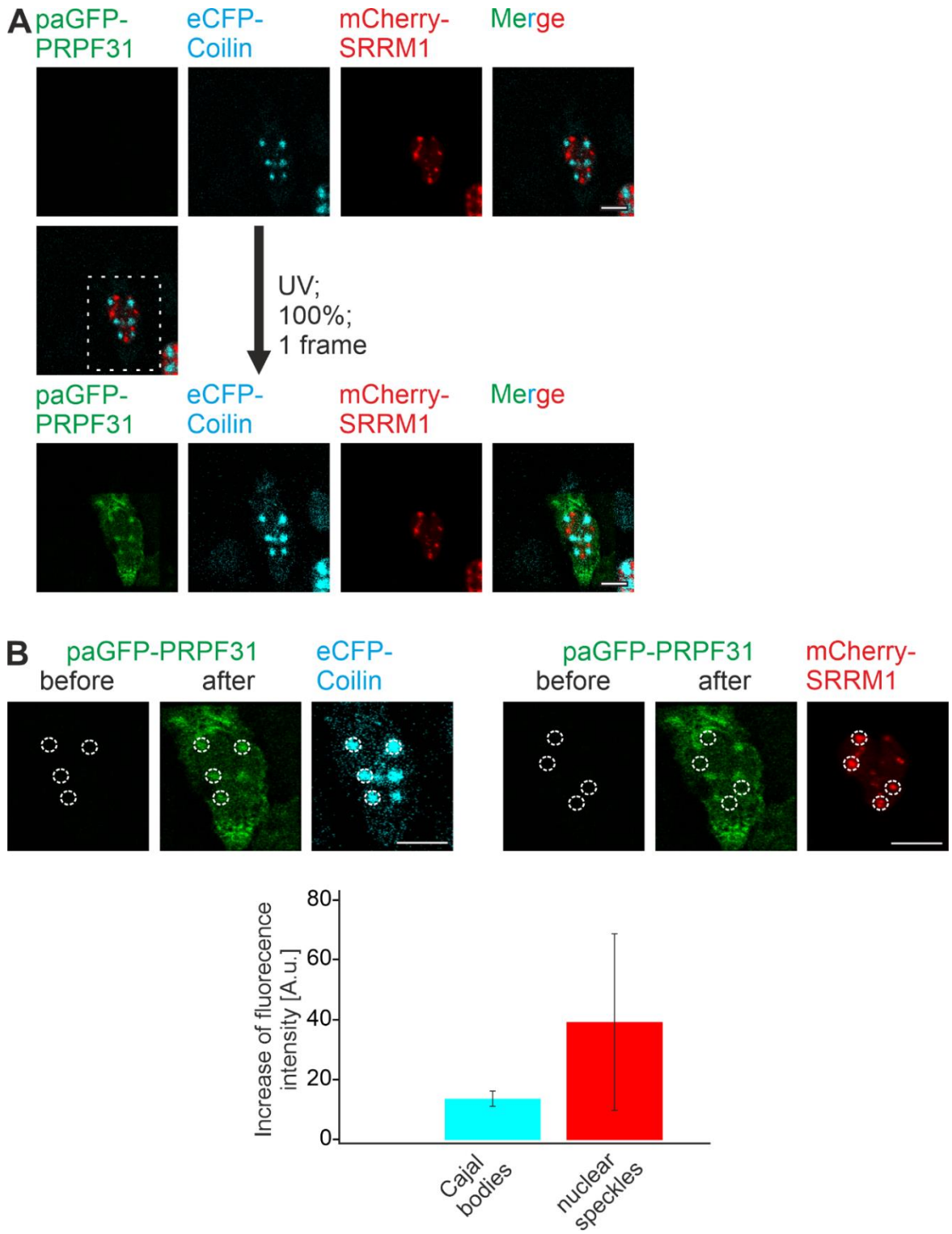

Figure 8. paGFP-PRPF31 is photoactivatable in Cajal bodies and nuclear speckles. (A, B) HeLa cells were co-transfected with paGFP-PRPF31, eCFP-Coilin and mCherry-SRRM1 and counterstained with SPY650-DNA. Region of interest (white box) was photoactivated in fixed cells with 100% laser intensity. **(A)** Photoactivated paGFP-PRPF31 is localized in Cajal bodies and nuclear speckles. **(B)** Quantification of intensity changes of **(A)** in Cajal bodies (left, white circle) or nuclear speckles (right, white circle). One cell out of >40 cells is shown from three independent experiments. Scale bar 10 µm. Data show mean values ± standard deviation from three independent experiments.

We then observed transfected HeLa cells expressing paGFP-PRPF31, eCFP-Coilin, and mCherry-SRRM1 using live-cell fluorescence microscopy (Figure 9). Unfortunately, only ~50% of the observed cells were photoactivatable. Nevertheless, we observed a specific activation of paGFP-PRFP31 within Cajal bodies following UV excitation (Figure 9A, B). Following UV activation, paGFP-PRPF31 fluorescence rapidly declined in activated Cajal bodies (Figure 9B). This is in line with the fast exchange of eCFP-PRPF31 in Cajal bodies shown with FRAP above (Chapter 7.3).

In cells, approximately 200 tri-snRNP complexes containing PRPF31 are formed per minute in each Cajal body (Novotnýa et al., 2011), suggesting a rapid transfer of these complexes from Cajal bodies to nuclear speckles. To rule out prolonged transfer durations, paGFP-PRPF31 nuclear mobility was initially monitored over 30 minutes with images captured every 20 seconds (Figure 9C). We did not observe significant fluorescence changes in the observed time frame (Figure 9C), but small peaks in the first seconds of observation (Figure 9D). Therefore, we hypothesized that the transfer of paGFP-PRPF31 from Cajal bodies to nuclear speckles occurs within seconds. Imaging was subsequently focused on a shorter time frame, with captures taken at one-second intervals (Figure 9E, F). We identified two distinct cell populations: cells in which paGFP-PRPF31 fluorescence increased in nuclear speckles within the first few seconds after activation (Figure 9E), and cells that showed no increase in nuclear speckles (Figure 9F). Both populations were observed with equal frequency and showed no notable differences in the shape, number and fluorescence intensity of their Cajal bodies and nuclear speckles.

In summary, our observations of PRPF31 mobility provide a deeper understanding of the dynamic transfer of the tri-snRNP complex from Cajal bodies to nuclear speckles. Our preliminary data suggest a fast transfer of PRPF31 from Cajal bodies to nuclear speckles but a finetuning of the chosen method is needed to analyze its mobility in more detail.

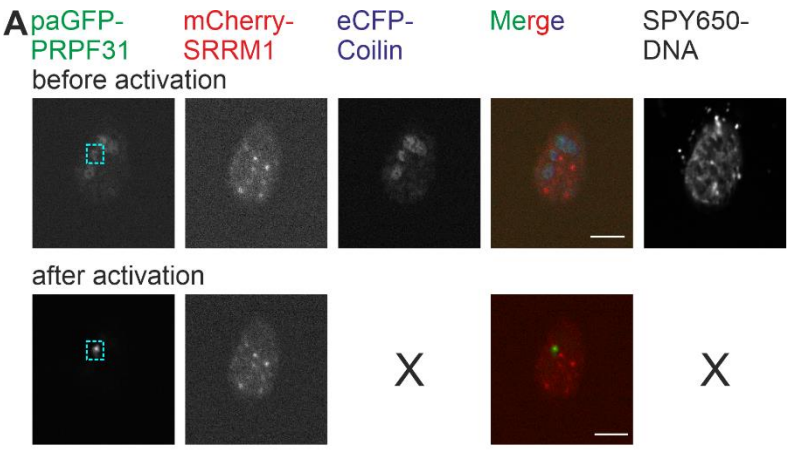
A
paGFP-PRPF31
mCherry-SRRM1
eCFP-Coilin
Merge
SPY650-DNA
before activation
after activation
X
X

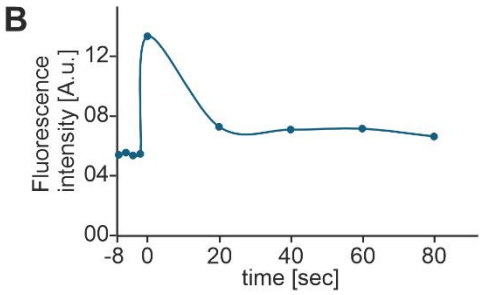
B
Fluorescence intensity [A.u.]
12
08
04
00
-8 0 20 40 60 80
time [sec]

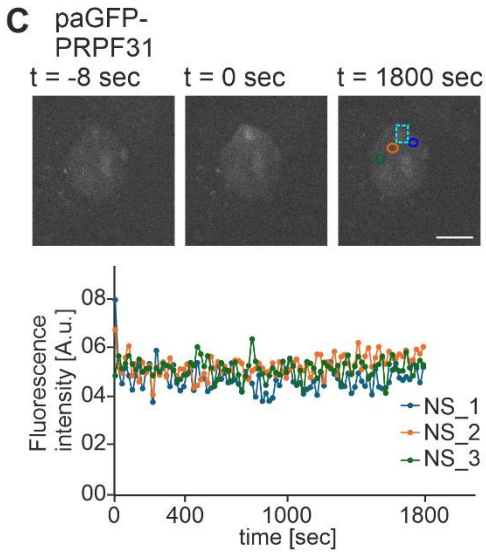
C
paGFP-PRPF31
t = -8 sec
t = 0 sec
t = 1800 sec
Fluorescence intensity [A.u.]
08
06
04
02
00
NS_1
NS_2
NS_3
0 400 1000 1800
time [sec]

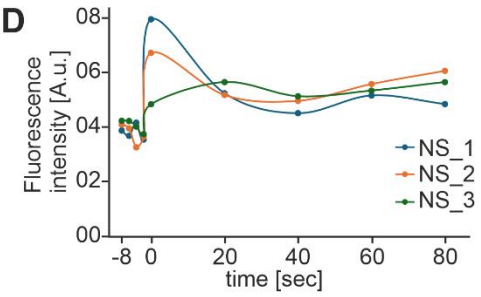
D
Fluorescence intensity [A.u.]
08
06
04
02
00
NS_1
NS_2
NS_3
-8 0 20 40 60 80
time [sec]

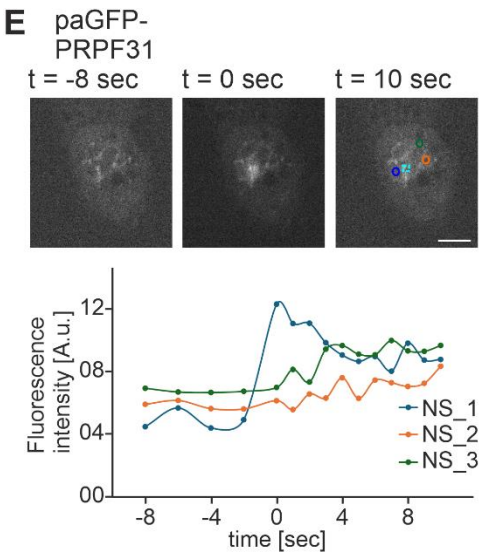
E
paGFP-PRPF31
t = -8 sec
t = 0 sec
t = 10 sec
Fluorescence intensity [A.u.]
12
08
04
00
NS_1
NS_2
NS_3
-8 -4 0 4 8
time [sec]

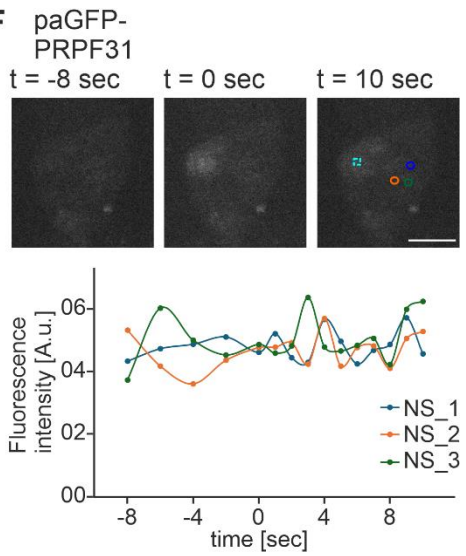
F
paGFP-PRPF31
t = -8 sec
t = 0 sec
t = 10 sec
Fluorescence intensity [A.u.]
06
04
02
00
NS_1
NS_2
NS_3
-8 -4 0 4 8
time [sec]

Figure 9. paGFP-PRPF31 nuclear mobility observed in live cell microscopy. (A-F) HeLa cells were co-transfected with paGFP-PRPF31, mCherry-SRRM1 (nuclear speckles) and eCFP-Coilin (Cajal bodies) and counterstained with SPY650-DNA. paGFP was activated at time point 0 with 10% laser intensity (cyan box). eCFP-Coilin and SPY650-DNA were only observed for the first time point. **(A)** Representative images of live cell activation of paGFP-PRPF31. **(B)** Fluorescence of paGFP-PRPF31 over time for one representative Cajal body. **(C)** Nearly no fluorescence intensity changes for three nuclear speckles (NS) over a timeframe of 30 min were observed. **(D)** Zoom in of **(C)**. A small fluorescence increase after photoactivation was observed for all three NS within the first seconds. **(E)** Representative cell showing that paGFP-PRPF31 transfers to NS. Fluorescence intensity increased for three NS over a timeframe of few seconds. **(F)** Representative cell for paGFP-PRPF31 not transferred to NS. No fluorescence intensity increase for three NS over a timeframe of few seconds was observed. Representative cells were analyzed in timesteps of 20 sec **(A-D)** or 1 sec **(E-F)**. NS of interest are indicated with colored circles. Normalized fluorescence intensity (A.u.) is shown over time. One cell out of >40 measured cells from one independent experiment is shown in each subfigure. Scale bar 10 µm.

8 General Discussion

Publication 1 (Fritze et al., 2023) and publication 2 (Fritze et al., 2024) include a detailed discussion of the main findings. This chapter elaborates on selected sections of the publications, explores the additional data presented in Chapter 7, and offers a broader perspective on the key findings.

8.1 The nuclear import of SANS

SANS was initially believed to be uniquely cytoplasmic located (Weil et al., 2003). In the cytoplasm, SANS fulfills roles in intracellular transport, endocytosis, and primary ciliogenesis (Maerker et al., 2008; Overlack et al., 2011; Bauss et al., 2014; Sorusch et al., 2019). However, recent findings from our lab suggest that SANS also localizes to the nucleus (Sorusch et al., 2017; Yildirim et al., 2021). Moreover, SANS regulates nuclear splicing and therefore has to enter the nucleus (Yildirim et al., 2021). We demonstrate that SANS is actively transported into the nucleus and identify two NLSs critical for its nuclear import (Fritze et al., 2024).

The two identified NLSs in SANS are NLS_1$^{213\text{-}224}$ and NLS_2$^{436\text{-}447}$ (Fritze et al., 2024). The deletion of NLS_2$^{436\text{-}447}$ had less effect on SANS' localization compared to the deletion of NLS_1$^{213\text{-}224}$. Proteins can contain both strong and weak NLSs (Mears et al., 1995). Thus, we hypothesize that NLS_1$^{213\text{-}224}$ is a strong NLS while NLS_2$^{436\text{-}447}$ is a weak NLS of SANS. The partial nuclear localization of SANS despite mutation of NLS_1$^{213\text{-}224}$ suggests that additional mechanisms contribute to its nuclear import, as detailed in publication 2 (Fritze et al., 2024).

Nonetheless, we identified an NLS-dependent pathway for SANS nuclear import (Fritze et al., 2024). This observation aligns with the finding that these NLSs play a critical role in nuclear import and underscores the essential role of SANS within the nucleus (Wing et al., 2022). The discovery of SANS' NLSs underscores its functional necessity in the nucleus, enabling critical interactions with PRPF31 and PRPF6, as detailed in the subsequent section.

8.2 SANS interacts through two different protein regions with the tri-snRNP proteins PRPF31 and PRPF6

Since we showed that SANS is able to enter the nucleus, we decided to deciphered its nuclear functions in more detail. We provide evidence of SANS' interactions with

PRPF31 and PRPF6 and further elucidates their respective interaction platforms. It shows, that PRPF31 and SANS interact through a long α-helix in SANS' CENTn domain, which we named CENTn1 (Fritze et al., 2023). The predicted binding of PRPF31 via its NOP domain to the helical structure of SANS' CENTn1 is consistent with the typical interaction mode of NOP domains (Tancredi et al., 2005; Charenton et al., 2019).

However, the functional significance of SANS-PRPF31 interaction remains unclear. A possibility is that SANS' interaction to PRPF31 reduces the mobility of PRPF31 in Cajal bodies, which is in line with the preliminary data presented in this thesis (Chapter 7.3). This interaction may enhance the recruitment of PRPF31 to Cajal bodies and thereby fine-tune the assembly of the tri-snRNP, similar to the role of other Cajal body components such as Coilin (Toyota et al., 2010). This recruitment is consistent with the role of protein-protein interactions in gathering client proteins within membraneless organelles, to enhance the respective protein concentration (Song et al., 2020). To further confirm a role of SANS for PRPF31s mobility in Cajal bodies, a reciprocal experiment could be conducted by knocking down endogenous SANS.

Regarding PRPF6's interaction with SANS, we confirmed that its C-terminal HAT domains bind to SANS, consistent with previous reports (Yildirim et al., 2021; Fritze et al., 2023). These domains bind to seven amino acids of the α-helix of SANS' CENTn1, but mainly to a region of SANS' CENTn2 (Fritze et al., 2023). The function of the interaction between PRPF6 and SANS remains elusive in the given study but may be related to the mobility of PRPF6 in Cajal bodies, as discussed above for PRPF31. However, since SANS' knockdown did not affect U5-snRNP-specific proteins, which include PRPF6, it is more likely that the SANS-PRPF6 interaction plays a role in other nuclear functions, such as U5-snRNP complex recycling (Makarov et al., 2000; Yildirim et al., 2021).

The findings presented here, detail SANS' interactions with splicing proteins and characterize the highly flexible CENTn2 domain. Therefore, they provide valuable insights into SANS' cellular functions. Nevertheless, SANS functions in both the nucleus and the cytoplasm (Maerker et al., 2008; Overlack et al., 2011; Bauss et al., 2014; Sorusch et al., 2019; Yildirim et al., 2021; Fritze et al., 2023). Therefore, it is likely that SANS is actively exported from the nucleus.

8.3 SANS NESs induce SANS nuclear export

SANS cellular localization may be regulated through two possible mechanisms. Either SANS' NLSs are actively modulated in the cytoplasm to regulate its nuclear-cytoplasmic distribution. Alternatively, SANS must possess NESs that are essential for its active nuclear export.

We identified two NESs, and deletion of both resulted in nearly complete nuclear localization of SANS (Fritze et al., 2024). Notably, deletion of a single NES still led to almost complete nuclear localization of SANS. This indicates that both NESs are simultaneously required for efficient protein export. Proteins with two or more functional NESs exhibit similar effects, as the deletion of a single NES results in complete nuclear localization (Ferrer et al., 2005; Ossovskaya et al., 2008). This indicates a cooperative function among these NESs. However, simultaneous binding of CRM1/Exportin-1 to two NESs within a single protein, or the requirement for multiple CRM1 molecules binding to one cargo, has not been described to date.

The identification of NESs complements the understanding of SANS' nuclear import via NLSs, emphasizing a tightly regulated bidirectional transport mechanism essential for its dual nuclear-cytoplasmic roles.

8.4 SANS is a ciliary and nuclear protein

We reinforce the observation that SANS is a protein capable of entering the nucleus (Fritze et al., 2024). However, initially SANS was believed to be a cytoplasmic protein (Weil et al., 2003). Thus, the precise timing and location of SANS localization within human cells remain unresolved.

Since SANS functions in both the nucleus and cytoplasm, its localization requires tight regulation. We have not identified such a regulation mechanism yet. But a common mechanism for this is the regulation of the function of NLSs and NESs via posttranslational modifications, such as phosphorylation (Sakiyama et al., 2008; Wang et al., 2014; Napolitano et al., 2018). Additionally, the binding of SANS' interaction partners could compete with exportin and importin binding, thereby modulating its subcellular localization. For instance, PRPF6 binds to a region in SANS (aa 166-194) including NES_1$^{181\text{-}195}$ (Fritze et al., 2023, 2024), which makes a simultaneous binding of CRM1 and PRPF6 unlikely and could lead to SANS abundance in the nucleus. Therefore, the regulation of SANS' NLSs/NESs should be elucidated in detail in the future.

The intricate regulation of SANS localization highlights its unique functional duality between the nucleus and the cytoplasm. Interestingly, this characteristic is not observed for its paralogue ANKS4B as discussed in the following section.

8.5 SANS paralogue ANKS4B differs in its cellular localization

In comparison to SANS, its paralogue ANSK4B was less abundant in the nucleus (Fritze et al., 2024), being in line with the fact that there is no known function of ANKS4B in the nucleus (Crawley et al., 2016; He et al., 2019). Therefore, SANS and ANKS4B differ in their cellular localization although they are paralogues. Such spatial differences are rarely observed among other paralogues (Kim et al., 2009) and are likely due to huge differences in the CENT domains of SANS and ANKS4B (Fritze et al., 2024). This is consistent with the distinct binding partners of SANS and ANKS4B in these protein domains, including Myosin-IIVA, Myosin-IIVB, and PRPF31 (Adato et al., 2005b; Crawley et al., 2016; Fritze et al., 2024). Interestingly, both CENT domains are predicted by AlphaFold2 as highly disordered (https://alphafold.ebi.ac.uk/; accessed 06th of August 2024 (Jumper et al., 2021)). Although we found, that SANS is highly conserved, its CENT domain is less conserved compared to its N- and C-terminal regions (Fritze et al., 2023), which is in line with the common assumption that IDRs are more accessible to evolutionary mutations (Ahrens et al., 2017). Thus, it is likely that the paralogues ANKS4B and SANS share a common protein ancestor, comprising folded domains in the N- and C-terminal regions, which evolved over time into two paralogues with less conserved CENT domains. This is in line with other protein paralogues, which possess a high similarity in their structured regions but differ in their IDRs (Chiu et al., 2022).

The distinct cellular localization and structural differences between SANS and its paralogue ANKS4B underscore SANS' unique roles in cellular function. These distinctions are particularly significant in the context of pathogenic SANS variants, where altered localization and impaired interactions directly contribute to disease mechanisms.

8.6 Pathogenic variants of SANS show altered function and localization in the cell

To date, more than 70 pathogenic variants in USH1G/SANS have been identified in USH1G patients (www.LOVD.nl/USH1G, accessed on 06th January 2025 (Fokkema et

al., 2011)). However, the molecular mechanisms underlying USH caused by these defects remain poorly understood. We provide evidence that pathogenic variants of SANS show altered interactions with the tri-snRNP proteins PRPF31 and PRPF6 and are mislocalized within the cell (Fritze et al., 2023, 2024). The altered interaction of SANS to its binding proteins has direct impact on its function and could therefore result in impaired alternative splicing events of other proteins as observed before (Yildirim et al., 2021). Additionally, mislocalization of SANS likely affects its cellular function, as seen in other diseases (Ederle & Dormann, 2017). The mislocalization of pathogenic SANS variants provides compelling evidence of the critical role that precise regulation of NLS and NES is necessary in maintaining cellular function, as outlined above.

Since the pathogenic variants of SANS observed in this thesis are targeted into the nucleus (Fritze et al., 2024), they may not fulfill their functions in the cytoplasm. Moreover, despite their nuclear localization, these truncated variants are unlikely to function properly in splicing regulation (Yildirim et al., 2021). This may result in the accumulation of truncated proteins in the nucleus, which could be additionally harmful.

In addition, the two pathogenic variants SANS^{V132Gfs*3} and SANS^{S278Pfs*71} caused a significant reduction in PRPF31 mobility within Cajal bodies (Chapter 7.3). It is possible that these pathogenic variants of SANS hinder the assembly of the tri-snRNP complex, which results in a slower mobility of PRPF31 in the Cajal bodies due to a prolonged process. Alternatively, the accumulation of pathogenic SANS variants could cause nuclear aggregation, initiating a chain reaction that leads to the aggregation of splicing proteins, as observed in other diseases like Alzheimer's disease (Guo et al., 2021). To explore this further, the mobility of SANS' pathogenic variants in live cells could be monitored in the nucleus, for example by using FRAP. Combined with the data provided in this thesis, mobility data of SANS' pathogenic variants could contribute to a deeper understanding of the USH1G disease.

8.7 SANS a multifunctional protein with moonlight functions

The specific timing and location of SANS' cellular functions remain unclear in this study. SANS localization may vary in a cell type-specific manner. In humans, SANS is expressed in both the retina and the inner ear (Weil et al., 2003). In the inner ear, SANS is primarily associated with the stereociliary morphology of hair cells (Caberlotto et al., 2011; Miyasaka et al., 2016). In the retina SANS also localizes and functions at cytoplasmic compartments such as the connecting cilium of photoreceptor cells

(Overlack et al., 2011; Bauss et al., 2014; Sorusch et al., 2019). Additionally, SANS has been detected in the nuclei of retinal cells, including the outer nuclear layer and retinal neurons (Sorusch et al., 2017; Yildirim et al., 2021). These findings suggest that SANS' nuclear export and import pathways, shown in this thesis, as well as its nuclear functions may be unique to retinal cells.

Moreover, within the cell, SANS performs multiple roles, including ciliary trafficking and nuclear splicing (Sorusch et al., 2019; Yildirim et al., 2021). In this thesis, we strengthened the observation that SANS participates in splicing through its interactions with proteins in the tri-snRNP complex (Fritze et al., 2023). Additionally, we demonstrate that SANS is actively transported out of the nucleus, allowing it to perform functions in the cytoplasm (Fritze et al., 2024). Proteins with such multifunctional capabilities are classified as moonlight proteins (Singh & Bhalla, 2020). Moonlight proteins perform diverse cellular functions, regulated by subcellular localization, cell-specific expression, posttranslational modifications, and binding interactions. All four regulatory mechanisms have been observed for SANS (Bauss et al., 2014; Sorusch et al., 2019; Cowan et al., 2020; Fritze et al., 2023, 2024). Thus, SANS is likely involved in distinct cellular pathways at different spatiotemporal stages. One pathway, which is of high importance is SANS function in the tri-snRNP complex maturation and nuclear transfer. In this study, I present a preliminary method for observing this function, discussed below.

8.8 PRPF31s nuclear mobility is observable via live cell imaging microscopy

The assembly of the U4/U6.U5 tri-snRNP complex takes place in Cajal bodies within seconds, followed by the transfer of the tri-snRNP complex from Cajal bodies to the nuclear speckles (Sleeman & Lamond, 1999; Novotnýa et al., 2011). Together with PRPF6, PRPF31 is the key assembly protein for the U4/U6.U5 tri-snRNP complex and its deletion results in retention of the tri-snRNP complex in Cajal bodies (Makarova et al., 2002; Schaffert et al., 2004). Interestingly, previous data from our group suggest additional retention of the tri-snRNP complex in Cajal bodies following SANS knockdown (Yildirim et al., 2021). However, the precise time frame of the tri-snRNP complex transfer, the mechanisms and the proteins involved remain unclear. Therefore, we aimed to establish a method to observe the transfer of the tri-snRNP complex in living cells, which is based on a photoactivatable protein called paGFP

(Chapter 7.4). Photoactivatable proteins are widely used, primarily to observe cell migration in tissues or organisms, or for tracking translocation of proteins between cellular compartments (Francis et al., 2020; Gwon et al., 2021; Tomura et al., 2021).

We provide preliminary evidence that the photoactivatable construct paGFP-PRPF31 is located to both Cajal bodies and nuclear speckles and transfers between the two compartments (Chapter 7.4). Unfortunately, we encountered three major problems during our experiments: 1. Not all Cajal bodies are photoactivatable by our method; 2. paGFP-PRPF31 transfer occurs in a very short time frame and 3. paGFP-PRPF31 does not transfer from Cajal bodies to nuclear speckles in every cell.

Regarding problem one, there are two possible reasons for an absence of photoactivation of paGFP-PRPF31 in Cajal bodies: Either the used microscope settings are not sufficient, or the transiently transfection of cells only worked for the Cajal body marker eCFP-Coilin, but not for paGFP-PRPF31. Since we generally observed the possibility of photoactivation of paGFP-PRPF31 in living cells with our technical setup, it is more likely that the lack of fluorescence of paGFP-PRPF31 is due to a lack of transfection. Thus, generating stably transfected cells or observing endogenous PRPF31 should be primary objectives for future studies on PRPF31 nuclear transfer. A technique, which could be promising is CRISPaint a CRISPR-Cas9 based method to insert fluorescence proteins specifically to the endogenous open reading frame of a target gene (Schmid-Burgk et al., 2016).

In concern of problem two, the rapid nuclear transfer of paGFP-PRPF31 may result in the loss of critical time points. For our studies, we used a Nikon Yokogawa spinning disc microscope with a single camera mode (https://www.microscope.healthcare.nikon.com/products/confocal-microscopes/csu-series/csu-w1; accessed on 25th September 2024), which may be to slow to observe paGFP-PRPF31 nuclear transfer with a 1 second image acquiring interval. Therefore, the used setting could either be improved with a dual camera detection mode or by switching to an alternative microscope with a faster acquisition mode.

Finally, regarding problem three, after activation of paGFP-PRPF31, we observed two distinct cell populations: one, which showed fluorescence increase in nuclear speckles within seconds, and another one, where no increase was detected. The reason for this remains unclear but could result from a loss of signal due to cell specificities. Additionally, a preference for the assembly of the tri-snRNP for endogenous PRPF31 without paGFP tag could result in a missing fluorescence

increase after activation. As mentioned above, stable transfected cells or the observation of endogenous PRPF31 would be beneficial for a more robust data acquisition. In addition, it should be tested whether paGFP-PRPF31 is included in the tri-snRNP complex e.g. through pull-down of paGFP-PRPF31 and detection of tri-snRNP protein members such as PRPF6.

9 Outlook

With this thesis, I provide further insight in the molecular functions of the *USH1G* derived protein SANS. It focuses on the interactions between SANS and the tri-snRNP proteins PRPF31 and PRPF6, utilizing *in vitro* and *in silico* techniques. Furthermore, I provide insight in SANS' nuclear-cytoplasmic shuttling as well as its differential localization to ANSK4B. Finally, it elucidates, on how pathogenic variants alter SANS' function in the cell through altered protein-protein binding and cellular localization.

Together with the previous work of our group (Yildirim et al., 2021), this thesis strengthens the observation that SANS' functions as a splicing regulator in the nucleus. However, to better understand the role of SANS, a more precise evaluation of its involvement in the different stages of splicing is required. A key objective would be to determine SANS' localization within the tri-snRNP complex and the assembled spliceosome using structural experiments. Here, AlphaFold3, an updated version of AlphaFold, which is capable of predicting protein-nucleic acid interactions, could be useful (Abramson et al., 2024). However, predictions from AlphaFold currently provide limited insights and should be validated with experimental techniques such as cryo-electron microscopy (cryo-EM) or nuclear magnetic resonance (NMR) spectroscopy. Additionally, a broader analysis of SANS' target genes during alternative splicing would be valuable, as it could reveal connections to SANS-dependent cellular functions.

Furthermore, a deeper understanding of SANS' regulation within the cell is needed. This is particularly relevant for understanding the conformational changes that occur upon binding to the CENTn2 domain. Here multiple binding partners of SANS' CENT domain could be visualized together with SANS through NMR spectroscopy to understand the conformational changes of SANS' CENTn2 in detail (Schneider et al., 2019; Dyson & Wright, 2021). Deciphering SANS' post-translational modifications would also be highly beneficial, as these likely influence SANS' protein-protein interactions and cellular localization.

In contrast to SANS, less is known about the function of its paralogue ANSK4B. A good approach would be to get a detailed protein interactome of ANKS4B, as it was previously done for SANS (see Chapter 4.2). *In silico* tools like AlphaFoldPulldown could be useful here, as they allow filtering for potential interaction partners of ANKS4B before conducting wet lab experiments (Yu et al., 2023). Additionally, the role of ANKS4B in the human body should be tackled in more detail, as it has not been linked to any disease yet. This could clarify whether the loss of ANKS4B due to a mutation is

lethal in patients or whether its deficiency only has mild effects, making it clinically undetected.

Moreover, SANS has effects on splicing but is mainly expressed in two sensory tissues of humans, the inner ear and the retina (Weil et al., 2003; Yildirim et al., 2021). Unfortunately, Sans deficient mice only show a hearing and vestibular impairment and not an impairment of sight (Kikkawa et al., 2003). The lack of an adequate model organism is one reason why the role of SANS in the human body is not yet fully understood. In this context, analysis of induced pluripotent stem cell derived models such as retinal organoids could be highly valuable for elucidating SANS' functional role in greater detail (Bell et al., 2020). This methodical approach would enable the direct observation of splicing alterations and changes in protein localization within an artificial retina system. Finally, these models offer promising options for testing treatments to cure or mitigate USH1G disease (Ashworth et al., 2024).

10 Summary

In my thesis I investigated the molecular mechanisms underlying Human Usher syndrome (USH), particularly focusing on the protein USH1G/SANS. Usher syndrome, a clinically and genetically heterogeneous disorder that leads to hearing and vision loss. The *USH1G* gene encodes the scaffold protein SANS, which is highly expressed in the eye and ear. Recently, SANS has also been found in the cell nucleus, where it participates in the regulation of pre-mRNA splicing.

In my thesis I aimed to elucidate the interactions of SANS with splicing-related proteins PRPF31 and PRPF6, as well as the mechanism of SANS' nuclear-cytoplasmic shuttling. Additionally, I established a method to monitor the nuclear transfer of PRPF31 by live cell imaging.

I show that SANS interacts with PRPF31 and PRPF6 at specific sites within its CENTn domain. Using FRET-based interaction assays and AlphaFold2, we identified for PRPF31 and PRPF6 specific binding sites in the CENTn domain of SANS, namely binding to the structured CENTn1 and to the unstructured CENTn2, respectively. In addition, we found evidence for sequential binding of PRPF31 and PRPF6 to the SANS molecule, which might be crucial for role of SANS in splicing processes in the nucleus.

To fulfill its nuclear functions, SANS needs to be transported into the nucleus. In my thesis I identified two nuclear localization sequences (NLSs) and two nuclear export sequences (NESs). I highlighted their critical roles in SANS subcellular localization and in nuclear–cytoplasmic shuttling. Comparative analysis with SANS' paralogue ANKS4B revealed distinct localization patterns, with ANKS4B more confined to the cytoplasm due to a lack of NLS.

Using pathogenic variants of *USH1G*/SANS, we demonstrated altered interactions with the splicing proteins PRPF31 and PRPF6. Additionally, these pathogenic variants displayed subcellular mislocalization, likely impacting SANS' function in splicing regulation and in the development of USH.

Further, I provide data on the nuclear mobility of photoactivatable fluorescence-tagged PRPF31 and the rapid transfer of splicing components between nuclear compartments. With these results, I could lay the groundwork for future studies on SANS-dependent molecular dynamics.

Collectively, I enlighten the role of SANS in the nucleus. My findings advance the understanding of the molecular functions of SANS and its broader implications for USH1G pathogenesis.

11 Zusammenfassung

In meiner Dissertation untersuchte ich die molekularen Mechanismen, die dem menschlichen Usher-Syndrom (USH) zugrunde liegen, wobei ich mich insbesondere auf das Protein USH1G/SANS konzentrierte. Das Usher-Syndrom ist eine klinisch und genetisch heterogene Störung, die zu Hör- und Sehverlust führt. Das *USH1G* Gen kodiert für das Gerüstprotein SANS, das im Auge und im Ohr stark ausgeprägt ist. Kürzlich wurde SANS auch im Zellkern gefunden, wo es an der Regulierung des prä-mRNA-Spleißens beteiligt ist.

In meiner Dissertation wollte ich die Wechselwirkungen von SANS mit den Proteinen PRPF31 und PRPF6, die mit dem Spleißen zusammenhängen, sowie den Mechanismus des Shuttlings von SANS zwischen Kern und Zytoplasma aufklären. Darüber hinaus habe ich eine Methode entwickelt, um den Kerntransfer von PRPF31 durch Bildgebung in lebenden Zellen zu überwachen.

Ich zeige, dass SANS mit PRPF31 und PRPF6 an spezifischen Stellen innerhalb seiner CENTn-Domäne interagiert. Mithilfe von FRET-basierten Interaktionsassays und AlphaFold2 haben wir für PRPF31 und PRPF6 spezifische Bindungsstellen in der CENTn-Domäne von SANS identifiziert, nämlich die Bindung an das strukturierte CENTn1 bzw. an das unstrukturierte CENTn2. Darüber hinaus fanden wir Hinweise auf eine sequenzielle Bindung von PRPF31 und PRPF6 an das SANS-Molekül, was für die Rolle von SANS bei Spleißprozessen im Zellkern entscheidend sein könnte.

Damit SANS seine Kernfunktionen erfüllen kann, muss es in den Zellkern transportiert werden. In meiner Dissertation habe ich zwei Kernlokalisierungssequenzen (NLS) und zwei Kernexportsequenzen (NES) identifiziert. Ich habe ihre kritische Rolle bei der subzellulären Lokalisierung von SANS und beim Nukleus-Zytoplasma-Shuttling herausgestellt. Eine vergleichende Analyse mit dem SANS-Paralogon ANKS4B ergab unterschiedliche Lokalisierungsmuster, wobei ANKS4B aufgrund fehlender NLS stärker auf das Zytoplasma beschränkt ist.

Mit pathogenen Varianten von *USH1G*/SANS konnten wir veränderte Interaktionen mit den Spleißproteinen PRPF31 und PRPF6 nachweisen. Darüber hinaus wiesen diese pathogenen Varianten eine subzelluläre Fehllokalisierung auf, die sich wahrscheinlich auf die Funktion von SANS bei der Spleißregulation und bei der Entwicklung von USH auswirkt.

Des Weiteren habe ich Daten zur Kernmobilität von photoaktivierbarem, fluoreszenzmarkiertem PRPF31 und zum schnellen Transfer von Spleißkomponenten

zwischen Kernkompartimenten vorgelegt. Mit diesen Ergebnissen konnte ich den Grundstein für künftige Studien zur SANS-abhängigen Molekulardynamik legen.

Insgesamt erkläre ich die Rolle von SANS im Zellkern. Meine Ergebnisse tragen zum besseren Verständnis der molekularen Funktionen von SANS und ihrer breiteren Bedeutung für die Pathogenese von USH1G bei.

12 Appendix

12.1 Materials and methods for Chapter 7.3 and Chapter 7.4

12.1.1 Materials:

DNA constructs

DNA construct	Reference
eYFP-SANS	(Fritze et al., 2023)
eYFP-SANS^{S278Pfs*71}	(Fritze et al., 2023)
eYFP-SANS^{V132Gfs*3}	(Fritze et al., 2023)
eCFP-PRPF31	(Fritze et al., 2023)
eGFP-Coilin	Kindly provided by Greg Matera (Addgene #36906)
eCFP-Coilin	This work
paGFP-PRPF31	This work
mCherry-SRRM1	Kindly provided by Lucas Pelkmans (Rai et al., 2018)

12.1.2 Methods:

Cloning

Open reading frames of PRPF31 and Coilin were obtained from template plasmids (Addgene #36906) (Fritze et al., 2023) and cloned into pENTR™, as described by the manufacturer (ThermoFisher, Karlsruhe, Germany, #K240020). Gateway™ LR reaction into the appropriate destination vector was performed according to the manufacturer's protocol (Thermo Fisher, #11791020).

Cell lines and culture

Dulbecco's modified Eagle's medium (DMEM) (ThermoFisher, Karlsruhe, Germany, #31966021) containing 10% heat-inactivated fetal calf serum (FCS) (Cytiva, Freiburg, Germany, #SV30160.03) was used to culture HeLa cells (kindly provided by AG Doorman, IMP).

Fluorescence recovery after photobleaching (FRAP)

HeLa cells were seeded in Ibidi 4 well plate (Ibidi, Gräfelfing, Germany, #80426) with a density of 40.000 cells/well. Cells were transfected with Lipofectamine™ LTX as described by the manufacturer (ThermoFisher, Karlsruhe, Germany, #15338100). Cells were observed with a Nikon Yokogawa spinning disc microscope with a 60x water objective under 37°C. FRAP was performed with a 445 nm laser at 36% laser intensity for 100 iterations. Recovery was observed every 3 sec for up to 4 min. Quantification was performed with Fiji and EasyFRAP-web (Koulouras et al., 2018). Data are presented as Full-Scale Normalization and T-half was calculated with Double curve fitting.

Fluorescence activation in fixed cell

HeLa cells were seeded in 6 well plates with a density of 250.000 cells/well. Cells were transfected with LipofectamineTM LTX as described by the manufacturer (ThermoFisher, Karlsruhe, Germany, #15338100). Fixed HeLa cells were analyzed with a Leica TCS SP8 and activation was performed with FRET acceptor photobleaching protocol from Leica (https://downloads.leica-microsystems.com/TCS%20SP8/Application%20Note/FRET_AB_with%20SP8-AppLetter_EN.pdf, accessed 25th September 2024). Quantification was performed with Fiji.

Fluorescence activation and transfer observation in live cell

HeLa cells were seeded in Ibidi 4 well plate (Ibidi, Gräfelfing, Germany, #80426) with a density of 40.000 cells/well. Cells were transfected with Lipofectamine™ LTX as described by the manufacturer (ThermoFisher, Karlsruhe, Germany, #15338100).

Cells were observed with a Nikon Yokogawa spinning disc microscope with a 60x water objective under 37°C. Activation was performed with a 405 nm laser at 10% laser intensity for 100 iterations. Transfer was observed every 20 sec or 1 sec for 30 min or 5 min, respectively. Quantification was performed with Fiji.

Statistics

Statistical analysis was performed with R-Studio (Positteam, 2023). The statistical methods are listed in corresponding individual legends. Results are shown from at least 3 separate experiments. Significance was determined as: *p≤0.05, **p≤0.009, ***p. ≤0.0009.

12.2 References

Abramson, J., Adler, J., Dunger, J., Evans, R., Green, T., Pritzel, A., Ronneberger, O., Willmore, L., Ballard, A. J., Bambrick, J., Bodenstein, S. W., Evans, D. A., Hung, C. C., O'Neill, M., Reiman, D., Tunyasuvunakool, K., Wu, Z., Žemgulytė, A., Arvaniti, E., … Jumper, J. M. (2024). Accurate structure prediction of biomolecular interactions with AlphaFold 3. *Nature*, *630*(8016), 493–500. https://doi.org/10.1038/s41586-024-07487-w

Adato, A., Lefevre, G., Delprat, B., Michel, V., Michalski, N., Chardenoux, S., Weil, D., El-Amraoui, A., & Petit, C. (2005a). Usherin, the defective protein in Usher syndrome type IIA, is likely to be a component of interstereocilia ankle links in the inner ear sensory cells. *Hum Mol Genet*, *14*(24), 3921–3932. https://doi.org/10.1093/hmg/ddi416

Adato, A., Michel, V., Kikkawa, Y., Reiners, J., Alagramam, K. N., Weil, D., Yonekawa, H., Wolfrum, U., El-Amraoui, A., & Petit, C. (2005b). Interactions in the network of Usher syndrome type 1 proteins. *Hum Mol Genet*, *14*(3), 347–356. https://doi.org/10.1093/hmg/ddi031

Ahrens, J. B., Nunez-Castilla, J., & Siltberg-Liberles, J. (2017). Evolution of intrinsic disorder in eukaryotic proteins. In *Cellular and Molecular Life Sciences* (Vol. 74, Issue 17, pp. 3163–3174). Birkhauser Verlag AG. https://doi.org/10.1007/s00018-017-2559-0

Aisa-Marin, I., Garcia-Arroyo, R., Mirra, S., & Marfany, G. (2021). The Alter Retina: Alternative Splicing of Retinal Genes in Health and Disease. *Int J Mol Sci*, *22*(4). https://doi.org/10.3390/ijms22041855

Alberti, S., & Dormann, D. (2019). Liquid-Liquid Phase Separation in Disease. In *Annual Review of Genetics* (Vol. 53, pp. 171–194). Annual Reviews Inc. https://doi.org/10.1146/annurev-genet-112618-043527

Alberti, S., Gladfelter, A., & Mittag, T. (2019). Considerations and Challenges in Studying Liquid-Liquid Phase Separation and Biomolecular Condensates. In *Cell* (Vol. 176, Issue 3, pp. 419–434). Cell Press. https://doi.org/10.1016/j.cell.2018.12.035

Alberti, S., & Hyman, A. A. (2021). Biomolecular condensates at the nexus of cellular stress, protein aggregation disease and ageing. In *Nature Reviews Molecular Cell Biology* (Vol. 22, Issue 3, pp. 196–213). Nature Research. https://doi.org/10.1038/s41580-020-00326-6

Alderson, T. R., Pritišanac, I., Kolarić, E., Moses, A. M., & Forman-Kay, J. D. (2023). Systematic identification of conditionally folded intrinsically disordered regions by AlphaFold2. *BioRxiv*, 2022.02.18.481080. https://doi.org/10.1101/2022.02.18.481080

Ashworth, K. E., Weisbrod, J., & Ballios, B. G. (2024). Inherited Retinal Diseases and Retinal Organoids as Preclinical Cell Models for Inherited Retinal Disease Research. *Genes*, *15*(6). https://doi.org/10.3390/GENES15060705

Ba, A. N. N., Pogoutse, A., Provart, N., & Moses, A. M. (2009). NLStradamus: A simple Hidden Markov Model for nuclear localization signal prediction. *BMC Bioinformatics*, *10*. https://doi.org/10.1186/1471-2105-10-202

Bauss, K., Knapp, B., Jores, P., Roepman, R., Kremer, H., Wijk, E. V, Marker, T., & Wolfrum, U. (2014). Phosphorylation of the Usher syndrome 1G protein SANS controls Magi2-mediated endocytosis. *Hum Mol Genet*, *23*(15), 3923–3942. https://doi.org/10.1093/hmg/ddu104

Bell, C. M., Zack, D. J., & Berlinicke, C. A. (2020). Human Organoids for the Study of Retinal Development and Disease. In *Annual Review of Vision Science* (Vol. 6, pp. 91–114). Annual Reviews Inc. https://doi.org/10.1146/annurev-vision-121219-081855

Bertram, K., Agafonov, D. E., Dybkov, O., Haselbach, D., Leelaram, M. N., Will, C. L., Urlaub, H., Kastner, B., Lührmann, R., & Stark, H. (2017). Cryo-EM Structure of a Pre-catalytic Human Spliceosome Primed for Activation. *Cell*, *170*(4), 701-713.e11. https://doi.org/10.1016/j.cell.2017.07.011

Bourgeois, B., Hutten, S., Gottschalk, B., Hofweber, M., Richter, G., Sternat, J., Abou-Ajram, C., Göbl, C., Leitinger, G., Graier, W. F., Dormann, D., & Madl, T. (2020). Nonclassical nuclear localization signals mediate nuclear import of CIRBP. *Proceedings of the National Academy of Sciences of the United States of America*, *117*(15), 8503–8514. https://doi.org/10.1073/PNAS.1918944117/-/DCSUPPLEMENTAL

Buskin, A., Zhu, L., Chichagova, V., Basu, B., Mozaffari-Jovin, S., Dolan, D., Droop, A., Collin, J., Bronstein, R., Mehrotra, S., Farkas, M., Hilgen, G., White, K., Pan, K. T., Treumann, A., Hallam, D., Bialas, K., Chung, G., Mellough, C., … Lako, M. (2018). Disrupted alternative splicing for genes implicated in splicing and ciliogenesis causes PRPF31 retinitis pigmentosa. *Nat Commun*, *9*(1). https://doi.org/10.1038/s41467-018-06448-y

Caberlotto, E., Michel, V., Foucher, I., Bahloul, A., Goodyear, R. J., Pepermans, E., Michalski, N., Perfettini, I., Alegria-Prévot, O., Chardenoux, S., Cruzeiro, M. Do, Hardelin, J. P., Richardson, G. P., Avan, P., Weil, D., Petit, C., Alegria-Prevot, O., Chardenoux, S., Do Cruzeiro, M., … Petit, C. (2011). Usher type 1G protein sans is a critical component of the tip-link complex, a structure controlling actin polymerization in stereocilia. *Proc Natl Acad Sci U S A*, *108*(14), 5825–5830. https://doi.org/10.1073/pnas.1017114108

Cai, N., Lai, A. C. K., Liao, K., Corridon, P. R., Graves, D. J., & Chan, V. (2022). Recent Advances in Fluorescence Recovery after Photobleaching for Decoupling Transport and Kinetics of Biomacromolecules in Cellular Physiology. In *Polymers* (Vol. 14, Issue 9). MDPI. https://doi.org/10.3390/polym14091913

Charenton, C., Wilkinson, M. E., & Nagai, K. (2019). Mechanism of 5' splice site transfer for human spliceosome activation. *Science*, *364*(6438), 362–367. https://doi.org/10.1126/science.aax3289

Chiu, S. H., Ho, W. L., Sun, Y. C., Kuo, J. C., & Huang, J. rong. (2022). Phase separation driven by interchangeable properties in the intrinsically disordered regions of protein paralogs. *Communications Biology*, *5*(1). https://doi.org/10.1038/s42003-022-03354-4

Colcombet-Cazenave, B., Druart, K., Bonnet, C., Petit, C., Sperandio, O., Guglielmini, J., & Wolff, N. (2021). Phylogenetic analysis of Harmonin homology domains. *BMC Bioinformatics*, *22*(1), 190. https://doi.org/10.1186/s12859-021-04116-5

Cowan, C. S., Renner, M., De Gennaro, M., Gross-Scherf, B., Goldblum, D., Hou, Y., Munz, M., Rodrigues, T. M., Krol, J., Szikra, T., Cuttat, R., Waldt, A., Papasaikas, P., Diggelmann, R., Patino-Alvarez, C. P., Galliker, P., Spirig, S. E., Pavlinic, D., Gerber-Hollbach, N., … Roska, B. (2020). Cell Types of the Human Retina and Its Organoids at Single-Cell Resolution. *Cell*, *182*(6), 1623-1640 e34. https://doi.org/10.1016/j.cell.2020.08.013

Crawley, S. W., Weck, M. L., Grega-Larson, N. E., Shifrin, D. A., & Tyska, M. J. (2016). ANKS4B Is Essential for Intermicrovillar Adhesion Complex Formation. *Developmental Cell*, *36*(2), 190–200. https://doi.org/10.1016/J.DEVCEL.2015.12.022

Das, R. K., Ruff, K. M., & Pappu, R. V. (2015). Relating sequence encoded information to form and function of intrinsically disordered proteins. In *Curr Opin Struct Biol* (Vol. 32, pp. 102–112). Elsevier Ltd. https://doi.org/10.1016/j.sbi.2015.03.008

De Ganck, A., Hubert, T., Van Impe, K., Geelen, D., Vandekerckhove, J., De Corte, V., & Gettemans, J. (2005). A monopartite nuclear localization sequence regulates nuclear targeting of the actin binding protein myopodin. *FEBS Letters*, *579*(29), 6673–6680. https://doi.org/10.1016/J.FEBSLET.2005.10.054

Delmaghani, S., & El-Amraoui, A. (2022). The genetic and phenotypic landscapes of Usher syndrome: from disease mechanisms to a new classification. *Human Genetics*, *141*(3–4), 709–735. https://doi.org/10.1007/S00439-022-02448-7

Delprat, B., Michel, V., Goodyear, R., Yamasaki, Y., Michalski, N., El-Amaraoui, A., Perfettini, I., Legrain, P., Richardson, G., Hardelin, J. P., & Petit, C. (2005). Myosin XVa and whirlin, two deafness gene products required for hair bundle growth, are located at the stereocilia tips and interact directly. *Human Molecular Genetics*, *14*(3), 401–410. https://doi.org/10.1093/hmg/ddi036

Dickmanns, A., Monecke, T., & Ficner, R. (2015). Structural basis of targeting the exportin CRM1 in cancer. In *Cells* (Vol. 4, Issue 3, pp. 538–568). MDPI. https://doi.org/10.3390/cells4030538

Dulon, D., Papal, S., Patni, P., Cortese, M., Vincent, P. F. Y., Tertrais, M., Emptoz, A., Tlili, A., Bouleau, Y., Michel, V., Delmaghani, S., Aghaie, A., Pepermans, E., Alegria-Prevot, O., Akil, O., Lustig, L., Avan, P., Safieddine, S., Petit, C., & El-Amraoui, A. (2018). Clarin-1 gene transfer rescues auditory synaptopathy in model of Usher syndrome. *Journal of Clinical Investigation*, *128*(8), 3382–3401. https://doi.org/10.1172/JCI94351

Dyson, H. J., & Wright, P. E. (2021). NMR illuminates intrinsic disorder. In *Current Opinion in Structural Biology* (Vol. 70, pp. 44–52). Elsevier Ltd. https://doi.org/10.1016/j.sbi.2021.03.015

Eberhard, D. A., Karns, L. R., VandenBerg, S. R., & Creutz, C. E. (2001). Control of the nuclear-cytoplasmic partitioning of annexin II by a nuclear export signal and by p11 binding. *Journal of Cell Science*, *114*(Pt 17), 3155–3166. https://doi.org/10.1242/JCS.114.17.3155

Ederle, H., & Dormann, D. (2017). TDP-43 and FUS en route from the nucleus to the cytoplasm. In *FEBS Letters* (Vol. 591, Issue 11, pp. 1489–1507). Wiley Blackwell. https://doi.org/10.1002/1873-3468.12646

Emenecker, R. J., Griffith, D., & Holehouse, A. S. (2021). Metapredict: a fast, accurate, and easy-to-use predictor of consensus disorder and structure. *Biophys. J.*, *120*(20), 4312–4319. https://doi.org/10.1016/j.bpj.2021.08.039

Evans, R., O'neill, M., Pritzel, A., Antropova, N., Senior, A., Green, T., Žídek, A., Bates, R., Blackwell, S., Yim, J., Ronneberger, O., Bodenstein, S., Zielinski, M., Bridgland, A., Potapenko, A., Cowie, A., Tunyasuvunakool, K., Jain, R., Clancy, E., … Hassabis, D. (2021). Protein complex prediction with AlphaFold-Multimer. *BioRxiv*, 2021.10.04.463034. https://doi.org/10.1101/2021.10.04.463034

Ferrer, M., Rodríguez, J. A., Spierings, E. A., de Winter, J. P., Giaccone, G., & Kruyt, F. A. E. (2005). Identification of multiple nuclear export sequences in Fanconi anemia group A protein that contribute to CRM1-dependent nuclear export. *Human Molecular Genetics*, *14*(10), 1271–1281. https://doi.org/10.1093/HMG/DDI138

Fokkema, I. F. A. C., Taschner, P. E. M., Schaafsma, G. C. P., Celli, J., Laros, J. F. J., & den Dunnen, J. T. (2011). LOVD v.2.0: The next generation in gene variant databases. *Hum Mutat*, *32*(5), 557–563. https://doi.org/10.1002/humu.21438

Francis, A. C., Marin, M., Singh, P. K., Achuthan, V., Prellberg, M. J., Palermino-Rowland, K., Lan, S., Tedbury, P. R., Sarafianos, S. G., Engelman, A. N., & Melikyan, G. B. (2020). HIV-1 replication complexes accumulate in nuclear speckles and integrate into speckle-associated genomic domains. *Nature Communications*, *11*(1). https://doi.org/10.1038/S41467-020-17256-8

Fritze, J. S., Stiehler, F. F., & Wolfrum, U. (2023). Pathogenic Variants in USH1G/SANS Alter Protein Interaction with Pre-RNA Processing Factors PRPF6 and PRPF31 of the Spliceosome. *International Journal of Molecular Sciences*, *24*(24). https://doi.org/10.3390/IJMS242417608

Fritze, J. S., Stiehler, F. F., & Wolfrum, U. (2024). Nuclear–Cytoplasmic Shuttling of the Usher Syndrome 1G Protein SANS Differs from Its Paralog ANKS4B. *Cells*, *13*(22), 1855. https://doi.org/10.3390/cells13221855

Fung, H. Y. J., Fu, S. C., & Chook, Y. M. (2017). Nuclear export receptor CRM1 recognizes diverse conformations in nuclear export signals. *ELife*, *6*. https://doi.org/10.7554/ELIFE.23961

Fung, H. Y. J., Niesman, A., & Chook, Y. M. (2021). An update to the CRM1 cargo/NES database NESdb. In *Molecular Biology of the Cell* (Vol. 32, Issue 6, pp. 467–469). American Society for Cell Biology. https://doi.org/10.1091/MBC.E20-11-0694

Fuster-Garcia, C., Garcia-Bohorquez, B., Rodriguez-Munoz, A., Aller, E., Jaijo, T., Millan, J. M., & Garcia-Garcia, G. (2021). Usher Syndrome: Genetics of a Human Ciliopathy. *Int J Mol Sci*, *22*(13). https://doi.org/10.3390/ijms22136723

Géléoc, G. G. S., & El-Amraoui, A. (2020). Disease mechanisms and gene therapy for Usher syndrome. In *Hear Res* (Vol. 394). Elsevier B.V. https://doi.org/10.1016/j.heares.2020.107932

Ghram, M., Morris, G., Culjkovic-Kraljacic, B., Mars, J., Gendron, P., Skrabanek, L., Revuelta, M. V., Cerchietti, L., Guzman, M. L., & Borden, K. L. B. (2023). The eukaryotic translation initiation factor eIF4E reprograms alternative splicing. *EMBO J*, *42*(7). https://doi.org/10.15252/embj.2021110496

Graves, M. J., Matoo, S., Choi, M. S., Storad, Z. A., El Sheikh Idris, R. A., Pickles, B. K., Acharya, P., Shinder, P. E., Arvay, T. O., & Crawley, S. W. (2020). A cryptic sequence targets the adhesion complex scaffold ANKS4B to apical microvilli to promote enterocyte brush border assembly. *The Journal of Biological Chemistry*, *295*(36), 12588–12604. https://doi.org/10.1074/JBC.RA120.013790

Grillet, N., Xiong, W., Reynolds, A., Kazmierczak, P., Sato, T., Lillo, C., Dumont, R. A., Hintermann, E., Sczaniecka, A., Schwander, M., Williams, D., Kachar, B., Gillespie, P. G., & Muller, U. (2009). Harmonin mutations cause mechanotransduction defects in cochlear hair cells. *Neuron*, *62*(3), 375–387. https://doi.org/10.1016/j.neuron.2009.04.006

Guo, Q., Dammer, E. B., Zhou, M., Kundinger, S. R., Gearing, M., Lah, J. J., Levey, A. I., Shulman, J. M., & Seyfried, N. T. (2021). Targeted Quantification of Detergent-Insoluble RNA-Binding Proteins in Human Brain Reveals Stage and Disease Specific Co-aggregation in Alzheimer's Disease. *Frontiers in Molecular Neuroscience*, *14*. https://doi.org/10.3389/fnmol.2021.623659

Gwon, Y., Maxwell, B. A., Kolaitis, R. M., Zhang, P., Kim, H. J., & Taylor, J. P. (2021). Ubiquitination of G3BP1 mediates stress granule disassembly in a context-specific manner. *Science (New York, N.Y.)*, *372*(6549). https://doi.org/10.1126/SCIENCE.ABF6548

Hasenson, S. E., & Shav-Tal, Y. (2020). Speculating on the Roles of Nuclear Speckles: How RNA-Protein Nuclear Assemblies Affect Gene Expression. *BioEssays*, *42*(10). https://doi.org/10.1002/bies.202000104

He, Y., Li, J., & Zhang, M. (2019). Myosin VII, USH1C, and ANKS4B or USH1G Together Form Condensed Molecular Assembly via Liquid-Liquid Phase Separation. *Cell Rep*, *29*(4), 974-986.e4. https://doi.org/10.1016/j.celrep.2019.09.027

Hevekerl, H., Spielmann, T., Chmyrov, A., & Widengren, J. (2011). Förster resonance energy transfer beyond 10 nm: Exploiting the triplet state kinetics of organic fluorophores. *J Phys Chem*, *115*(45), 13360–13370. https://doi.org/10.1021/jp206770s

Holehouse, A. S., Das, R. K., Ahad, J. N., Richardson, M. O. G., & Pappu, R. V. (2017). CIDER: Resources to Analyze Sequence-Ensemble Relationships of Intrinsically Disordered Proteins. *Biophys J*, *112*(1), 16–21. https://doi.org/10.1016/j.bpj.2016.11.3200

Islam, Z., Nagampalli, R. S. K., Fatima, M. T., & Ashraf, G. M. (2018). New paradigm in ankyrin repeats: Beyond protein-protein interaction module. *Int J Biol Macromol*, *109*, 1164–1173. https://doi.org/10.1016/j.ijbiomac.2017.11.101

Ittisoponpisan, S., Islam, S. A., Khanna, T., Alhuzimi, E., David, A., & Sternberg, M. J. E. (2019). Can Predicted Protein 3D Structures Provide Reliable Insights into whether Missense Variants Are Disease Associated? *Journal of Molecular Biology*, *431*(11), 2197–2212. https://doi.org/10.1016/J.JMB.2019.04.009

Jans, D. A., Martin, A. J., & Wagstaff, K. M. (2019). Inhibitors of nuclear transport. *Current Opinion in Cell Biology*, *58*, 50–60. https://doi.org/10.1016/J.CEB.2019.01.001

Johnston, A. M., Naselli, G., Niwa, H., Brodnicki, T., Harrison, L. C., & Góñez, L. J. (2004). Harp (harmonin-interacting, ankyrin repeat-containing protein), a novel protein that interacts with harmonin in epithelial tissues. *Genes to Cells*, *9*(10), 967–982. https://doi.org/10.1111/j.1365-2443.2004.00776.x

Jumper, J., Evans, R., Pritzel, A., Green, T., Figurnov, M., Ronneberger, O., Tunyasuvunakool, K., Bates, R., Žídek, A., Potapenko, A., Bridgland, A., Meyer, C., Kohl, S. A. A., Ballard, A. J., Cowie, A., Romera-Paredes, B., Nikolov, S., Jain, R., Adler, J., … Hassabis, D. (2021). Highly accurate protein structure prediction with AlphaFold. *Nature*. https://doi.org/10.1038/s41586-021-03819-2

Karpova, T. S., Baumann, C. T., He, L., Wu, X., Grammer, A., Lipsky, P., Hager, G. L., & McNally, J. G. (2003). Fluorescence resonance energy transfer from cyan to yellow fluorescent protein detected by acceptor photobleaching using confocal microscopy and a single laser. *J Microsc*, *209*(1), 56–70. https://doi.org/10.1046/j.1365-2818.2003.01100.x

Kazmierczak, P., Sakaguchi, H., Tokita, J., Wilson-Kubalek, E. M., Milligan, R. A., Müller, U., & Kachar, B. (2007). Cadherin 23 and protocadherin 15 interact to form

tip-link filaments in sensory hair cells. *Nature*, *449*(7158), 87–91. https://doi.org/10.1038/nature06091

Kikkawa, Y., Shitara, H., Wakana, S., Kohara, Y., Takada, T., Okamoto, M., Taya, C., Kamiya, K., Yoshikawa, Y., Tokano, H., Kitamura, K., Shimizu, K., Wakabayashi, Y., Shiroishi, T., Kominami, R., & Yonekawa, H. (2003). Mutations in a new scaffold protein Sans cause deafness in Jackson shaker mice. *Human Molecular Genetics*, *12*(5), 453–461. https://doi.org/10.1093/hmg/ddg042

Kim, T. Y., Ha, C. W., & Huh, W. K. (2009). Differential subcellular localization of ribosomal protein L7 paralogs in Saccharomyces cerevisiae. *Molecules and Cells*, *27*(5), 539–546. https://doi.org/10.1007/s10059-009-0077-0

Kopp, M., Rotan, O., Papadopoulos, C., Schulze, N., Meyer, H., & Epple, M. (2017). Delivery of the autofluorescent protein R-phycoerythrin by calcium phosphate nanoparticles into four different eukaryotic cell lines (HeLa, HEK293T, MG-63, MC3T3): Highly efficient, but leading to endolysosomal proteolysis in HeLa and MC3T3 cells. *PloS One*, *12*(6). https://doi.org/10.1371/JOURNAL.PONE.0178260

Koulouras, G., Panagopoulos, A., Rapsomaniki, M. A., Giakoumakis, N. N., Taraviras, S., & Lygerou, Z. (2018). EasyFRAP-web: A web-based tool for the analysis of fluorescence recovery after photobleaching data. *Nucleic Acids Research*, *46*(W1), W467–W472. https://doi.org/10.1093/nar/gky508

Kumagai, A., & Dunphy, W. G. (1999). Binding of 14-3-3 proteins and nuclear export control the intracellular localization of the mitotic inducer Cdc25. *Genes & Development*, *13*(9), 1067–1072. https://doi.org/10.1101/GAD.13.9.1067

Levin, A., Neufeldt, C. J., Pang, D., Wilson, K., Loewen-Dobler, D., Joyce, M. A., Wozniak, R. W., & Tyrrell, D. L. J. (2014). Functional characterization of nuclear localization and export signals in hepatitis C virus proteins and their role in the membranous web. *PloS One*, *9*(12). https://doi.org/10.1371/JOURNAL.PONE.0114629

Li, J., He, Y., Lu, Q., & Zhang, M. (2016). Mechanistic Basis of Organization of the Harmonin/USH1C-Mediated Brush Border Microvilli Tip-Link Complex. *Developmental Cell*, *36*(2), 179–189. https://doi.org/10.1016/J.DEVCEL.2015.12.020

Liao, S. E., & Regev, O. (2021). Splicing at the phase-separated nuclear speckle interface: a model. *Nucleic Acids Research*, *49*(2), 636–645. https://doi.org/10.1093/nar/gkaa1209

Linnert, J., Knapp, B., Güler, B. E., Boldt, K., Ueffing, M., & Wolfrum, U. (2023). Usher syndrome proteins ADGRV1 (USH2C) and CIB2 (USH1J) interact and share a common interactome containing TRiC/CCT-BBS chaperonins. *Frontiers in Cell and Developmental Biology*, *11*. https://doi.org/10.3389/fcell.2023.1199069

Liu, S., Li, P., Dybkov, O., Nottrott, S., Hartmuth, K., Lührmann, R., Carlomagno, T., & Wahl, M. C. (2007). Binding of the human Prp31 Nop domain to a composite RNA-protein platform in U4 snRNP. *Science*, *316*(5821), 115–120. https://doi.org/10.1126/science.1137924

Liu, S., Rauhut, R., Vornlocher, H. P., & Lührmann, R. (2006). The network of protein-protein interactions within the human U4/U6.U5 tri-snRNP. *RNA*, *12*(7), 1418–1430. https://doi.org/10.1261/rna.55406

Lou, M., Pang, C. W. M., Gerken, A. E., & Brock, T. G. (2004). Multiple nuclear localization sequences allow modulation of 5-lipoxygenase nuclear import. *Traffic (Copenhagen, Denmark)*, *5*(11), 847–854. https://doi.org/10.1111/J.1600-0854.2004.00227.X

Lu, J., Wu, T., Zhang, B., Liu, S., Song, W., Qiao, J., & Ruan, H. (2021). Types of nuclear localization signals and mechanisms of protein import into the nucleus. In *Cell Communication and Signaling* (Vol. 19, Issue 1). BioMed Central Ltd. https://doi.org/10.1186/s12964-021-00741-y

Lukowski, S. W., Lo, C. Y., Sharov, A. A., Nguyen, Q., Fang, L., Hung, S. S., Zhu, L., Zhang, T., Grünert, U., Nguyen, T., Senabouth, A., Jabbari, J. S., Welby, E., Sowden, J. C., Waugh, H. S., Mackey, A., Pollock, G., Lamb, T. D., Wang, P., … Wong, R. C. (2019). A single-cell transcriptome atlas of the adult human retina. *The EMBO Journal*, *38*(18). https://doi.org/10.15252/EMBJ.2018100811

Macara, I. G. (2001). Transport into and out of the nucleus. *Microbiology and Molecular Biology Reviews : MMBR*, *65*(4), 570–594. https://doi.org/10.1128/MMBR.65.4.570-594.2001

Maerker, T., van Wijk, E., Overlack, N., Kersten, F. F. J., Mcgee, J., Goldmann, T., Sehn, E., Roepman, R., Walsh, E. J., Kremer, H., & Wolfrum, U. (2008). A novel Usher protein network at the periciliary reloading point between molecular transport machineries in vertebrate photoreceptor cells. *Hum Mol Genet*, *17*(1), 71–86. https://doi.org/10.1093/hmg/ddm285

Makarov, E. M., Makarova, O. V., Achsel, T., & Lührmann, R. (2000). The human homologue of the yeast splicing factor Prp6p contains multiple TPR elements and

is stably associated with the U5 snRNP via protein-protein interactions. *Journal of Molecular Biology*, *298*(4), 567–575. https://doi.org/10.1006/jmbi.2000.3685

Makarova, O. V., Makarov, E. M., Liu, S., Vornlocher, H. P., & Lührmann, R. (2002). Protein 61K, encoded by a gene (PRPF31) linked to autosomal dominant retinitis pigmentosa, is required for U4/U6·U5 tri-snRNP formation and pre-mRNA splicing. *EMBO Journal*, *21*(5), 1148–1157. https://doi.org/10.1093/emboj/21.5.1148

Matera, A. G., & Wang, Z. (2014). A day in the life of the spliceosome. In *Nat Rev Mol Cell Biol* (Vol. 15, Issue 2, pp. 108–121). Nat Rev Mol Cell Biol. https://doi.org/10.1038/nrm3742

Mathur, P., & Yang, J. (2015). Usher syndrome: Hearing loss, retinal degeneration and associated abnormalities. *Biochim Biophys Acta*, *1852*(3), 406–420. https://doi.org/10.1016/j.bbadis.2014.11.020

Mears, W. E., Lam, V., & Rice, S. A. (1995). Identification of nuclear and nucleolar localization signals in the herpes simplex virus regulatory protein ICP27. *Journal of Virology*, *69*(2), 935–947. https://doi.org/10.1128/jvi.69.2.935-947.1995

Michalski, N., Michel, V., Bahloul, A., Lefèvre, G., Barral, J., Yagi, H., Chardenoux, S., Weil, D., Martin, P., Hardelin, J. P., Sato, M., & Petit, C. (2007). Molecular characterization of the ankle-link complex in cochlear hair cells and its role in the hair bundle functioning. *Journal of Neuroscience*, *27*(24), 6478–6488. https://doi.org/10.1523/JNEUROSCI.0342-07.2007

Michel, V., Pepermans, E., Boutet de Monvel, J., England, P., Nouaille, S., Aghaie, A., Delhommel, F., Wolff, N., Perfettini, I., Hardelin, J. P., Petit, C., & Bahloul, A. (2020). Interaction of protocadherin-15 with the scaffold protein whirlin supports its anchoring of hair-bundle lateral links in cochlear hair cells. *Scientific Reports*, *10*(1). https://doi.org/10.1038/S41598-020-73158-1

Millan, J. M., Aller, E., Jaijo, T., Blanco-Kelly, F., Gimenez-Pardo, A., & Ayuso, C. (2011). An update on the genetics of usher syndrome. *J Ophthalmol*, *2011*, 417217. https://doi.org/10.1155/2011/417217

Mirdita, M., Schütze, K., Moriwaki, Y., Heo, L., Ovchinnikov, S., & Steinegger, M. (2022). ColabFold: making protein folding accessible to all. *Nat Methods*, *19*(6), 679–682. https://doi.org/10.1038/s41592-022-01488-1

Miyasaka, Y., Shitara, H., Suzuki, S., Yoshimoto, S., Seki, Y., Ohshiba, Y., Okumura, K., Taya, C., Tokano, H., Kitamura, K., Takada, T., Hibino, H., Shiroishi, T., Kominami, R., Yonekawa, H., & Kikkawa, Y. (2016). Heterozygous mutation of

Ush1g/Sans in mice causes early-onset progressive hearing loss, which is recovered by reconstituting the strain-specific mutation in Cdh23. *Human Molecular Genetics*, *25*(10), 2045–2059. https://doi.org/10.1093/hmg/ddw078

Mroczek, S., & Dziembowski, A. (2013). U6 RNA biogenesis and disease association. *Wiley Interdisciplinary Reviews. RNA*, *4*(5), 581–592. https://doi.org/10.1002/WRNA.1181

Murphy, D., Cieply, B., Carstens, R., Ramamurthy, V., & Stoilov, P. (2016). The Musashi 1 Controls the Splicing of Photoreceptor-Specific Exons in the Vertebrate Retina. *PLoS Genet*, *12*(8), e1006256. https://doi.org/10.1371/journal.pgen.1006256

Nagel-Wolfrum, K., Fadl, B. R., Becker, M. M., Wunderlich, K. A., Schäfer, J., Sturm, D., Fritze, J., Gür, B., Kaplan, L., Andreani, T., Goldmann, T., Brooks, M., Starostik, M. R., Lokhande, A., Apel, M., Fath, K. R., Stingl, K., Kohl, S., Deangelis, M. M., … Wolfrum, U. (2023). Expression and subcellular localization of USH1C/harmonin in human retina provides insights into pathomechanisms and therapy. *Hum Mol Genet*, *32*(3), 431–449. https://doi.org/10.1093/hmg/ddac211

Napolitano, G., Esposito, A., Choi, H., Matarese, M., Benedetti, V., Di Malta, C., Monfregola, J., Medina, D. L., Lippincott-Schwartz, J., & Ballabio, A. (2018). mTOR-dependent phosphorylation controls TFEB nuclear export. *Nature Communications*, *9*(1). https://doi.org/10.1038/s41467-018-05862-6

Nardozzi, J. D., Lott, K., & Cingolani, G. (2010). Phosphorylation meets nuclear import: a review. *Cell Communication and Signaling : CCS*, *8*. https://doi.org/10.1186/1478-811X-8-32

Nguyen Ba, A. N., Yeh, B. J., Van Dyk, D., Davidson, A. R., Andrews, B. J., Weiss, E. L., & Moses, A. M. (2012). Proteome-wide discovery of evolutionary conserved sequences in disordered regions. *Sci Signal*, *5*(215). https://doi.org/10.1126/scisignal.2002515

Novotnýa, I., Blažíková, M., Staněka, D., Herman, P., & Malinsky, J. (2011). In vivo kinetics of U4/U6•U5 tri-snRNP formation in Cajal bodies. *Molecular Biology of the Cell*, *22*(4), 513–523. https://doi.org/10.1091/mbc.E10-07-0560

Nunez-Castilla, J., & Siltberg-Liberles, J. (2020). An easy protocol for evolutionary analysis of intrinsically disordered proteins. In *Methods mol biol* (Vol. 2141, pp. 147–177). Humana Press Inc. https://doi.org/10.1007/978-1-0716-0524-0_7

Ossovskaya, V., Lim, S. T., Ota, N., Schlaepfer, D. D., & Ilic, D. (2008). FAK nuclear export signal sequences. *FEBS Letters*, *582*(16), 2402–2406. https://doi.org/10.1016/j.febslet.2008.06.004

Overlack, N., Kilic, D., Bauss, K., Marker, T., Kremer, H., van Wijk, E., Wolfrum, U., Bauß, K., Märker, T., Kremer, H., van Wijk, E., & Wolfrum, U. (2011). Direct interaction of the Usher syndrome 1G protein SANS and myomegalin in the retina. *Biochim Biophys Acta*, *1813*(10), 1883–1892. https://doi.org/10.1016/j.bbamcr.2011.05.015

Overlack, N., Maerker, T., Latz, M., Nagel-Wolfrum, K., & Wolfrum, U. (2008). SANS (USH1G) expression in developing and mature mammalian retina. *Vision Res*, *48*(3), 400–412. https://doi.org/10.1016/j.visres.2007.08.021

Papal, S., Cortese, M., Legendre, K., Sorusch, N., Dragavon, J., Sahly, I., Shorte, S., Wolfrum, U., Petit, C., & El-Amraoui, A. (2013). The giant spectrin betaV couples the molecular motors to phototransduction and Usher syndrome type I proteins along their trafficking route. *Hum Mol Genet*, *22*(18), 3773–3788. https://doi.org/10.1093/hmg/ddt228

Papasaikas, P., Tejedor, J. R., Vigevani, L., & Valcárcel, J. (2015). Functional splicing network reveals extensive regulatory potential of the core spliceosomal machinery. *Mol. Cell*, *57*(1), 7–22. https://doi.org/10.1016/j.molcel.2014.10.030

Patterson, G. H., & Lippincott-Schwartz, J. (2002). A photoactivatable GFP for selective photolabeling of proteins and cells. *Science (New York, N.Y.)*, *297*(5588), 1873–1877. https://doi.org/10.1126/SCIENCE.1074952

Pemberton, L. F., & Paschal, B. M. (2005). Mechanisms of receptor-mediated nuclear import and nuclear export. *Traffic (Copenhagen, Denmark)*, *6*(3), 187–198. https://doi.org/10.1111/J.1600-0854.2005.00270.X

Pennica, C., Hanna, G., Islam, S. A., Sternberg, M. J. E., & David, A. (2023). Missense3D-PPI: A Web Resource to Predict the Impact of Missense Variants at Protein Interfaces Using 3D Structural Data. *Journal of Molecular Biology*, *435*(14), 168060. https://doi.org/10.1016/J.JMB.2023.168060

Peter, V. G., Quinodoz, M., Sadio, S., Held, S., Rodrigues, M., Soares, M., Sousa, A. B., Coutinho Santos, L., Damme, M., & Rivolta, C. (2021). New clinical and molecular evidence linking mutations in ARSG to Usher syndrome type IV. *Hum Mutat*, *42*(3), 261–271. https://doi.org/10.1002/humu.24150

Pettersen, E. F., Goddard, T. D., Huang, C. C., Couch, G. S., Greenblatt, D. M., Meng, E. C., & Ferrin, T. E. (2004). UCSF Chimera - A visualization system for exploratory research and analysis. *J Comput Chem*, *25*(13), 1605–1612. https://doi.org/10.1002/jcc.20084

Positteam. (2023). *Download RStudio - Posit*. https://posit.co/downloads/

Rai, A. K., Chen, J. X., Selbach, M., & Pelkmans, L. (2018). Kinase-controlled phase transition of membraneless organelles in mitosis. *Nature*, *559*(7713), 211–216. https://doi.org/10.1038/S41586-018-0279-8

Reichenbach, A., & Bringmann, A. (2020). Glia of the human retina. *GLIA*, *68*(4), 768–796. https://doi.org/10.1002/glia.23727

Reiners, J., van Wijk, E., Marker, T., Zimmermann, U., Jurgens, K., te Brinke, H., Overlack, N., Roepman, R., Knipper, M., Kremer, H., & Wolfrum, U. (2005). Scaffold protein harmonin (USH1C) provides molecular links between Usher syndrome type 1 and type 2. *Human Molecular Genetics*, *14*(24), 3933–3943. https://doi.org/10.1093/hmg/ddi417

Riazuddin, S., Belyantseva, I. A., Giese, A. P. J., Lee, K., Indzhykulian, A. A., Nandamuri, S. P., Yousaf, R., Sinha, G. P., Lee, S., Terrell, D., Hegde, R. S., Ali, R. A., Anwar, S., Andrade-Elizondo, P. B., Sirmaci, A., Parise, L. V., Basit, S., Wali, A., Ayub, M., … Ahmed, Z. M. (2012). Alterations of the CIB2 calcium-and integrin-binding protein cause Usher syndrome type 1J and nonsyndromic deafness DFNB48. *Nature Genetics*, *44*(11), 1265–1271. https://doi.org/10.1038/ng.2426

Roszik, J., Tóth, G., Szöllosi, J., & Vereb, G. (2013). Validating pharmacological disruption of protein-protein interactions by acceptor photobleaching FRET imaging. *Methods Mol Biol*, *986*, 165–178. https://doi.org/10.1007/978-1-62703-311-4_11

Sahly, I., Dufour, E., Schietroma, C., Michel, V., Bahloul, A., Perfettini, I., Pepermans, E., Estivalet, A., Carette, D., Aghaie, A., Ebermann, I., Lelli, A., Iribarne, M., Hardelin, J. P., Weil, D., Sahel, J. A., El-Amraoui, A., & Petit, C. (2012). Localization of Usher 1 proteins to the photoreceptor calyceal processes, which are absent from mice. *J Cell Biol*, *199*(2), 381–399. https://doi.org/10.1083/jcb.201202012

Sakiyama, H., Wynn, R. M., Lee, W. R., Fukasawa, M., Mizuguchi, H., Gardner, K. H., Repa, J. J., & Uyeda, K. (2008). Regulation of nuclear import/export of carbohydrate response element-binding protein (ChREBP): Interaction of anα-

helix of ChREBP with the 14-3-3 proteins and regulation by phosphorylation. *Journal of Biological Chemistry*, *283*(36), 24899–24908. https://doi.org/10.1074/jbc.M804308200

Sato, Y., Hatta, M., Karim, M. F., Sawa, T., Wei, F. Y., Sato, S., Magnuson, M. A., Gonzalez, F. J., Tomizawa, K., Akaike, T., Yoshizawa, T., & Yamagata, K. (2012). Anks4b, a novel target of HNF4α protein, interacts with GRP78 protein and regulates endoplasmic reticulum stress-induced apoptosis in pancreatic β-cells. *Journal of Biological Chemistry*, *287*(27), 23236–23245. https://doi.org/10.1074/jbc.M112.368779

Schaffert, N., Hossbach, M., Heintzmann, R., Achsel, T., & Lührmann, R. (2004). RNAi knockdown of hPrp31 to an accumulation of U4/U6 di-snRNPs in Cajal bodies. *EMBO Journal*, *23*(15), 3000–3009. https://doi.org/10.1038/sj.emboj.7600296

Schindelin, J., Rueden, C. T., Hiner, M. C., & Eliceiri, K. W. (2015). The ImageJ ecosystem: An open platform for biomedical image analysis. *Mol Reprod Dev*, *82*(7–8), 518–529. https://doi.org/10.1002/mrd.22489

Schmid-Burgk, J. L., Höning, K., Ebert, T. S., & Hornung, V. (2016). CRISPaint allows modular base-specific gene tagging using a ligase-4-dependent mechanism. *Nature Communications*, *7*. https://doi.org/10.1038/NCOMMS12338

Schneider, R., Blackledge, M., & Jensen, M. R. (2019). Elucidating binding mechanisms and dynamics of intrinsically disordered protein complexes using NMR spectroscopy. In *Current Opinion in Structural Biology* (Vol. 54, pp. 10–18). Elsevier Ltd. https://doi.org/10.1016/j.sbi.2018.09.007

Senften, M., Schwander, M., Kazmierczak, P., Lillo, C., Shin, J. B., Hasson, T., Géléoc, G. S. G., Gillespie, P. G., Williams, D., Holt, J. R., & Müller, U. (2006). Physical and functional interaction between protocadherin 15 and myosin VIIa in mechanosensory hair cells. *Journal of Neuroscience*, *26*(7), 2060–2071. https://doi.org/10.1523/JNEUROSCI.4251-05.2006

Sheinerman, F. B., Norel, R., & Honig, B. (2000). Electrostatic aspects of protein-protein interactions. In *Curr Opin Struct Biol* (Vol. 10, Issue 2, pp. 153–159). Current Biology Ltd. https://doi.org/10.1016/S0959-440X(00)00065-8

Shoubridge, C., Tan, M., Fullston, T., Cloosterman, D., Coman, D., McGillivray, G., Mancini, G., Kleefstra, T., & Gécz, J. (2010). Mutations in the nuclear localization sequence of the Aristaless related homeobox; sequestration of mutant ARX with

IPO13 disrupts normal subcellular distribution of the transcription factor and retards cell division. *PathoGenetics*, *3*(1). https://doi.org/10.1186/1755-8417-3-1

Shpargel, K. B., Ospina, J. K., Tucker, K. E., Matera, G. G., & Hebert, M. D. (2003). Control of Cajal body number is mediated by the coilin C-terminus. In *Journal of Cell Science* (Vol. 116, Issue 2, pp. 303–312). J Cell Sci. https://doi.org/10.1242/jcs.00211

Singh, N., & Bhalla, N. (2020). Moonlighting Proteins. In *Annual Review of Genetics* (Vol. 54, pp. 265–285). Annual Reviews Inc. https://doi.org/10.1146/annurev-genet-030620-102906

Sleeman, J. E., & Lamond, A. I. (1999). Newly assembled snRNPs associate with coiled bodies before speckles, suggesting a nuclear snRNP maturation pathway. *Current Biology*, *9*(19), 1065–1074. https://doi.org/10.1016/S0960-9822(99)80475-8

Sleeman, J. E., Trinkle-Mulcahy, L., Prescott, A. R., Ogg, S. C., & Lamond, A. I. (2003). Cajal body proteins SMN and Coilin show differential dynamic behaviour in vivo. *Journal of Cell Science*, *116*(10), 2039–2050. https://doi.org/10.1242/jcs.00400

Smith, K. M., Di Antonio, V., Bellucci, L., Thomas, D. R., Caporuscio, F., Ciccarese, F., Ghassabian, H., Wagstaff, K. M., Forwood, J. K., Jans, D. A., Palù, G., & Alvisi, G. (2018). Contribution of the residue at position 4 within classical nuclear localization signals to modulating interaction with importins and nuclear targeting. *Biochimica et Biophysica Acta. Molecular Cell Research*, *1865*(8), 1114–1129. https://doi.org/10.1016/J.BBAMCR.2018.05.006

Song, D., Jo, Y., Choi, J. M., & Jung, Y. (2020). Client proximity enhancement inside cellular membrane-less compartments governed by client-compartment interactions. *Nature Communications*, *11*(1). https://doi.org/10.1038/s41467-020-19476-4

Sorusch, N., Baub, K., Plutniok, J., Samanta, A., Knapp, B., Nagel-Wolfrum, K., & Wolfrum, U. (2017). Characterization of the ternary Usher syndrome SANS/ush2a/whirlin protein complex. *Hum Mol Genet*, *26*(6), 1157–1172. https://doi.org/10.1093/hmg/ddx027

Sorusch, N., Wunderlich, K., Bauá, K., Nagel-Wolfrum, K., & Wolfrum, U. (2014). Usher syndrome protein network functions in the retina and their relation to other retinal ciliopathies. *Adv Exp Med Biol*. https://doi.org/10.1007/978-1-4614-3209-8_67

Sorusch, N., Yildirim, A., Knapp, B., Janson, J., Fleck, W., Scharf, C., & Wolfrum, U. (2019). SANS (USH1G) molecularly links the Human Usher Syndrome Protein Network to the Intraflagellar Transport Module by direct binding to IFT-B Proteins. *Front Cell Dev Biol*, *7*, 216. https://doi.org/10.3389/fcell.2019.00216

Staněk, D. (2017). Cajal bodies and snRNPs - friends with benefits. *RNA Biology*, *14*(6), 671–679. https://doi.org/10.1080/15476286.2016.1231359

Stanek, D., Pridalova-Hnilicova, J., Novotny, I., Huranova, M., Blazikova, M., Wen, X., Sapra, A. K., & Neugebauer, K. M. (2008). Spliceosomal small nuclear ribonucleoprotein particles repeatedly cycle through Cajal bodies. *Mol Biol Cell*, *19*(6), 2534–2543. https://doi.org/10.1091/mbc.E07-12-1259

Stenson, P. D., Ball, E. V., Mort, M., Phillips, A. D., Shiel, J. A., Thomas, N. S. T., Abeysinghe, S., Krawczak, M., & Cooper, D. N. (2003). Human Gene Mutation Database (HGMD®): 2003 Update. In *Hum Mutat* (Vol. 21, Issue 6, pp. 577–581). Hum Mutat. https://doi.org/10.1002/humu.10212

Stirling, D. R., Swain-Bowden, M. J., Lucas, A. M., Carpenter, A. E., Cimini, B. A., & Goodman, A. (2021). CellProfiler 4: improvements in speed, utility and usability. *BMC Bioinformatics*, *22*(1). https://doi.org/10.1186/S12859-021-04344-9

Sundar, J., Matalkah, F., Jeong, B., Stoilov, P., & Ramamurthy, V. (2020). The Musashi proteins MSI1 and MSI2 are required for photoreceptor morphogenesis and vision in mice. *Journal of Biological Chemistry*, *296*. https://doi.org/10.1074/jbc.ra120.015714

Tanackovic, G., Ransijn, A., Ayuso, C., Harper, S., Berson, E. L., & Rivolta, C. (2011). A missense mutation in PRPF6 causes impairment of pre-mRNA splicing and autosomal-dominant retinitis pigmentosa. *Am. J. Hum. Genet.*, *88*(5), 643–649. https://doi.org/10.1016/j.ajhg.2011.04.008

Tancredi, T., Carrà, G., Guerrini, R., Arduin, M., Calò, G., Regoli, D., Salvadori, S., & Temussi, P. A. (2005). The interaction of highly helical structural mutants with the NOP receptor discloses the role of the address domain of nociceptin/orphanin FQ. *Chem Eur J*, *11*(7), 2061–2070. https://doi.org/10.1002/chem.200401095

Tessier, T. M., Macneil, K. M., & Mymryk, J. S. (2020). Piggybacking on Classical Import and Other Non-Classical Mechanisms of Nuclear Import Appear Highly Prevalent within the Human Proteome. *Biology*, *9*(8), 1–20. https://doi.org/10.3390/BIOLOGY9080188

Timney, B. L., Raveh, B., Mironska, R., Trivedi, J. M., Kim, S. J., Russel, D., Wente, S. R., Sali, A., & Rout, M. P. (2016). Simple rules for passive diffusion through the nuclear pore complex. *The Journal of Cell Biology*, *215*(1). https://doi.org/10.1083/JCB.201601004

Tomura, M., Ikebuchi, R., Moriya, T., & Kusumoto, Y. (2021). Tracking the fate and migration of cells in live animals with cell-cycle indicators and photoconvertible proteins. *Journal of Neuroscience Methods*, *355*. https://doi.org/10.1016/J.JNEUMETH.2021.109127

Toyota, C. G., Davis, M. D., Cosman, A. M., & Hebert, M. D. (2010). Coilin phosphorylation mediates interaction with SMN and SmB'. *Chromosoma*, *119*(2), 205–215. https://doi.org/10.1007/S00412-009-0249-X

Uhlén, M., Fagerberg, L., Hallström, B. M., Lindskog, C., Oksvold, P., Mardinoglu, A., Sivertsson, Å., Kampf, C., Sjöstedt, E., Asplund, A., Olsson, I. M., Edlund, K., Lundberg, E., Navani, S., Szigyarto, C. A. K., Odeberg, J., Djureinovic, D., Takanen, J. O., Hober, S., … Pontén, F. (2015). Proteomics. Tissue-based map of the human proteome. *Science (New York, N.Y.)*, *347*(6220). https://doi.org/10.1126/SCIENCE.1260419

Ullah, F., Zeeshan Ali, M., Ahmad, S., Muzammal, M., Khan, S., Khan, J., & Ahmad Khan, M. (2024). Current updates on genetic spectrum of usher syndrome. In *Nucleosides, Nucleotides and Nucleic Acids*. Taylor and Francis Ltd. https://doi.org/10.1080/15257770.2024.2344194

van Wijk, E., van der Zwaag, B., Peters, T., Zimmermann, U., te Brinke, H., Kersten, F. F. J., Märker, T., Aller, E., Hoefsloot, L. H., Cremers, C. W. R. J., Cremers, F. P. M., Wolfrum, U., Knipper, M., Roepman, R., & Kremer, H. (2006). The DFNB31 gene product whirlin connects to the Usher protein network in the cochlea and retina by direct association with USH2A and VLGR1. *Human Molecular Genetics*, *15*(5), 751–765. https://doi.org/10.1093/hmg/ddi490

Velde, H. M., Reurink, J., Held, S., Li, C. H. Z., Yzer, S., Oostrik, J., Weeda, J., Haer-Wigman, L., Yntema, H. G., Roosing, S., Pauleikhoff, L., Lange, C., Whelan, L., Dockery, A., Zhu, J., Keegan, D. J., Farrar, G. J., Kremer, H., Lanting, C. P., … Pennings, R. J. E. (2022). Usher syndrome type IV: clinically and molecularly confirmed by novel ARSG variants. *Hum Genet*, *141*(11), 1723–1738. https://doi.org/10.1007/s00439-022-02441-0

Wang, L., Liu, X., Gusev, E., Wang, C., & Fagotto, F. (2014). Regulation of the phosphorylation and nuclear import and export of β-catenin by APC and its cancer-related truncated form. *Journal of Cell Science*, *127*(8), 1647–1659. https://doi.org/10.1242/jcs.131045

Waterhouse, A. M., Procter, J. B., Martin, D. M. A., Clamp, M., & Barton, G. J. (2009). Jalview Version 2-A multiple sequence alignment editor and analysis workbench. *Bioinformatics*, *25*(9), 1189–1191. https://doi.org/10.1093/bioinformatics/btp033

Weil, D., El-Amraoui, A., Masmoudi, S., Mustapha, M., Kikkawa, Y., Laine, S., Delmaghani, S., Adato, A., Nadifi, S., Zina, Z. Ben, Hamel, C., Gal, A., Ayadi, H., Yonekawa, H., Petit, C., Lainé, S., Delmaghani, S., Adato, A., Nadifi, S., … Petit, C. (2003). Usher syndrome type I G (USH1G) is caused by mutations in the gene encoding SANS, a protein that associates with the USH1C protein, harmonin. *Hum Mol Genet*, *12*(5), 463–471. https://doi.org/10.1093/hmg/ddg051

Wiemann, S., Pennacchio, C., Hu, Y., Hunter, P., Harbers, M., Amiet, A., Bethel, G., Busse, M., Carninci, P., Diekhans, M., Dunham, I., Hao, T., Harper, J. W., Hayashizaki, Y., Heil, O., Hennig, S., Hotz-Wagenblatt, A., Jang, W., Jöcker, A., … Hill, D. E. (2016). The ORFeome Collaboration: a genome-scale human ORF-clone resource. *Nature Methods*, *13*(3), 191–192. https://doi.org/10.1038/NMETH.3776

Will, C. L., & Lührmann, R. (2011). Spliceosome structure and function. *Cold Spring Harb Perspect Biol*, *3*(7), 1–2. https://doi.org/10.1101/cshperspect.a003707

Wing, C. E., Fung, H. Y. J., & Chook, Y. M. (2022). Karyopherin-mediated nucleocytoplasmic transport. *Nature Reviews. Molecular Cell Biology*, *23*(5), 307–328. https://doi.org/10.1038/S41580-021-00446-7

Wolfrum, U. (2011). Protein networks related to the Usher syndrome gain insights in the molecular basis of the disease. In S. Ahuja (Ed.), *Usher Syndrome: Pathogenesis, Diagnosis and Therapy* (pp. 51–73). Nova Science Publishers Inc.

Wright, P. E., & Dyson, H. J. (2015). Intrinsically disordered proteins in cellular signalling and regulation. In *Nature Reviews Molecular Cell Biology* (Vol. 16, Issue 1, pp. 18–29). Nature Publishing Group. https://doi.org/10.1038/nrm3920

Xu, B., Peng, Z., Yan, G., Wang, N., Chen, M., Yao, X., Sun, M., & An, Y. (2021). Establishment and Validation of a Genetic Label Associated With M2 Macrophage Infiltration to Predict Survival in Patients With Colon Cancer and to Assist in

Immunotherapy. *Frontiers in Genetics*, *12*. https://doi.org/10.3389/fgene.2021.726387

Xu, D., Marquis, K., Pei, J., Fu, S. C., Całatay, T., Grishin, N. V., & Chook, Y. M. (2015). LocNES: A computational tool for locating classical NESs in CRM1 cargo proteins. *Bioinformatics*, *31*(9), 1357–1365. https://doi.org/10.1093/bioinformatics/btu826

Yan, J., Pan, L., Chen, X., Wu, L., & Zhang, M. (2010). The structure of the harmonin/sans complex reveals an unexpected interaction mode of the two Usher syndrome proteins. *Proc Natl Acad Sci U S A*, *107*(9), 4040–4045. https://doi.org/10.1073/pnas.0911385107

Yang, J., Liu, X., Zhao, Y., Adamian, M., Pawlyk, B., Sun, X., McMillan, D. R., Liberman, M. C., & Li, T. (2010). Ablation of whirlin long isoform disrupts the USH2 protein complex and causes vision and hearing loss. *PLoS Genet*, *6*(5), e1000955. https://doi.org/10.1371/journal.pgen.1000955

Yang, Y., Guo, L., Chen, L., Gong, B., Jia, D., & Sun, Q. (2023). Nuclear transport proteins: structure, function, and disease relevance. *Signal Transduction and Targeted Therapy*, *8*(1). https://doi.org/10.1038/S41392-023-01649-4

Yildirim, A. (2019). *Validation and characterization of the gene regulatory role of the Usher syndrome 1G protein SANS*.

Yildirim, A., Mozaffari-Jovin, S., Wallisch, A. K., Schäfer, J., Ludwig, S. E. J., Urlaub, H., Lührmann, R., & Wolfrum, U. (2021). SANS (USH1G) regulates pre-mRNA splicing by mediating the intra-nuclear transfer of tri-snRNP complexes. *Nucleic Acids Res*, *49*(10), 5845–5866. https://doi.org/10.1093/nar/gkab386

Yu, D., Chojnowski, G., Rosenthal, M., & Kosinski, J. (2023). AlphaPulldown—a python package for protein–protein interaction screens using AlphaFold-Multimer. *Bioinformatics*, *39*(1). https://doi.org/10.1093/bioinformatics/btac749

Zelinger, L., & Swaroop, A. (2018). RNA Biology in Retinal Development and Disease. In *Trends in Genetics* (Vol. 34, Issue 5, pp. 341–351). Elsevier Ltd. https://doi.org/10.1016/j.tig.2018.01.002

Zhou, Y., Liu, F., Xu, Q., Yang, B., Li, X., Jiang, S., Hu, L., Zhang, X., Zhu, L., Li, Q., Zhu, X., Shao, H., Dai, M., Shen, Y., Ni, B., Wang, S., Zhang, Z., & Teng, Y. (2020). Inhibiting Importin 4-mediated nuclear import of CEBPD enhances chemosensitivity by repression of PRKDC-driven DNA damage repair in cervical cancer. *Oncogene*, *39*(34), 5633–5648. https://doi.org/10.1038/S41388-020-1384-3

Zhu, Y., Delhommel, F., Cordier, F., Lüchow, S., Mechaly, A., Colcombet-Cazenave, B., Girault, V., Pepermans, E., Bahloul, A., Gautier, C., Brûlé, S., Raynal, B., Hoos, S., Haouz, A., Caillet-Saguy, C., Ivarsson, Y., & Wolff, N. (2020). Deciphering the Unexpected Binding Capacity of the Third PDZ Domain of Whirlin to Various Cochlear Hair Cell Partners. *Journal of Molecular Biology*, *432*(22), 5920–5937. https://doi.org/10.1016/J.JMB.2020.09.012

12.3 Contribution to the indicated manuscripts

This cumulative thesis consists of a total of two publications as well as two chapters with preliminary data. The contributions to the preliminary data were done alone by me with scientific feedback from Prof. Dr. Uwe Wolfrum. The contributions to the publications were made by me, and other colleagues outlined in the following sections.

In Publication 1, Fritze et al., 2023, I worked together with Felizitas F. Stiehler and Prof. Dr. Uwe Wolfrum. The main results were obtained by me with some support from Felizitas F. Stiehler. The figures of the publication were prepared by me and improved with suggestions from Prof. Dr. Uwe Wolfrum. The first draft of the text was prepared by me. The final version of the publication was established by me and Prof. Dr. Uwe Wolfrum.

In Publication 2, Fritze et al., 2024, I worked together with Felizitas F. Stiehler and Prof. Dr. Uwe Wolfrum. The main results were obtained by me with some support from Felizitas F. Stiehler. The figures through the publication were prepared by me and improved with suggestions from Prof. Dr. Uwe Wolfrum. The first draft of the text was prepared by me. The final version of the publication was established by me and Prof. Dr. Uwe Wolfrum.

PERSONAL INFORMATION

*12.09.1992 in Malsch, German, married

CONTACT

Stahlbergstr. 23
55131 Mainz
Jacques.Fritze@web.de
015737960883
linkedin.com/in/jacques-fritze-581383155

HARDSKILLS

- Molecularbiology ●●●●
- Cellbiology ●●●●
- Projectmanagement ●●●○
- MS Office ●●●●
- AlphaFold ●●●○
- R(-Studio) ●●●○
- Python ●○○○

SOFTSKILLS

- Organization ●●●●
- Teamwork ●●●●
- Resilience ●●●●
- Communication ●●●○

LANGUAGES

- German ●●●●
- English ●●●●
- Chinese ●○○○

JACQUES S. FRITZE

CURRICULUM VITAE

Highly organized molecular biology enthusiast with a strong passion for project management.

WORK EXPERIENCE

Since Nov. 2020 — **PhD Student**
Johannes-Gutenberg-University, Mainz
- Topic: Usher Syndrome
- Thesis title: „Deciphering the role of SANS in protein-protein interactions and nuclear transfer“
- Methods: Cloning, (live cell-) Microscopy, DNA-, Protein- and RNA-analysis

04.2019-09.2019 — **Internship**
Chinese Academy of Science, Qingdao China
- Microbial Metabolic Engineering Group
- Topics: *In vivo* protein degradation system in cyanobacteria
- Methods: Cloning, Microbiology

12.2015-03.2017 + 11.2017-02.2019 — **Working Student**
Robert Bosch GmbH, Stuttgart + Böblingen
- Supporting the projectmanagment team
- Methods: SAP-based ordering, Budget- and timeline-planning

07.2012-07.2013 — **Voluntary Social Year**
German Red Cross, Reutlingen
- Rescue- and patient transport
- 10 weeks of paramedic training

EDUCATION

Since Nov. 2020 — **PhD Student**
Johannes-Gutenberg-University, Mainz + Graduate School IPP, Mainz
Degree: Planned for 12.2024

04.2018-11.2020 — **Master of Science Technical Biology**
University Stuttgart
Degree: M.Sc.; 1.5

10.2014-04.2018 — **Bachelor of Science Technical Biology**
University Stuttgart
Degree: B.Sc.; 2.4

09.2003-07.2012 — **Abitur**
Johannes-Kepler-Gymnasium, Reutlingen
Degree: 2.5

JACQUES S. FRITZE

PERSONAL INFORMATION

*12.09.1992 in Malsch, German, married

CONTACT

Stahlbergstr. 23
55131 Mainz
Jacques.Fritze@web.de
015737960883
linkedin.com/in/jacques-fritze-581383155

CONTINUOUS EDUCATION

2024 **GMP basic course**
GMP Academy, online

2023-2024 **Biology Meets Programming + Bioinformatics Specialization**
Coursera, online

2023 **Scientific Writing**
Graduate School IPP, Mainz

2022 **Presentation Skills**
Graduate School IPP, Mainz

2022 **Structural Bioinformatics Course**
EMBL-EBI, online

2021 **Introduction to Biostatistics**
Graduate School IPP, Mainz

SOCIAL COMMITMENT

10.2022-10.2023 **IPP-Representative**
Graduate School IPP, Mainz
Discussion and planning of IPP-events and IPP-resolutions

10.2016-10.2019 **Member of The Senate**
University of Stuttgart
Discussing and participating in university topics like study and finance

10.2015-07.2016 **Main-Organizer of the Biohazard Festival**
B.Sc. + M.Sc. Technical Biology, Stuttgart
Planning and organizing of the festival with ~2000 visitors and 50 assistances

04.2015-04.2018 **Head of Technical Biology Study Course**
B.Sc. + M.Sc. Technical Biology, Stuttgart
Planning and organizing between students and PIs

Since Mar. 2011 **Trainer in Whitewater Kayaking**
CVJM e.V., Reutlingen
Organization and planning of whitewater kayaking trips and teaching on land and water for up to 40 children

Mainz, 13.01.2025

Jacques S. Fritze

13 Acknowledgments

I would like to thank the whole AG Wolfrum team for supporting me in my time as a PhD student. Special thanks to my supervisor and boss [redacted] for having me in the lab and scientific discussion. Further I would like to thank the 3xJ^N group: [redacted] for being my anchor during the time. I would like to thank [redacted] for technical support, especially in immunoblotting. I would like to thank [redacted] for her contribution to the two publications in form of her Master thesis.

Additionally, I would like to thank the AG May-Simera group for refreshing and intellectual discussion during and outside the Journal Club. I would like to thank the AG Wolf group members [redacted] and [redacted] for their open ear and scientific support in protein structure analysis. I would like to thank [redacted] of the AG Dormann for her open ear, scientific input and technical support.

Further I would like to thank my TAC members [redacted] for their support during the TAC Meetings as well as outside discussions. Additionally, for supporting me in hard times and giving me advice.

I would like to thank the Microscopy Core Facilities of the IMB and JGU for their technical support and know how especially I would like to thank here [redacted]

Further, I would like to thank the IPP Coordinators for their organization in the IPP, for having an open ear, as well as protecting and supporting us IPP students.

I would like to thank our funders FAUN-Stiftung, the Foundation Fighting Blindness and the DFG for making this work possible.

Finally, I would like to thank my whole family for their support. My grandfather for thinking my PhD will be finished soon (from day one onwards^^) and supporting me in my way. My brother for bringing fun and exercise to my life. My parents-in-law [redacted] and [redacted] for their open ear and constructive suggestions. Special thanks goes to my parents Sonja and Claus who support and protect me since day one of my life and cheer along during every step I take. Thank you so much for everything you have done for me! Last but definitely not least to my wife and love of my live Lea who is always their for me, loves me unconditionally, drives me to higher things and protects me like a true lioness. I love you Lea!

14 Declaration

I hereby declare that present thesis is my original research work. It has not been previously presented in this or any other university for any degree. I have appropriately acknowledged and referenced all text passages that are derived literally from or are based on the content of published or unpublished work of others. I have abided by the principles of good scientific conduct laid down in the character of Johannes Gutenberg University of Mainz in carrying out the investigations described in the dissertation.

Jacques Sebastian Fritze
15.01.2025, Mainz, Germany